A Comprehensive Sensitivity Analysis of the Weather Research and Forecasting Modeling System over Southern Ontario, Canada

by

Md Mostofa Kamal

A thesis
presented to the University of Waterloo
in fulfillment of the
thesis requirement for the degree of
Master of Science
in
Earth Sciences

Waterloo, Ontario, Canada, 2017

I hereby declare that I am the sole author of this thesis. This is a true copy of the thesis, including any required final revisions, as accepted by my examiners.

I understand that my thesis may be made electronically available to the public.

Abstract

Every year weather events cause billions of dollars property damage and take many lives globally. Preventing as much damage as possible is crucial, and one way to help is through having the most accurate advance warning of extreme weather events.

Therefore, this thesis investigates the sensitivity of precipitation, temperatures, and surface energy fluxes (i.e., sensible heat flux (SHF), latent heat flux (LHF), and ground heat flux (GHF) in four cumulus cloud (CU), five cloud microphysics (MP), and four planetary boundary layer (PBL) parameterization schemes; over five years (2002, 2007, 2008, 2014, and 2015) with significantly different climatological atmospheric conditions; horizontal grid spacing; two seasons: winter and summer; and feedback between the nest and its parent domain, using the dynamical downscaling technique of the Weather Research and Forecasting (WRF) model. The main objectives are 1) to identify a combination of physics schemes that realistically reproduce observed atmospheric conditions, and 2) to improve current understanding of factors influencing the micro climate of southern Ontario, a region of complex land-water-atmosphere interactions. Ontario is also the most populous province and the largest manufacturing hub of Canada.

WRF-simulated precipitation and temperature agree well with DAYMET Model gridded observations, with correlation coefficients of nearly 0.3 to 0.8 and >0.9, respectively. Precipitation showed an average systematic bias for July of -50 to +30 mm and for January of -10 to +30 mm. The simulated precipitation was more sensitive to CU and PBL schemes. WRF-simulated temperatures showed good reproducing skill, with biases within the range of $\pm\ -1.0\,^{\circ}$ to $+1.0\,^{\circ}$ C in most parts of the domain. Model-predicted temperature was quite sensitive to PBL and MP schemes. Model-simulated precipitation variability increased when the horizontal grid resolution was refined from 8.0 to 2.67 km. However, simulated temperature variability decreased. Overall, the model performed better in the 2.67 km resolution simulation than in the highest resolution simulations (with grid spacing of 0.888 km), an unexpected finding that suggests the need for carefully designed high-resolution dynamical downscaling experiments. WRF's limitation in capturing all variabilities in a 1 km resolution simulation, particularly mountainous precipitation may result from uncertainties in our understanding of the climate and our inability to parameterize sub-grid scale processes realistically. WRF reproduced the diurnal variability of the SHF very well but systematically overestimated LHF compared to eddy covariance (EC) tower measurements for June of 2007 and 2008. For the interior of all three domains in July 2002, spatial distribution was overestimated for SHF and underestimated for LHF, with biases ranging from -30 to +30 Wm^{-2} over most of the area when compared to the North America Land Data Assimilation System (NLDAS) model gridded analysis. WRF

showed little sensitivity to the choice of PBL scheme, except for January 2002's LHF, the hottest January of the five studied. If forced with distinctively different annual climatological boundary conditions, such as extreme cold in January 2014 and below average temperatures in January 2015, the model's simulated spatial distribution of energy flux bias indicates behavior that clearly differs from NLDAS analysis. A large energy flux bias occurs over the smaller shallow northern lakes, perhaps due to incorrect representation of their water temperatures. Overall, the Kain-Fritsch (KF) CU, Yonsei University (YSU) PBL, and WRF Single-Moment 6-class (WSM6) microphysics parameterization schemes exhibit superior results over the domain studied.

The WRF model shows a high skill score over southern Ontario while reproducing observed climate means and statistics. Nevertheless, the model's performance depends on the meteorological variables, season, and synoptic conditions. The Great Lakes strongly influence atmospheric conditions in southern Ontario, by affecting precipitation and surface temperatures, ranging from the diurnal to the seasonal timescales. These results affirm the need for extensive sensitivity analysis, for both research, and operational applications. However, the findings are limited by the shorter spin-up time and by having only one-month simulation, although WRF ran for a month in both the winter and summer over multiple years.

Acknowledgements

I am deeply grateful to Drs. Martin Ross, Andre Unger, John C. Lin, and Tom W. D. Edwards, for their supervision, discussion, suggestion, and encouragement at different stages of my thesis. They have persistently taught me not only the different ways to approach a research problem, but also the art of scientific research.

I would like to express my gratitude and heartfelt thanks to my advising committee, Drs. Edward Sudicky, Richard Petron, and Chris Fletcher, for their constructive feedback and guidance over the years. I also would like to express my thanks to the Associate Dean of Science, Dr. Robert Hill, who generously extended his helping hand during a difficult time.

I would like to thank Daniel Gruner, Jemmy Hu, Isaac Ye, and Alex Man for compiling different codes and installing software packages in the SciNet and SHARCNET high performance computing clusters. Thanks also go to the Earth and Environmental Sciences graduate program coordinator, Sue Fisher, for her very warm administrative support from the initiation of the application procedure until the end of the program.

Thanks are due to my colleagues Deyong Wen, Myung-gwang Kim, Jason Davidson, Niina Luus, Joshua Benmergui, and Eric Chan for their discussions and companionship throughout my time at the University of Waterloo. I also would like to express my thanks to Syed I. Hussain, Prodip K. Kundu, Abdus Sabur, Tapan Dhar, and Ariful Hoque. They have been encouraging and supportive as I progressed through my degree. I am very greatful to Janet Mary McPherson for her Writing Center services.

Last and most importantly, I am indebted to my parents and family members, who never wavered in their support and blessing.

This research was partially supported by an Early Researcher Award grant provided to Dr. John C. Lin by the Ontario Ministry of Research and Innovation and the University of Waterloo. A project with this many computations would not be possible without the massive super computing facilities of the SciNet and SHARCNET.

The NLDAS-2 data-provider agency has requested that researchers quote the following sentence if their data is used in any study: "The data used in this study were acquired as part of the mission of NASA's Earth Science Division and archived and distributed by the Goddard Earth Sciences (GES) Data and Information Services Center (DISC)."

Dedication

More than 8.7 million people were affected and almost ten thousand people lost their lives by the cyclone SIDR in the coastal region of Bangladesh in 2007. That very high number of causalities and the severity of suffering motivated me to pursue my higher studies in Atmospheric Sciences. I would like to dedicate my M.Sc thesis to those departed souls.

Table of Contents

List of Tables

List of Figures

List of Acronyms

ABL Atmospheric Boundary Layer 6, 10

ACM2 Asymmetric Convective Model version 2 6

AVHRR Advanced Very High Resolution Radiometer 16

BEM Building Energy Model 25

BMJ Betts, Miller, and Janjic 2, 4, 26

CAPE Convective Available Potential Energy 8, 30

CBL Convective Boundary Layer 11

CC Correlation Coefficient 5, 21

CMP Cloud Microphysics Parameterization 8

CP Convective Parameterization 4, 29

CU Cumulus Cloud iii

DAYMET DAYMET gridded observation 17

EC Eddy Co-variance iii

ECMWF European Center for Medium Range and Weather Forecasting 31

GD Grel-Devenyi 26

GHF Ground Heat Flux iii

GPM Global Precipitation Measurement 18

ILBC Initial and Lateral Boundary Conditions 3, 7

IMERG Integrated Multi-satellitE Retrievals for GPM gridded observation 18

IPCC Intergovernmental Panel on Climate Change 5

KF Kain-Fritsch iv, 2, 26

LAI Leaf Area Index 10

LCL Lifting Condensation Level 31

LHF Latent Heat Flux iii

LIC Lake Ice Coverage 11

LST Lake Surface Temperatures 11

LULCC Land-use and Land-cover conversions 10

LW Long Wave Radiation 4

M2M Morrison two Moment 8

MP Microphysics iii

MYJ Mellor, Yamada, and Janjic 2, 4

MYNN2 Mellor-Yamada-Nakanishi-Niino version 2 7

NARR North American Regional Reanalysis 15, 22

NCAR National Center for Atmospheric Research 6, 14

NCEP National Center for Environmental Prediction 14, 15

NDVI Normalized Difference Vegetation Index 16

NLDAS North America Land Data Assimilation System iii, 17

NOAA National Oceanic and Atmospheric Administration 14

NoahLSM Noah Land Surface Model 24

NSAS New Simplified Arakawa-Schubert 26, 33

NSD Normalized Standard Deviation 21

NWP Numerical Weather Prediction 1

PBL Planetary Boundary Layer iii, 2, 6

PDF Probability Density Functions 21

RCP Representative Concentration Pathways 5

RMSD Root Mean Squared Difference 21

RMSE Root Mean Square Error 21

RRTM Rapid Radiative Transfer Model 2, 4, 24, 27

SHF Sensible Heat Flux iii

SST Sea Surface Temperature 11

THOM Thompson 8

UCM Urban Canopy Model 24

USGS United States Geological Survey 16

VIC Variable Infiltration Capacity 28

WRF Weather Research and Forecasting iii, 1, 14

WSM6 WRF Single-Moment 6-class microphysics iv, 123

YSU Yonsei University iv, 2, 6

Nomenclature

closure A variable is said to be unknown if it can not be represented by a prognostic or diagnostic equation. The set of equations that describe turbulent flow contain more unknowns than the numbers of equations. A new equation to represent an unknown introduces more unknowns in it. Nevertheless, an infinite number of equations are required for a complete representation of turbulence. Hence the mathematical representation of turbulence has become a never-ending problem and is called the closure problem (Stull, 1988 [93]) 7

DAYMET Model The Daymet model (DAYMET) was developed by Dr. Peter E Thornton *et al.* (2012) [98] at the University of Montana, Numerical Terradynamic Simulation Group (NTSG). The model generates daily, gridded surface temperatures, precipitation, humidity, and radiation at 1 km resolution iii, 17

hydrometeor A hydrometeor is an ensemble of liquid or solid water particles suspended in or falling through the air (Jacobson, 2005 [41]) 7

NWP Model Numerical weather prediction (NWP) models are powerful mathematical systems that allow us to simulate and understand complex weather and climate processes 1

RCM Regional Climate Model 3

Chapter 1

Introduction

Modeling is a powerful tool for interpolating and extrapolating observations, clarifying climate system processes, and scaling and integrating scientific understanding. The Weather Research and Forecasting (WRF) modeling system (Skamarock *et al.*, 2005) [90] is one next-generation Numerical Weather Prediction (NWP model. Currently, WRF is one of the most-popular mesocale models among the atmospheric science community, and has obtained its credibility not only in the atmospheric research community but also in the operational weather forecasting community. One can use this model to simulate atmospheric processes with a wide spectrum of scales, including large-eddy simulations, mesoscale, and synoptic scale.

Parameterization is a technique of representing any poorly understood phenomena in terms of variables that are well understood. This technique is widely used in the study of atmospheric phenomena (e.g., deep convection, cloud-radiation feedback, turbulent transport of heat, momentum, moisture, etc.) and is a fundamental part of the NWP Model. According to Stull (1988) [93], parameterization is an approximate representation of a natural process. In this thesis the WRF model physical parameterization sensitivity studies have two main objectives: 1) to identify a combination of physics schemes that realistically reproduce observed atmospheric conditions, and 2) to improve current understanding of factors that influence the micro climate of southern Ontario, a region of complex land-atmosphere interactions.

Application of Regional Climate Models (RCMs) has been gaining importance in recent years, including for the prediction of extreme-event recurrence intervals and the associated vulnerability assessment; energy demand forecasting for mega cities as a consequence of growing urban sprawl; and, local and regional climate change prediction with significantly

higher atmospheric CO_2 concentrations than the current level. Quite recently, model users have devoted attention to testing the sensitivity of NWP models such as WRF to establish its credibility for both stakeholders and policy makers. Figure 1.1 represents an overview of how the WRF model's physical parameterization schemes communicate with one other.

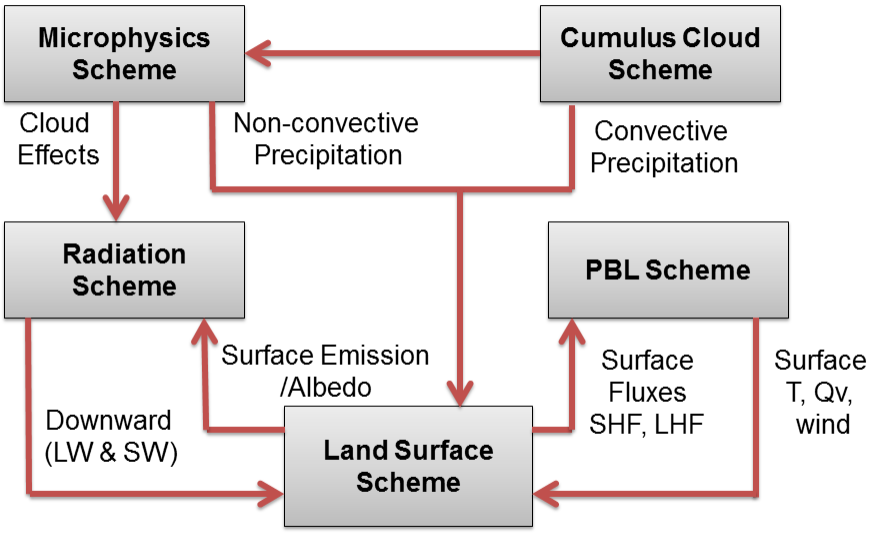

Figure 1.1: Schematic diagram showing how WRF physical parameterizations communicate with one other.

Earlier sensitivity studies using the WRF model reported that the Yonsei University (YSU) planetary boundary layer (PBL), the Kain-Fritsch (KF) cumulus, and the Rapid Radiative Transfer Model (RRTM) radiation schemes are the best-performing physics combinations for different parts of the globe. However, a "thirty-six member multi-physics ensemble" study over the south-east coast of Australia by Evans *et al.* (2012) [25] strongly advised against using the above combination in this region. In fact, their study identified the Mellor-Yamada-Janjic (MYJ) PBL scheme and the Betts, Miller, and Janjic (BMJ) cumulus scheme as the best performing combination. Surprisingly, these last two schemes showed poor performance over many other regions. Another study by Gilmore *et al.* (2015) [30] over the same Australian regions found that, over the entire precipitation event, the

BMJ cumulus scheme produced better rainfall totals, but the KF cumulus scheme reproduced hourly extreme precipitation totals very well.

RCMs may show very little to no sensitivity to the choice of physical parameterization schemes in the case of average statistics on an extreme event such as total precipitation, but hourly scales reveal a dependency on the choice of physics scheme (Gilmore *et al.*, 2015 [30]). In an ensemble experiment using ten RCMs over the Coordinated Regional Downscaling Experiment (CORDEX) African domain, conducted by Nikulin *et al.* (2012) [72], nearly all RCMs captured observed seasonal means and annual precipitation cycles quite accurately, but diurnal cycles poorly.

To characterize errors induced by the physical parameterization scheme, Awan *et al.* (2011) [5] performed a sensitivity experiment over the European Alps and concluded that model bias can be reduced significantly by using appropriate parameterization combinations. As stated by García-Díez (2013) [29], a model may provide correct average statistics for the wrong reason, such as compensating error.

Previous studies have examined and compared various aspects of regional climate model (RCM) components, such as domain size, initial and lateral boundary conditions (ILBC) data resolution, grid spacing, physical parameterization schemes, etc. They demonstrated that different physical parameterization schemes perform best for different events, variables, and metrics. Much research has been done to test the WRF model's physical parameterization sensitivity across the world at various spatial and temporal resolutions. The research discussed above clearly indicates that the results obtained by earlier studies may not be practical in all situations.

As shown in Figure 1.1, the WRF model's physical parameterization schemes provide information to one another. For example, the surface layer scheme influences the PBL through sensible and latent heat fluxes, whereas the cumulus scheme collects information from the PBL scheme. In the same way, the MP scheme is coupled with the cumulus scheme. Meanwhile, precipitation produced during cumulus convection and microphysical processes then feeds back to the surface layer scheme through soil moisture. Given these complex interdependencies, an extensive performance analysis of the WRF model can offer unique opportunities that not only enable us to identify an optimal set of physical parameterization schemes but also allow us to diagnose different sources of error by using an identical model configuration.

1.1 Literature Review

1.1.1 Cumulus Cloud Parameterization Schemes

The magnitude of cloud motions in the vertical direction varies over horizontal scales ranging from tens to hundreds of meters. When the cloud structure is sufficiently smaller than a NWP model's horizontal grid spacing ($\triangle x = \triangle y$), its evolution can be explicitly presented by the vertical momentum equation. Although computing power has considerably improved in recent decades, most mesoscale and synoptic scale models still use grid spacing of $4 \sim 50$ km and $100 \sim 200$ km, respectively. In the real atmosphere, multiple clouds with distinct heights and widths can be observed within a small horizontal distance. In a grid column of mesoscale or synoptic scale models, cloud motions are considered as subgrid-scale phenomena that significantly influence large scale flow. Therefore, subgrid-scale process effects cannot be omitted in an NWP models. The technique of representing subgrid-scale clouds in NWP models in terms of resolvable scale (large scale) meteorological variables is called convective parameterization (CP).

For optimum overall performance, parameterization developers commonly adjust different parameters in predictive equations, a practice that may perform well in some situations but fail in others. The WRF model with the YSU PBL, KF cumulus, and RRTM long wave radiation (LW) schemes were the best-performing physics combination for various parts of the world. However, a large multi-physics ensemble study by Evans *et al.* (2012) [25] strongly advised against using the above combination over South-East Australia. Their study identified the MYJ PBL scheme and the BMJ cumulus scheme as the best performing combinations. Surprisingly, these two schemes performed poorly over many regions. The same study also revealed the pressing need to fine-tune appropriate physics combinations for extreme precipitation simulation.

Cumulus convection significantly influences the dynamics and energetics of atmospheric circulation (Bechtold *et al.*, 2001 [6]; Arakawa and Schubert, 1974 [2]). Observational studies have found that latent heat released by cumulus clouds fuels the cyclone, which in turn provides the moisture that maintains cumulus clouds. During cumulus convection, entrainment and detrainment modify large-scale temperature and moisture fields, resulting in cumulus-induced subsidence in the environmental air. Entrainment, a process inherent in deep convective clouds, mixes relatively cool and dry environmental air around the edge of a cumulus cloud tower containing comparatively warm, moist air. At the cloud tower edge, the warm and moist cloud air evaporates and cools, causing downdraft as well as slowing the upward motion of clouds. During detrainment, cloud and environmental air

movement directions are reversed, and thus cloud mass is removed (escapes from the cloud) by the air around it (Jacobson, 2005 [41]).

Gilmore *et al.* (2015) [30] studied an extreme precipitation event that occurred along the eastern coast of Australia on the 8th of June, 2007, using different WRF physical parameterization schemes. Their results indicate that over the entire precipitation event, rainfall-amount and hourly precipitation maxima were realistically reproduced by the BMJ and KF cumulus schemes, respectively.

Several other studies (Mooney *et al.*, 2012 [69]; Ratna *et al.*, 2013 [86]; and Bukovsky *et al.*, 2009 [16]) have tested the sensitivity of different WRF CPs over different parts of the globe. There are multiple limitations of the above studies, including different geographic locations, individual case studies (such as squall line, thunderstorm, heavy rainfall) that span a short period of time, and with horizontal grid spacing > 10 km.

Zhao *et al.* (2012) [109] studied the WRF model over the Great Lakes region to better understand lake effect precipitation, but selected cumulus parameterization based on another study (Theeuwes *et al.*, 2010 [95]). However, both studies were limited in several ways. First, Theeuwes's study area was relatively very small, approximately equivalent to the intermediate domain of this study. Second, model boundaries were put over very complex topographic features, for example, one corner over the Appalachian mountains; another corner over Lake Huron and Lake Superior's intersection; one side of the domain start at the edge of Lake Michigan. Warner *et al.* (1997) [105], in a review paper on lateral boundary conditions (LBCs), conclusively show that an erroneous LBC limits RCM's predictability and strongly warn against putting RCM's domain boundaries over areas with complex topographies and sharp boundaries between land and water bodies. Theeuwes's study also violated certain RCM tenets discussed by Laprise *et al.* (2008) [51]. More importantly, the study tested two older versions of the KF cumulus parameterization schemes (Khain and Fritsch, 2004 [47]). In addition, Zhao's study blindly adopted the selection proposed by Theeuwes's study [95]. Last but not least, both studies focused only on winter precipitation.

Another recent study of the Great Lakes regions, by Gula and Peltier (2012) [32], investigated the sensitivity of two cumulus parameterization schemes (KF and Grell-Devenyi) and evaluated their performance using only two metrics: correlation coefficient (CC) and RMSE. Both statistics have many drawbacks. In fact, the main focus of their study was not to evaluate the WRF model's physical parameterizations, but instead to simulate how the Great Lakes affect regional climate in this region in response to various representative concentration pathways (RCP), as set by the Intergovernmental Panel on Climate Change (IPCC) 5th assessment report.

To the author's knowledge, very few studies have used the WRF model over this region, and none of them have tested multiple WRF cumulus parameterization schemes, a luxury that very few RCMs can offer. Meanwhile, many recent studies have demonstrated the importance of comprehensive sensitivity analysis (Mooney *et al.*, 2012 [69]; Jankov *et al.*, 2007 [46]). Among the NWP model community, interest has grown rapidly with current computing capabilities in producing detailed sensitivity studies.

1.1.2 Planetary Boundary Layer Parameterization Schemes

The atmospheric boundary layer (ABL), or PBL, is the bottom portion of the Earth's atmosphere, where people live and undertake nearly all their daily activities. In the ABL, the mixing of momentum, heat, moisture, and passive scalars takes place under the influence of turbulence (Holtslag and Boville, 1993 [36]). Weather research and forecasting (WRF) model-sensitivity experiments over Europe (Hu *et al.*, 2010 [40]) evaluating three different PBL schemes found that the YSU scheme of Hong *et al.* (2006) [38] widely used with the WRF model, produced results close to summer night observations but with large biases for winter night ones. The Asymmetric Convective Model 2 (ACM2) scheme of Pleim *et al.* (2007) [81, 82] and MYJ scheme of Mellor, Yamada, and Janjic (1994) [42] were found to work better in winter.

PBL processes help modulate physical properties and pollutant dispersion in the lower troposphere (García-Díez *et al.*, 2013 [29]; Hu *et al.*, 2010 [40]). They also modify both the height of deep convective clouds and formation and dissipation of low level clouds through boundary layer thermodynamics. Otkin and Greenwalld's study (2008) [75] indicates that PBL schemes influence the structural evolution of simulated cloud fields by perturbing subgrid scale temperatures, moisture, and momentum fluxes. Bright and Mullen (2002) [12] showed that, in the Fifth-Generation National Center for Atmospheric Research (NCAR) / Penn State University (PSU) Mesoscale Model (known as MM5), the forecast accuracy of convection initiation depends on proper representation of PBL processes. Several studies (Ayotte *et al.*, 1996; Betts *et al.*, 1997; and Noh *et al.*, 2003) found that PBL-structure evolution is sensitive to entrainment fluxes.

Awan *et al.* (2011) [5] configured the WRF over the European Alps and ran twenty-nine year-long hind-cast simulations with a mixed physics ensemble. They used two domains, with grid spacing of 30-km and 10-km, respectively, to dynamically downscale the ERA-40 re-analysis dataset. Switching from the MYJ to the YSU scheme reduced both temperature and precipitation biases. A recent paper by Krogsaeter and Reuder (2014) [50] studied five PBL schemes over the North Sea to evaluate their performance in simulating boundary-

layer parameters for offshore wind-energy applications. The results conclusively show that MYJ is marginally superior to the others.

García-Díez *et al.* (2013) [29] and Hu *et al.* (2010) [40] investigated the sensitivity of YSU, MYJ, and ACM2 PBL schemes over Europe and Texas (USA), respectively. To prevent the model departing from driving initial and lateral boundary conditions (ILBC), WRF was restarted every day in both studies. The former ran the model for 42hrs, and the latter for 36hrs, and both discarded the first 12hrs for model spin-up. The former ran their study for one full year and concluded that model biases depend on multiple factors, including season, geographical location, and time of day. The latter analyzed only July, August and September of 2005, and observed that the local scheme (MYJ) gave the coldest and moistest biases in the PBL. They attributed the schemes' performance differences to differences in entrainment of the air.

PBL sensitivity literature shows that YSU and MYJ are the most frequently used PBL schemes among RCM researchers and use non-local and local closure assumptions, respectively. Prior research has shown that none of the schemes perform equally in all conditions; for example, one performs better during day and the other at night. The ACM2 PBL scheme is a relatively new development that incorporates both local and non-local closure assumptions. Very few publications can be found on the Mellor-Yamada - Nakanishi-Niino version 2 (MYNN2) scheme developed based on the MYJ scheme algorithm to overcome its various limitations, including persistent cold bias at the surface, excessive moisture in the lowest couple of model layers, and lower vertical velocity. Therefore, evaluating ACM2 and MYNN2 performance can clarify PBL processes and also broaden RCM users' choices for future RCM experimental design. Realistic representation of the PBL layer in the NWP model is essential to accurate forecasting, especially of surface variables.

1.1.3 Microphysics Parameterization Schemes

Clouds are a type of hydrometeor that govern the dynamics and thermodynamics of the atmosphere through cloud-radiation feedback. In a NWP model grid box, grid-scale precipitation is produced when microphysical processes inside a cloud are explicitly resolved (Hong *et al.*, 2009 [39]). Clouds significantly affect human lives and activities at different spatial and temporal scales, ranging from the diurnal to the decadal time scales and from the mesoscale to the synoptic scale.

When water changes phase from liquid to solid, or vice versa, it releases or gains energy to or from the atmosphere, accordingly. This form of energy is called latent heat, and

it plays a crucial role in changing mesoscale circulation patterns, and influences weather and climate from the local to the global scales. Khain *et al.* (2000) [48] studied cloud microphysical processes and summarized them in one simple sentence: *"the rate of latent heat release, processes of precipitation formation, and radiative properties of clouds are affected by microphysical processes of formation, growth and interaction of drops and ice particles"*.

Prior studies have reported that in high-resolution simulations that can explicitly resolve convection processes, cloud microphysical parameterization (CMP) can be a principle source of uncertainty (Rajeevan *et al.*, 2010 [85]; Otkin and Greenwald, 2008 [75]). The results obtained by Hong and Lim (2006) [37] indicate that the complexity of MP schemes significantly influences the evolution of surface precipitation in a high-resolution simulation, and a MP scheme with more hydrometeor species produces more rainfall and more-intense rainfall peaks.

Most bulk MP parameterization schemes use two to three ice species, but the degree of sophistication and order of interactions (microphysical processes) among the species varies considerably from one scheme to another (McCumber *et al.*, 1991 [59]). Hong *et al.* (2009) [39] demonstrated that the accuracy of a grid-scale precipitation algorithm that describes microphysical processes in a model grid box affects the model's precipitation-forecasting skill .

A comparative study of one- and two- moment schemes by Morrison *et al.* (2009) [70] showed that trailing stratiform precipitation is better captured by the two-moment scheme because of the reduced rain evaporation rate in the trailing stratiform region of the two-moment scheme. Molthan and Colle (2012) [67] investigating the sensitivity of five MP schemes, reported that the observed profiles of ice crystal aggregates at 2 km and below agree quite well with profiles simulated using Morrison's two-moment scheme (M2M). The sensitivity of three WRF MP schemes (WSM6, Thompson (THOM), and M2M) were studied recently by Halder *et al.* (2015) [33] over India to simulate a severe thunderstorm. Their study found that the model-simulated convective available potential energy (CAPE), surface properties, wind speed, vertical velocity, reflectivity, and precipitation generally matched well with observation only when Morrison's MP scheme was used.

Since the grid-resolvable precipitation comes from an MP parameterization scheme, the skill of precipitation forecasting from a high-resolution model like the WRF largely depends on the accuracy of the grid-resolvable precipitation algorithm. MaCumber *et al.* (1991) [59] tested the sensitivity of several ice parameterizations while studying tropical squall lines. The model showed greater variability to the selection of hydrometeor parameters (e.g., Graupel terminal fall velocity) than to the order of microphysical process treatments

among the MP schemes.

Realistic representation of all cloud microphysical processes in a NWP model is still very difficult due to major uncertainties in the fundamental understanding of the underlying physical processes inherent in ice and water, lack of observations, and the non-linear nature of the multi-scale interactions among various hydrometeor species. Quoting Orville (1980) [73], [80] states that for an explicit representation of the growth of cloud droplets to precipitation sized particles, the conservation of water equation (1.1) needs to be split into $50 \sim 100$ equations so that each hydrometeor size category is represented by an individual prognostic equation. With explicit MP schemes forecasted, precipitation becomes more accurate, but, at the expense of computing power.

$$\frac{\partial \bar{q}_n}{\partial t} = -\bar{u}_j \frac{\partial \bar{q}_n}{\partial x_j} - \frac{1}{\rho_0} \frac{\partial}{\partial x_j} \rho_0 \overline{u_j'' q_n''} + \overline{S_{q_n}}, \qquad n = 1, 2, 3, \tag{1.1}$$

where q_1, q_2, q_3 represent the mass mixing ratio of the solid, liquid, and vapor forms of water, respectively, to the air in the same volume. S_{q_n} indicates the source-sink term, which illustrates the processes by which water undergoes phase changes. This term also represents the processes by which water is generated or lost during chemical reactions. The subgrid-scale correlation term, $\overline{u_j'' q_n''}$, is called turbulent moisture flux. The overbar represents the integrated contributions from all source-sink terms over the intervals Δx, Δy, Δz, and Δt and defined by Eq. (1.2). Since the averaging is done over all three spatial coordinates, Eq. (1.2) is also called grid-volume averaging.

$$\overline{(\,)} = \int_t^{t+\Delta t} \int_x^{x+\Delta x} \int_y^{y+\Delta y} \int_z^{z+\Delta z} (\,) \mathrm{d}z \, \mathrm{d}y \, \mathrm{d}x \, \mathrm{d}t (\Delta t)(\Delta x)(\Delta y)(\Delta z). \tag{1.2}$$

The study by Gula and Peltier (2012) [32] also tested the sensitivity of three MP parameterization schemes (WSM3, WSM6, and M2M). The WSM6 scheme is an updated version of WSM3. From this study, it is unclear why one scheme outperforms the other. There is evidence that, in some cases, a comparatively less-sophisticated MP scheme shows better performance than relatively complex schemes.

1.1.4 Surface Energy Flux

Earth's land and overlying atmosphere interact using turbulent eddies through the exchange of various surface fluxes, including heat, energy, momentum, and moisture. These fluxes result from direct partitioning of incoming solar radiation. In NWP models, some

bottom boundary conditions are provided by surface energy fluxes (Ek *et al.*, 2003 [23]). Therefore, accurate representation of surface flux components is important in determining atmospheric boundary layer (ABL) stability.

Land-use and Land-cover conversions (LULCC) directly perturb the surface energy balance by changing the surface heat capacity, albedo, roughness length, leaf area index (LAI), root depth, etc. The United States National Oceanic and Atmospheric Administration (NOAA) defined LULCCs as: "Land cover data documents how much of a region is covered by forests, wetlands, impervious surfaces, agriculture, and other land and water types. Land use shows how people use the landscape whether for development, conservation, or mixed uses." Due to LULCCs, the Planet's once-pristine surfaces have been changing since the beginning of the agricultural era, which inadvertently perturb natural climate variability. The albedo of snow-covered cultivated land is higher than that of the snow-covered forested land. Since irrigated soil is darker than bare soil and absorbs more solar radiation, large irrigated agricultural areas can perturb the surface energy balance through increasing transpiration and evaporation due to the altered surface albedo (Bounoua *et al.*, 2002 [11]). Earlier studies reported that LULCCs' dominant impacts on regional climate are evident in mid-latitude and tropical areas in winter and summer, respectively.

Elfatih (1998) [24] reported that at the Earth's surface, "net radiation has to be balanced by the sum of sensible, latent, and soil (ground) heat fluxes (i.e., SHF, LHF, and GHF)." A change in any single term of the surface heat budget equation will result in a spatial redistribution of energy. He also concludes that GHF is very small for long-term equilibrium conditions and can be negligible. Therefore, the net surface radiation is balanced by the SHF and LHF. The energy balance equation that needs to be satisfied at the surface is given in (1.3)

$$S(1-\alpha) + F_{\downarrow} - \varepsilon_s \sigma T_s^4 = H + L + G \tag{1.3}$$

where S = solar radiation (Wm^{-2}); α = albedo; $F_{\downarrow}$ = downward infrared radiation (Wm^{-2}) as a function of temperature, water vapor, and clouds; T_s = surface temperature; H = sensible heat flux (Wm^{-2}, a +ve sign indicates flux from surface to atmosphere); L = latent heat flux (Wm^{-2}, +ve indicates evapotranspiration, −ve indicates condensation); G = ground heat flux conducted into soil (Wm^{-2}); ε_s= surface emissivity; and σ is the *Stefan-Boltzmann constant.*

Strong differences in heat and moisture fluxes between adjacent land patches are widely known to affect mesoscale circulation. Eder *et al.* (2014) [21] evaluated the performance

of two energy-balance closure parameterizations and reported that the NWP model persistently underestimated turbulent heat fluxes compared to EC measurements, largely because of surface level heterogeneity to the up-wind direction from the EC measurement tower. Trier *et al.* (2010) [101] investigated the sensitivities of surface heat and moisture flux on warm season precipitation over the central United States and found that both are important in convection initiation. A similar study by Shen and Leclerc (1995) [89] reported that changes in surface heat-flux trigger changes in turbulence structures and the mean circulation in the convective boundary layer (CBL). Priestley and Taylor (1972) [84] concluded that inaccuracy in the measurement of surface values of flux and its variation with height leads to erroneous vertical transport of proper amounts of heat, momentum, moisture, and angular momentum, which in turn limits a model's ability to accurately simulate natural processes. They reported that the coupling problem between a boundary layer and larger scale dynamics cannot be solved independently.

Cordeira and Laird (2008) [19] studied two lake-effect snow events and found that the ice cover of Lake Erie affects boundary layer structure through controlling heat and moisture exchange between the lake water and overlying atmosphere. The study's greatest strength is its observational nature, and it can thus be used as a reference for the NWP model's performance evaluation. Strong connections between sea surface temperature (SST) anomalies and the surface heat budget in the high latitudes during winter were observed by Daniel (1992) [17], who noticed energy flux anomalies of up to 50 $W\,m^2$ for a monthly SST anomaly of $\sim 0.2\,^\circ$ C. Zhao *et al.* (2012) [109] found that observation-based lake surface temperatures (LST) and lake ice coverage (LIC) can ensure more-accurate transport of heat and moisture flux and maintain low-level stability, resulting in decreased lake effect precipitation bias. The latter study confirms the dominant role of the Great Lakes in winter precipitation over this region. Asefi *et al.* (2012) [3] conducted an observational study over Wheeler Lake (width of $\sim$ km), northern Alabama, which is comparatively smaller than the Great lakes, and concluded that a few degrees Celsius temperature difference between a small body of open water and surrounding land can induce lake breeze circulation. A detailed examination revealed that stronger synoptic scale flow changes lateral boundary circulation in various ways, including location, strength, direction, and inland penetration distance.

Salvi *et al.* (2012) [111] conducted numerical simulations using the University of Utah Cloud Resolving Model to examine the role of different properties of Arctic leads, both on the overlying atmosphere and large-scale surface heat budget. Their study reported that Arctic lead properties significantly influence both local and large-scale atmospheric conditions by perturbing the SHF, LHF, near surface winds, and vertical mixing of moisture. The "Surface Heat Budget of the Arctic Ocean (SHEBA)" experiment, lead by NOAA

scientists Taneil Uttal *et al.* (2002) [103] also observed a cloud plume over Arctic leads.

The above mentioned research demonstrated the importance of a lake's physical size, geographic location, water surface temperature, ice coverage, and ice thickness on the lake's overlying and surrounding atmosphere, as well as on mesoscale atmospheric circulation. However, no studies were performed on a particular area like southern Ontario, which (1) is significantly affected by lake breezes, (2) has very large temperature differences between winter and summer months, (3) is underneath the Jet Stream path, and (4) is frequently disturbed by synoptic scale processes. In summer, lake breeze from Lakes Erie, Huron, and Ontario create a rare lower tropospheric environment over southern Ontario, which can be observed at very few other places on Earth. Moreover, most of the studies were fully numerical and conducted in idealized conditions, and they prescribed surface water temperature and ice conditions over smaller lakes (that are not resolved in the driving SST data) by interpolating SST from geographically distant resolved water bodies. This approach can lead to an unrealistically warm or cold surface water temperature over those unresolved lakes. Inaccurate lake SST and ice conditions over smaller lakes, especially at midlatitudes, where ice-cover conditions significantly modulate surface flux exchanges, may produce misleading results.

1.2 Research Objectives

The above literature review has identified multiple areas that need further research. The goals of this thesis are to address the followings:

1. Evaluate the sensitivity of simulated total precipitation and temperature (the daily maximum, minimum, and mean) by varying the different physical parameterization schemes, including CU, PBL, and MP;
2. Qualitatively compare the WRF model simulations with available observations;
3. Determine whether increased horizontal resolution gives consistently better results, and whether this approach is economically justified by the resulting performance increase;
4. Identify whether the WRF model quantitatively captures the variability of precipitation and temperature;
5. Explore whether the WRF model is able to simulate observed extreme characteristics for different variables;

6. Experiment with various grid spacings and identify the optimum one for a given forecasting accuracy so that existing computing resources can be used to simulate climate over relatively large domains;

7. Quantify systematic errors (bias) and detect their possible sources;

8. Determine whether running the model over different seasons (cold and warm) sheds light on issues that may not be apparent in a single season;

9. Investigate why different parameterization schemes give different results in winter and summer months.

In summary, my MSc study contributes to science directly in two ways. Firstly, it will help to assess the forecast skill of the WRF model and to improve understanding about the meteorological variables and events that dominate the weather and climate system over the Great Lakes region, thereby supplementing the very few existing assessments. Secondly, the results could help regional climate model users who are interested in using the WRF model by providing a pre-identified set of physical parameterizations that perform optimally over the southern Ontario region.

1.3 Thesis Organization

The organization of this thesis is as follows: a brief description of the model, data set, experiment design, and the model's performance-evaluation methodologies are discussed in Chapter 2. The relative skill of the WRF CU, PBL, and MP parameterization schemes in reproducing various observed atmospheric conditions are presented in Chapters 3, 4, and 5, respectively. Assessment of the WRF model performance in simulating the surface energy balance over southern Ontario is explored in Chapter 6. Chapter 7 discusses the results of the present research and compares them with the results of other studies of similar nature. Finally, Chapter 8 summarizes the key findings of this thesis research and suggest research and policy recommendations for future research.

Chapter 2

Model, Data and Experimental Design

2.1 Model Description

Modeling is a powerful tool for interpolating and extrapolating observations, clarifying climate system processes, and scaling and integrating scientific understanding.

2.1.1 The Weather Research and Forecasting (WRF) Modeling System

This study uses the Weather Research and Forecasting (WRF) model version 3.3 as a nested regional climate model (Skamarock et al., 2005 [90]). This fully compressible, Eulerian non-hydrostatic (with a runtime hydrostatic option) model was developed jointly by the U.S. National Center for Atmospheric Research (NCAR), the National Oceanic and Atmospheric Administration (NOAA), and the National Center for Environmental Prediction (NCEP), in conjunction with over 150 organizations and universities worldwide, to meet both operational forecasting and atmospheric research needs. This next-generation mesoscale numerical weather-prediction system can be applied across scales ranging from meters to thousands of kilometers. The WRF is freely available at http://www.mmm.ucar.edu/wrf/users/download/get_sources.html.

2.1.2 Use Mesoscale Models

The term "mesoscale model" in the field of atmospheric science refers to an NWP model which can resolve atmospheric features with a horizontal scale on the order of a few kilometers to several hundred kilometers. Pielke Sr. [80] defined the mesoscale as "having a temporal and a horizontal spatial scale smaller than the conventional radiosonde network, but significantly larger than individual cumulus clouds while the vertical scale extends from tens of meters to the depth of the troposphere." Thunis and Bornstein (1996) [100] compiled a Table that summarizes the main atmospheric scales used by atmospheric scientists (cf. Appendix C, Fig. C.0.1). Typical examples of mesoscale atmospheric features include thunderstorms, tornadoes, land-sea breezes, squall lines, and mesoscale convective systems. These mesoscale weather phenomena are often triggered by topography, and coastlines and directly affect human activities. Therefore, a better understanding about mesoscale models will enable us to ensure their optimum use in both research and operational weather forecasting fields.

2.2 Data for Model Initialization

2.2.1 The North American Regional Reanalysis (NARR)

The North American Regional Reanalysis (NARR) computed at the U.S. National Center for Environmental Prediction (NCEP) (from the NCAR CISL research data archive, http://rda.ucar.edu/datasets/ds608.0/index.html#sfol-hr?g=3) was used to provide time varying (every three hours) large-scale conditions at the lateral boundary of the outermost domain. This study used the highest resolution output of the NARR (32 km spatially and every three hours temporally) data (Mesinger *et al.*, 2006 [61]).

2.2.2 Sea Surface Temperature (SST)

It is beneficial to update the sea surface temperatures (SSTs) regularly when running the model for longer simulations. Hence, a daily, high-resolution (on a $0.5^\circ \times 0.5^\circ$ grid), real-time, global, sea surface temperature (RTG_SST from http://polar.ncep.noaa.gov/sst/oper/Welcome.html) developed at NCEP's Marine Modeling and Analysis Branch (NCEP/MMAB) was used (Thiébaux *et al.*, 2003 [96]). The daily SST data was interpolated to the required three-hour intervals to match the NARR data intervals.

2.2.3 Land Use and Topographic Data

In order to ensure finer representation of the topography and surface characteristics that match the WRF model domain resolution, this study uses the U.S. Geological Survey (USGS) 24 classification categories of land use data based on 1-km advanced very high resolution radiometer (AVHRR) 10-day normalized difference vegetation index (NDVI) composites (April 1992-March 1993). The study also uses the 30 second ($\sim 1km$ horizontal resolution) data set to interpolate the topography and land surface characteristics. Figure 2.1 shows the topographic distribution over the study area.

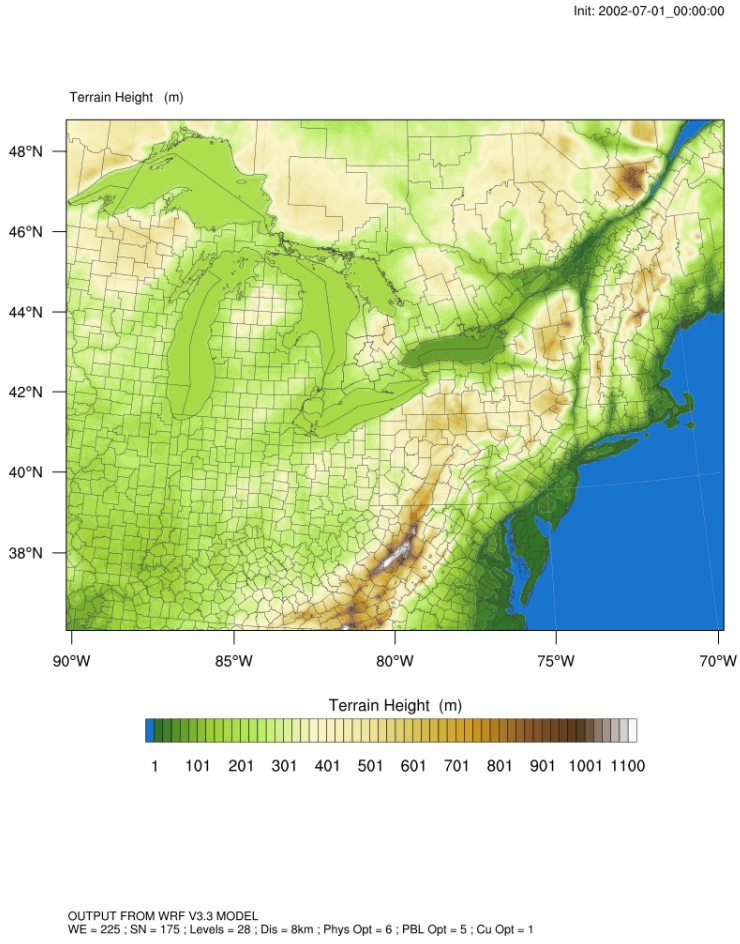

Figure 2.1: Topographic distribution over the study area

2.3 Data for Model Verification

This study compares WRF outputs with different observational datasets: Eddy Covariance tower measurements and high-resolution gridded climate datasets called DAYMET gridded observation (DAYMET), atmospheric soundings, and independent land surface model outputs, such as the North America Land Data Assimilation System (NLDAS) Phase 2 products (NLDAS-2).

2.3.1 Eddy Covariance Tower Measurement

This study compares WRF-simulated SHF, LHF, and GHF with EC tower measurements obtained at the Strawberry Creek Watershed station, Waterloo, Ontario, described in detail by Petrone *et al.* (2008) [78]. The EC tower mainly measures major surface energy fluxes (latent and sensible heat) and carbon fluxes along with other meteorological variables. Due to unstable meteorological conditions and unavoidable instrumental malfunctions, the EC data is marred by missing and abnormally high and low values, and requires correction before use. Therefore, missing values in both EC and meteorological data were compensated using Mean Diurnal Variation (MDV) technique (Falge *et al.*, 2001 [26]).

2.3.2 DAYMET Gridded Observations

High resolution climate data (1 km2 spatially) are able to capture environmental variability of temperature and precipitation that can be partly lost at lower resolutions, especially over mountain environments and areas with strong climate gradients. This study differs from other mainly because its models output is compared with the highest resolution observational data set, the DAYMET interpolated observation (an output of the DAYMET model) developed by Oak Ridge National Laboratory. Of interest were the daily maximum, minimum, and mean temperatures and precipitation. The DAYMET Model was originally developed by Numerical Terradynamic Simulation Group (NTSG) at the University of Montana. In the Daymet algorithm, a truncated Gaussian weighting filter is combined with spatially and temporally explicit empirical relationships of temperature and precipitation to topographic height to interpolate a desired variable at each prediction point. The algorithm establishes a system in which the search radius of stations is reduced in data-rich regions and increased in data-poor ones (Thornton *et al.*, 1997 [99]). The DAYMET model generates daily, gridded surface temperatures, precipitation, humidity, and radiation at a spatial resolution of 1 km x 1 km, comprising the highest-resolution observational data set

for the entirety of North America and which is available from 1980 through the latest full calendar year. Thornton *et al.* (2012) [98] describes the DAYMET product and a detailed description of the DAYMET data set is given at: http://daymet.ornl.gov/overview.

2.3.3 Global Precipitation Measurement (GPM) Multi-satellite Observations

The WRF model simulations were compared with the Global Precipitation Measurement (GPM) satellite observation data sets, also know as Integrated Multi-satellitE Retrievals for GPM (IMERG) gridded observation. The IMERG is a satellite based tertiary-level precipitation data set that combines data from all passive-microwave instruments in the GPM Constellation. Precipitation data is available at $0.1^\circ \times 0.1^\circ$ grid to 30 minute horizontal and 6 hourly temporal resolutions.

Detailed descriptions of the IMERG gridded observations can be found at: http://pmm.nasa.gov/data-access/downloads/gpm.

2.3.4 NLDAS-2 Land Surface Model Analysis

The North America land data assimilation system (NLDAS-2) land surface model output of Mitchell *et al.* (2004) [65] is used to validate WRF-simulated SHF, LHF, and GHF. The data set has temporal coverage from January 1, 1979 to the present, with very high spatial resolution (on a $0.25^\circ \times 0.25^\circ$ grid spacing over central North America). A detailed description of the NLDAS-2 datasets can be found in Xia *et al.* (2012) [107]. The NLDAS uses NOAA's Noah, NASA's Mosaic, and University of Washington's variable infiltration capacity (VIC) land surface models (LSM) to generate output both at hourly and monthly frequencies. Since WRF model simulations used the Noah LSM, model simulations are compared in this study against the Mosaic and VIC models monthly output.

The NLDAS-2 is freely available from the following server: ftp://hydro1.sci.gsfc.nasa.gov/data/s4pa/NLDAS/. The data-provider agency has requested that researcher quote the following sentence if data is used in any study: "The data used in this study were acquired as part of the mission of NASA's Earth Science Division and archived and distributed by the Goddard Earth Sciences (GES) Data and Information Services Center (DISC)." In order to compare them with WRF model output, all the observed and other analysis gridded datasets have been re-gridded to match the corresponding WRF domain size and resolution. Descriptions of the land surface models used in NLDAS are available at http://ldas.gsfc.nasa.gov/nldas/NLDAS2model.php.

2.3.5 Atmospheric Soundings

The NCEP Automated Data Processing (ADP) global upper air and surface weather observations are used to check the behavior of various meteorological variables on levels other than the surface. This data set is used to compare simulated vertical profiles of temperature and specific humidity. This study is forced to compare WRF simulated profiles with atmospheric soundings only at 0000 UTC and 1200 UTC, as most stations release balloons only twice a day.

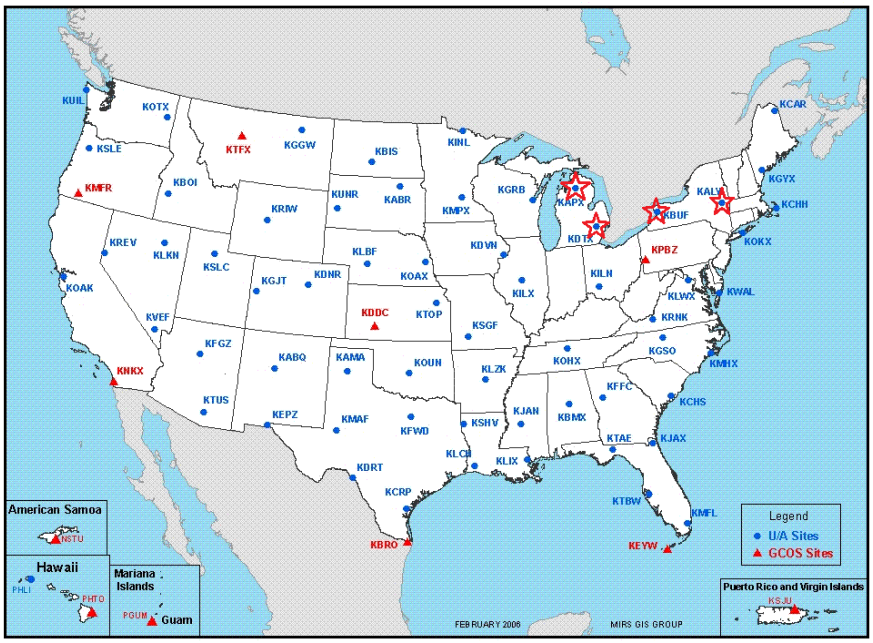

Figure 2.2: NOAA's National Weather Service (NWS)-operated radiosonde observations station map. WRF simulations are compared with soundings taken at four stations, highlighted by red stars: Detroit (DTX) and Gaylord (APX), Michigan, and Buffalo (BUF) and Albany (ALY), New York, USA.

Detailed descriptions of the NCEP ADP global upper air and surface weather observations can be found at: http://rda.ucar.edu/datasets/ds337.0/.

2.3.6 The Great Lakes Ice-cover Statistics

Winter season large-scale conditions over the North American continent, more specifically over the north-eastern part, were distinctly different in 2001-2002, 2013-2014, and 2014-2015. According to Environment Canada, the winter of 2002 was the 8th warmest in over half a century; 2014 was the coldest winter in the last 18 years; and 2015's winter was slightly below average. In 2002, the Great Lakes were nearly ice free. During the entire season, the maximum cover never exceeded 15%, and average ice covered areas were slightly below 10 %. In contrast, by the first week of January 2014, more than 90 % of the Great Lakes surface area was ice. The NOAA ranked 2014 as having the second-highest ice-cover in the Lakes' recorded history. By the third week of January, Lake Erie, the shallowest of the Great Lakes, was entirely ice covered. The ice extent for 2015 was also above average (the long-term average is 51 % since 1973) covering more than 50 % of Lake Erie by January 10, and 80 % by January 15. By February 28, 2015, both Lake Huron and Lake Erie were 95 % ice covered.

2.4 Evaluation of Model Performance

For a sensitivity-analysis study using NWP models, it is a pre-requisite to determine whether a model forecast is on target, i.e., compare actual observations with the model's analysis or short-term forecast. It is the first responsibility of a modeler to ensure that the chosen model is able to reproduce the observed climatology over the experimental domain. Pielke Sr. (2002) [80] has stated that six basic requirements must be met in order to establish the credibility of simulations performed using a mesoscale numerical model like WRF:

1. The model must be compared with a known analytic solution.
2. Nonlinear simulations with the model must be compared with the results from other models that have been developed independently.
3. The mass, moisture, and energy budgets of the model must be computed to determine the conservation of these important physical quantities.
4. The model predictions must be quantitatively compared with observations.
5. The computer logic of the model must be available upon request, so that the flow structure of the code can be examined.

6. The published version of the model must have been subjected to peer review, and model results presented in recognized professional journals should carry more weight than those distributed in report formats.

2.4.1 Evaluation Methodologies

There are a variety of ways to assess NWP models' forecast reproducibility skill or accuracy, but in a broader sense, all evaluation methodologies fall into two categories: subjective(qualitative comparison) and objective (quantitative evaluation) validation. Specifically, root-mean-square errors (RMSE), correlation coefficients (CC), and bias or threat scores. are widely used in the atmospheric science community. The RMSE is a simple but popular way of representing an overview of the absolute accuracy of a data set (Teddy Holt and Sethu Rahman, 1988 [35]). However, Anthes (1986) [1] warned against using RMSE for model performance evaluation because it does not portray how well a model predicts the overall structure of a variable.

Taylor (2001) [94] developed a technique that illustrates multiple aspects of model performance, such as the pattern CC, normalized standard deviation (NSD), and root mean square difference (RMSD) in a single diagram. Indeed, it is one of the most popular climate model evaluation metrics among the Earth Sciences community.

Scientists today are not only interested in climate mean values but also in the frequency and severity of climate extremes that damage human lives and property. Probability density functions (PDF) are widely used metrics that allow us to estimate the probability of a given variable of interest such as a particular temperature or precipitation event (Perkins *et al.*, 2007 [77]).

This thesis uses the following methodologies to evaluate the sensitivity of different WRF physical parameterizations in simulating the observed variability of multiple meteorological variables, such as both grid scale (from the microphysics parameterization scheme) and subgrid scale (from the convective parameterization scheme) precipitation and major surface energy fluxes.

- Time series analysis
- Spatial distribution of systematic bias (model-observation)
- Root mean square error (RMSE)
- Box and whisker plot

- Taylor statistics [Taylor (2001) [94]]
- Probability density functions (PDFs)

2.5 Experimental Design

To the author's best knowledge, very few publications explicitly focus on the southern Ontario region and comprehensively (i.e., using different seasons, grid resolutions, feedback on/off, downscaling, multiple physics options, and input SST data resolution) investigate the WRF model's physical parameterization sensitivity. In fact, there are still some interesting and relevant problems to be addressed. In my study, I do not assume *a priori* that a certain physical parameterization scheme performs better than others; rather, I will follow the scientific method to identify a set of physical parameterizations that give optimum performance over the study area.

The WRF model, version 3.3, is used to conduct forty-two simulations, each spanning about two months, on a three-domain nested grid with horizontal resolutions at 8.0, 2.67, and 0.89 km, respectively. The goal is to examine the performance of different physical parameterization schemes available in the WRF model with two main research objectives: 1) to identify a combination of physics schemes that realistically reproduce observed atmospheric conditions and 2) to improve current understanding of factors that influence the micro climate of southern Ontario, a region of complex land-atmosphere interactions. The first set, of thirty four simulations, spans December 1, 2001 to January 31, 2002, and the second set spans June 1, 2001 to July 31, 2002. For each set of simulations, the first month is discarded for model spin-up. The results presented here focus on January and July of 2002, as representatives of winter and summer, respectively.

The experimental model grids are arranged such that the innermost domain covers southern Ontario, Canada, whereas the outermost domain covers the entire Great Lakes basin (Figure 2.3). The horizontal resolution of the coarser domain is 8.0 km both in the east-west and the north-south directions. The horizontal resolution of the nest is automatically adjusted to 1:3:3 ratios, i.e., 2.67 km (=8km/3) for the intermediate nest and 0.889 km (=2.67/3) for the innermost nest. There are 225 grid boxes along the east-west and 175 grid boxes along the north-south directions.

The North American Regional Reanalysis (NARR) dataset is used to provide time-varying (every three hours) large-scale conditions at the lateral boundary of the outermost domain. The SST is updated every three hours. The model is run at 28 vertical sigma layers, with the model top at 10 hPa. The integration time step is set to 48 seconds, six

times the horizontal resolution of the coarser domain (= 6 x 8 km) as advised by the WRF developer. The radiation physics subroutines are called only every 8 minutes for all three nests, thereby saving computing time.

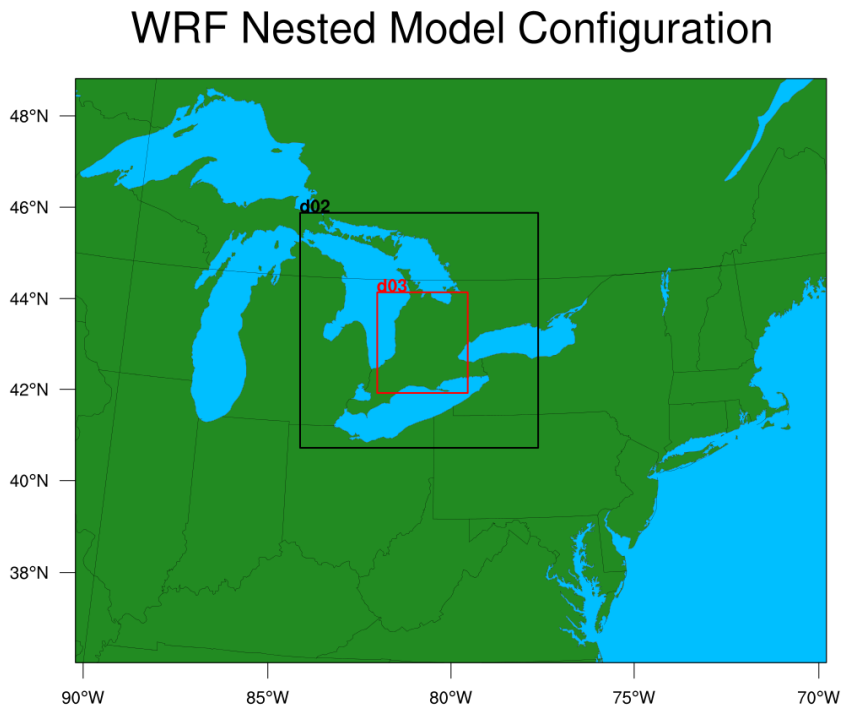

Figure 2.3: Map showing nested WRF model configuration over the study area. The experimental model grids were arranged such that the innermost domain covers southern Ontario, Canada, whereas the outermost domain covers the entire Great Lakes basin.The horizontal grid spacing of coarser domain (labeled d01), intermediate domain (d02), and finer domain (d03) is 8.0, 2.67, and 0.888 km, respectively.

The WRF model offers multiple surface layer schemes that use similarity theory to calculate exchange coefficients; diagnostics of two meter temperature (T2m) and specific humidity (q); and wind components at a 10 meter height. The surface layer scheme also provides exchange coefficients and a frictional velocity to land-surface model and

PBL scheme, respectively. Of the four PBL schemes used to examine the sensitivity of surface energy fluxes, the YSU, ACM2, and MYNN2 schemes use the MM5 surface layer scheme based on the similarity theory of Monin and Obukhov (1954) [68], with a Carslon-Boland viscous sub-layer. On the other hand, the MYJ scheme uses the Eta surface layer scheme (Janjic 1996, 2002) [45, 44] that also uses the similarity theory of [68] along with Zilitinkevich thermal roughness length Zilitinkevich (1970) [110]. The MYJ and MYNN2 schemes use local closure assumptions, whereas the YSU and ACM2 schemes use non-local closure assumptions. For the PBL parameterization sensitivity experiments, each simulation was performed by varying one physical parameterization scheme at a time, while keeping the others fixed. To simulate processes inherent in long-wave and shortwave radiation, the rapid radiative transfer model (RRTM) of Mlawer *et al.* (1997) [66] and the Dudhia schemes of Dudhia (1989) [20] were used, respectively.

Table 2.1: Abbreviations used to denote different Physical parameterization schemes

Physical scheme	Parameterization type	Abbreviation
New Simplified Arakawa-Schubert	Cumulus cloud	NSAS
Betts-Miller-Janjic	Cumulus cloud	BMJ
Grell-Devenyi	Cumulus cloud	GD
Kain-Fritsch	Cumulus cloud	KF
Yonsei University	PBL processes	YSU
Asymmetrical Convection Model	PBL processes	ACM2
Mellor Yamada and Janjic	PBL processes	MYJ
Mellor-Yamada-Nakanishi-Niino	PBL processes	MYNN2
Lin (Purdue)	Microphysical processes	PLIN
Eta (Ferrier)	Microphysical processes	ETA
Thompson	Microphysical processes	THOM
WRF single moment six class	Microphysical processes	WSM6
Morrison two moment	Microphysical processes	M2M
Rapid radiative transfer model	Long-wave radiation	RRTM
Dudhia	Short-wave radiation	Dudhia
Noah land-surface model	Land surface processes	Noah LSM

Of the four available land-surface parameterization schemes, this study uses the Noah land-surface model (NoahLSM), which predicts soil temperature and moisture in four layers. The Noah LSM also represents fractional snow cover and frozen soil water. As LSM is generally sufficient for large-scale studies, a separate Urban Canopy Model (UCM) or

Building Energy Model (BEM) were not required for our study. However, UCM or BEM may represent biophysical processes more realistically.

Table 2.2: Physical parameterization schemes used in each of the WRF simulations

Experiment No.	Cumulus scheme	Microphysics scheme	PBL scheme	Feedback On	Feedback Off
Exp#1	NSAS	YSU	YSU	Yes	Yes
Exp#2	BMJ	WSM6	YSU	Yes	Yes
Exp#3	GD	WSM6	YSU	Yes	Yes
Exp#4	KF	WSM6	YSU	Yes	Yes
Exp#5	KF	ETA	YSU	Yes	NA
Exp#6	KF	PLIN	YSU	Yes	NA
Exp#7	KF	THOM	YSU	Yes	NA
Exp#8	KF	M2M	YSU	Yes	NA
Exp#9	KF	WSM6	MYJ	Yes	NA
Exp#10	KF	WSM6	MYNN2	Yes	NA
Exp#11	KF	WSM6	ACM2	Yes	NA
Exp#12	KF	WSM6	YSU	Yes	NA

This study initializes the SST field of unresolved lakes from daily-average surface air temperature following a best-guess strategy, an approach that significantly reduces surface temperature and ice-cover condition biases compared to others.

In summary, we examine the performance of the WRF model in simulating precipitation, temperature, and major surface energy fluxes over southern Ontario, Canada. To the best of our knowledge, this is the first comprehensive sensitivity study that investigates the WRF model's credibility over the Great Lakes region. By examining surface energy flux sensitivity along with the WRF model's physical parameterizations (i.e., CU, PBL, and MP) offers the opportunity to test the WRF model's forecast credibility and a chance to verify the results published for other areas. The following sub-sections present additional experiment details specific to each study.

2.5.1 Cumulus Cloud Parameterization Study

To investigate the sensitivity of WRF CPs, sixteen two-month-long WRF simulations are carried out using four cumulus cloud parameterization schemes. Each WRF simulation is

performed by varying one CP scheme at a time, while keeping the others fixed. Further, each scheme is used to simulate two winter months (December and January) and two summer months (June and July). The main objective is to examine the performance of different CP schemes available in the WRF model and then to identify a CP scheme that performs optimally over southern Ontario. This study will increase existing knowledge about the physical mechanism behind why one scheme outperforms others. Four convective parameterization schemes, described briefly with references in Table 2.3, are examined (i.e., Kain-Fritsch (KF) [47], Grel-Devenyi (GD) [31]; New Simplified Arakawa-Schubert (NSAS) [34]; and Betts-Miller-Janjic (BMJ) [43, 42]. Results from all nested domains are compared, but in some cases, only over the area equivalent to the innermost nest (a domain with grid spacing of 0.9 km). In all figures, CU denotes cumulus parameterization, abbreviated in the text to CP.

Section 3.1 briefly introduces fundamentals of cumulus cloud parameterization and key characteristics of the four CP schemes examined. Results and discussion are presented in section 3.2, followed by conclusions in section 3.3.

Table 2.3: Cumulus cloud schemes used in the outermost domain of each WRF simulation

Scheme	Momentum Tendencies	Shallow Convection	Reference
NSAS	Yes	Yes	Han and Pan (2011, WF)
BMJ	No	Yes	Janjic (1994, MWR; 2000 JAS)
GD	No	No	Grell-Devenyi (2002, GRL)
KF	No	Yes	KF (2004, JAM)

2.5.2 Planetary Boundary Layer Parameterization Study

WRF model version 3.3 users choose one PBL scheme from a pool of nine, to compute unresolved turbulent surface fluxes in the ABL. This study uses four PBL schemes (i.e., YSU, MYJ, MYNN2, and ACM2) to examine the sensitivity of precipitation (convective + non-convective) and surface temperature. Table 2.4 summarizes basic characteristics of the PBL schemes tested in this study and their corresponding references. Each WRF simulation is performed by varying one PBL parameterization scheme at a time, while keeping the others fixed.

The WRF model offers multiple surface layer schemes that use similarity theory to calculate exchange coefficients; diagnostics of two meter temperature (T2m) and specific

Table 2.4: PBL schemes tested in the current study

Scheme	Closure	PBL Top Calculated from	Reference
YSU	Non-local	Buoyancy profile	Hong *et al.* (2006, MWR)
MYJ	Local	TKE	Janjic (1994, MWR)
ACM2	Local and Non-local	Critical Bulk R_i	Pleim (2007, JAMC)
MYNN2	Local	TKE	Nakanishi and Niino (2006, BLM)

humidity (q); and wind components at a 10 meter height. The surface layer scheme also provides exchange coefficients and a frictional-velocity to land-surface model and PBL scheme, respectively. Of the four PBL schemes used in this study, the YSU, ACM2, and MYNN2 schemes use the MM5 surface layer scheme based on the similarity theory of [68] with a Carslon-Boland viscous sub-layer. On the other hand, the MYJ scheme uses the Eta surface layer scheme [45, 44] which also uses the similarity theory of [68], along with Zilitinkevich thermal roughness length [110]. The MYJ and MYNN2 schemes use local closure assumptions, whereas the YSU and ACM2 schemes use non-local closure assumptions. To simulate processes inherent in long-wave and shortwave radiation, the rapid radiative transfer model (RRTM) and the Dudhia schemes are used, respectively.

Section 4.1 briefly introduces fundamentals of PBL parameterization and key characteristics of the four PBL schemes examined. Results are presented in section 4.2 followed by discussion and conclusions in section 4.3.

2.5.3 Microphysics Parameterization Study

This study investigates CMPs with a wide spectrum of characteristics, including how many hydro-meteors are explicitly predicted; whether ice-phase and mixed-phase processes are included; whether ice particle size distribution is assumed or predicted. Table 2.5, lists the variables that each MP scheme predicts, with corresponding references. In this study, each WRF simulation is performed by varying one CMP scheme at a time, keeping the others fixed.

Section 5.1 briefly introduces fundamentals of cloud MP parameterization. Various hydrometeors properties and key characteristics of the five MP schemes examined are presented in sections 5.2 and 5.3, respectively. Results and discussion are presented in section 5.4, followed by conclusions in section 5.5.

Table 2.5: Microphysics schemes used in each of the WRF simulations

Scheme	Mass Variable	Reference
WSM6	q_v q_c q_r q_i q_s q_g	Hong and Lim (2006, JKAM)
THOM	q_v q_c q_r q_i q_s q_g	Thompson and others (2008, MWR)
PLIN	q_v q_c q_r q_i q_s q_g	Lin and others (1983, JCAM)
ETA	q_v q_c q_r q_s	Rogers and others (2001, NWS)
M2M	q_v q_c q_r q_i q_s q_g q_h	Morrison and others (2009, MWR)

2.5.4 Surface Energy Flux Sensitivity Study

As stated in the data section, the winter season large-scale conditions over the North American continent vary from year to year. In order to examine WRF-simulated surface energy fluxes' sensitivity to annual climatological atmospheric conditions, six WRF simulations are performed for January and February of 2014, and 2015 in addition to those for 2002. To investigate seasonal dependence, a year long WRF simulation is also performed for 2014. These WRF simulations use the KF cumulus, WSM6 microphysics, and YSU PBL parameterization schemes.

To compare WRF-simulated major surface energy flux components with EC tower measurements, WRF model is run for 25 days, from June 2 to June 26 for 2007 and 2008. Model simulations are compared with variable infiltration capacity (VIC), Noah, and mosaic LSM gridded analysis. The Mosaic LSM initially developed by Koster *et al.* (1992) [49] and uses the "mosaic" approach to represent subgrid-scale heterogeneity in surface characteristics. The VIC, a macroscale hydrological model developed at the University of Washington by Liang *et al.*, (1994) [54] is a comparatively sophisticated LSM that solves full water and energy balance equations. The Noah model is a four-layer LSM developed by Ek *et al.* (2003) [23] under the leadership of the NOAA. For comparison with WRF model output, the NLDAS-2-gridded analysis has been re-gridded to match the corresponding WRF domain size and resolutions.

Section 6.1 presents results from the surface energy flux sensitivity study. Discussion is presented in section 6.2, followed by conclusions in section 6.3.

Chapter 3

Assessment of WRF Model Convective Parameterization Schemes

3.1 Fundamentals of Cumulus Cloud Parameterization

Different Cloud Parameterization (CP) schemes use different closure assumptions and parameters to solve interactions among large-scale flow fields and convective clouds (Grell and Dévényi, 2002 [31]). The uncertainty associated with the closure assumptions and parameter settings have inspired the scientific community to look for better answers in the never-ending discussions of "which assumptions are appropriate under what conditions". At a shorter time scale, a CP scheme's qualities determine the accuracy of quantitative precipitation forecasts (QPFs). On the other hand, at longer-time scale, a CP scheme is judged based on its ability to reproduce an observed mean climate.

In an NWP model with horizontal grid spacing >10 km, a CP scheme can be used to reduce atmospheric instability through the redistribution of heat and moisture fluxes (some schemes also take into account momentum transport) vertically in model grid columns that contain convective clouds. During the re-distribution process, an updraft process carries boundary layer air upwards, whereas the downdraft process takes the mid-level air downwards. Fundamental difference exist among the major CPs, most falling into two categories: 1) moist convective adjustment type (first proposed by Manabe *et al.*, 1965 [58]

and 2) mass-flux type (based on Arakawa and Schubert, 1974 [2]).

3.1.1 Moist Convective Adjustment Type

When a parcel of air becomes super-saturated (with a specific humidity $q > q_*$) and conditionally or absolutely unstable (an environmental lapse rate (Γ) > moist adiabatic lapse rate (Γ_m)) at grid scale, an adjustment type scheme is used to fine-tune both the vertical temperature (T) and humidity (q) profile by an amount $\delta T(z)$, $\delta q(z)$, respectively, to obtain neutrality ($\Gamma = \Gamma_m$), such that:

$$-\int_{z_B}^{z_T} L\,\rho\,\delta q(z)\,\mathrm{d}z = \int_{z_B}^{z_T} \rho\,c_p\,\delta T(z)\,\mathrm{d}z \tag{3.1}$$

$$q(z) + \delta q(z) = q_*(T + \delta T, p) \tag{3.2}$$

where ρ represents the density of air, and L represents latent heat (the quantity of heat released or absorbed by water when changing its phase type, such as from solid to liquid or vapor with no change of temperature). Latent heat is released to the atmospheric layer, where precipitation results due to condensation.

During adjustment, the total energy is conserved across the cloud layers. This type of scheme is criticized for requiring prior grid scale saturation to initiate subgrid moist convection. The Betts-Miller-Janjic (2000) [43] scheme falls under this category. The excessive moisture of the convective cloud condenses and falls as precipitation (P) under the influence of gravity according to equation (3.3):

$$P\,[kgm^{-2}] = -\int_{z_B}^{z_T} \rho\,\delta q(z)\,\mathrm{d}z \tag{3.3}$$

3.1.2 Mass-flux Type

The Mass-flux type schemes are based on the convective available potential energy (CAPE) consumption principle. Upon activation, the mass flux cumulus schemes interchange mass between the convective cloud columns and the environment in order to relax the model's atmosphere towards a connectively adjusted state, hence the name mass flux (Bechtold *et al.*, 2001 [6]).

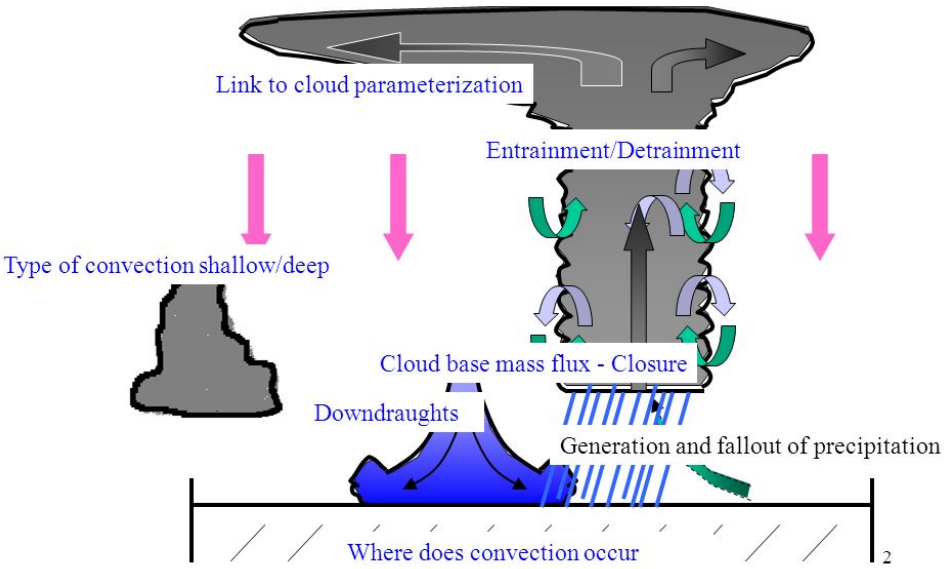

Figure 3.1: Characteristics diagram of Mass-flux type scheme [Adapted from European Center for Medium-Range Weather Forecasts (ECMWF)

The concept of a mass flux scheme was originally proposed by Arakawa (1974) [2], and a detailed description of the physical mechanism and associated mathematical representation of mass flux schemes can be found in their classic paper.

3.1.3 The Kain-Fritsch (KF) Scheme

This mass-flux-based complex cumulus scheme uses the Lagrangian parcel method to assess whether certain conditions exist in a model at a level to activate convection, with positive buoyancy being a mandatory activation condition. The KF scheme, which uses triggers function originally developed by Fritsch and Chappell (1980) [27], is based on the temperature and vertical velocity at the lifted condensation level (LCL). The trigger function starts checking a parcel for positive buoyancy at the lowest 50-hPa and repeats the procedure up to 700-hPa (Kain, 2004 [47]). Once convection is activated, a continuous rearrangement of the grid column mass takes place through updraft, downdraft, and entrainment, until at least 90% of the CAPE is consumed (removed). The KF scheme explicitly calculates the entrainment rate between convective cells and the environment. This scheme calculates the sub-grid scale or parametric precipitation (PP) according to equation (3.4).

$$PP = E\,S \tag{3.4}$$

where E is the precipitation efficiency and S represents the sum of the vertical fluxes of vapour and liquid at about 150 hPa above the LCL.

3.1.4 The Betts-Miller-Janjic (BMJ) Scheme

This scheme from [43, 42] is an adjustment-type scheme that was developed based on the algorithm of Betts (1986) and Betts and Miller (1986) [8] and [7]. The BMJ scheme removes the conditional instability of a model grid column by relaxing the temperature and specific humidity profile towards a predetermined reference profile derived from field observations (Betts and Miller, 1986 [7]). Unlike other adjustment-type schemes that relax towards a moist adiabat, the MYJ scheme uses a quasi-equilibrium state as a reference profile. The subgrid-scale precipiattion resulting from the adjustment is computed as equation (3.5) (Wang and Seman, 1997 [104]).

$$PP = \int_{P_B}^{P_T} \frac{(q_R - q)}{\tau} \frac{\mathrm{d}p}{g} \tag{3.5}$$

where p_B and p_T represent cloud top and base pressures, respectively, τ is the time scale over which the adjustment occurs, and q and q_R represent the model's and reference-profile specific humidity, respectively.

3.1.5 The Grell-Devenyi (GD) Scheme

This scheme is a mass-flux-based cumulus cloud parameterization. Several theories have been proposed to determine the location and intensity of convection. The GD scheme takes advantage of many of these closures to determine the cloud-base mass flux and generate an ensemble of 144 members (Grell and Dévényi, 2002 [31]). Statistical techniques [1] are then applied to find the optimal value at each time step and grid point for feedback to a 3-d model (e.g., WRF). Thus, this is often called an ensemble mass-flux scheme. Its developers are hopeful that their techniques can be applied to other physical parameterization schemes. It takes into account any subsidence effects, and spreads the subsided air to the neighboring

[1] Mean, standard deviation, skewness, and kurtosis (flatness) are computed at each grid-point individually for individual sub-ensembles and also for unified ensembles

grid columns. Recently, Krogsaeter and Reuder (2014) [50] suggested using this scheme for a high resolution (grid spacing < 10 km) model run.

3.1.6 The New Simplified Arakawa-Schubert (NSAS) Scheme

The Old simplified Arakawa-Schubert (SAS) convective parameterization scheme (Pan and Wu, 1995 [76]) was used in the operational version of the NCEP's Global Forecast System (GFS) to represent deep cumulus convection. The SAS scheme had no shallow convection (SC) component; therefore, its algorithm was modified, especially the parameters related cloud-base mass flux, entrainment, and detainment processes, to represent the SC as well, hence the name New simplified Arakawa-Schubert (NSAS) scheme (Han and Pan, 2011 [34]).

The old scheme was unable to fully remove grid column instability within the relaxation time scale, and a problem blamed for the excessive grid-scale precipitation. To alleviate the excessive precipitation problem, the new scheme revised the old deep convection algorithm to accommodate a large cloud-base mass-flux and higher cloud tops. The level at which the maximum moist static energy is found is considered to be the convection starting point. In the case of shallow convection, the algorithm searches for the maximum moist static energy level within the PBL, whereas for deep convection, a search is extended up to 700-hPa from the Earth's surface. In the NSAS scheme, deep convection is activated if a cloud is thicker than 150-hPa; otherwise, it is considered to be shallow convection.

3.2 Results and Discussions

We examined the sensitivity of WRF-simulated total precipitation (RAINC + RAINNC), daily maximum, minimum, and mean temperatures across four convective parameterization schemes. The DAYMET gridded-observations have been reprojected to match the WRF domain size and resolution, since nested WRF simulations cover different domain sizes (Figure 2.3). In addition, for consistency during comparisons, we carried out analyses over the domain areas that are shared by all three domains. The main goal was to investigate the skill of different convective parameterization schemes in reproducing observed temperature and precipitation patterns over southern Ontario; later, the knowledge is applied for regional climate change assessment using the WRF mesoscale model [90].

3.2.1 Precipitation

Temporal Precipitation Patterns

Figure 3.2 represents the domain-averaged daily time series of the DAYMET-gridded observations and WRF-simulated total precipitation (RAINC + RAINNC) for the four CP schemes, for January 2002. The WRF model realistically reproduces both the precipitation phase and intensity, and captured the extreme precipitation pattern very well, with some exceptions. However, an altered pattern was observed for July, indicating that simulated July precipitation is quite sensitive to convective parameterization. Further, WRF simulations showed comparatively poor skill relative to the DAYMET observations in simulating extreme precipitation events in July. The innermost domain-averaged simulated total precipitation shows very little sensitivity to the choice of CP scheme for January's primarily snowy precipitation. However, for July's rain-only precipitation, it shows substantial variability to the choice of CP scheme. The time series for July precipitation also illustrates disagreement in the precipitation magnitude simulated by different convective schemes. A phase lag among the simulated and observed rainfall is clear, but was not seen in the precipitation time series from the coarser domain (Figure 3.2). Increased precipitation variabilities are seen due to dynamical downscaling. It is hypothesized that rainfall distribution in the innermost nest increased because of more realistic representation of land use and land-cover classes over the domain.

Consider Figure 3.3, which plots accumulated total precipitation from the outermost (d01) and intermediate (d02) domains using the four CPs against DAYMET observations. Dynamical downscaling shows hardly any changes to the precipitation total, and the WSM6 scheme shows excellent forecasting skill in reproducing the observed precipitation total. The BMJ and NSAS schemes show comparatively small bias, and the GD scheme gives the largest systematic bias among the four.

January's accumulated surface precipitation total varies hardly at all with cumulus-scheme change (Figure 3.4). However, a large mismatch ($\sim$ 50 %) between the simulated and observed precipitation patterns is noticeable, mostly originating from the microphysics parameterization scheme.

The time series analysis gives an overview of the intensity and phase of precipitation, but ignores spatial distribution. Therefore, the spatial distribution of monthly domain-averaged precipitation bias is discussed next.

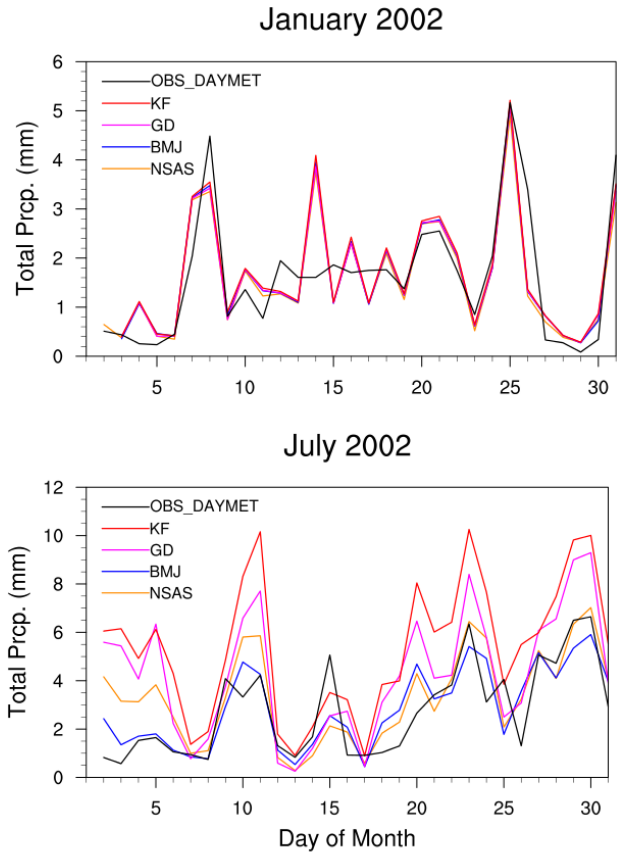

Figure 3.2: Domain averaged daily time series of the DAYMET observations (black) and WRF-simulated total precipitation (RAINC + RAINNC) in mm/day for January (top pannel) and July (bottom pannel) by four convective schemes: KF (red), BMJ (blue), GD (magenta), and NSAS (dark orange) from coarse resolution domain (domain with grid spacing 8 km).

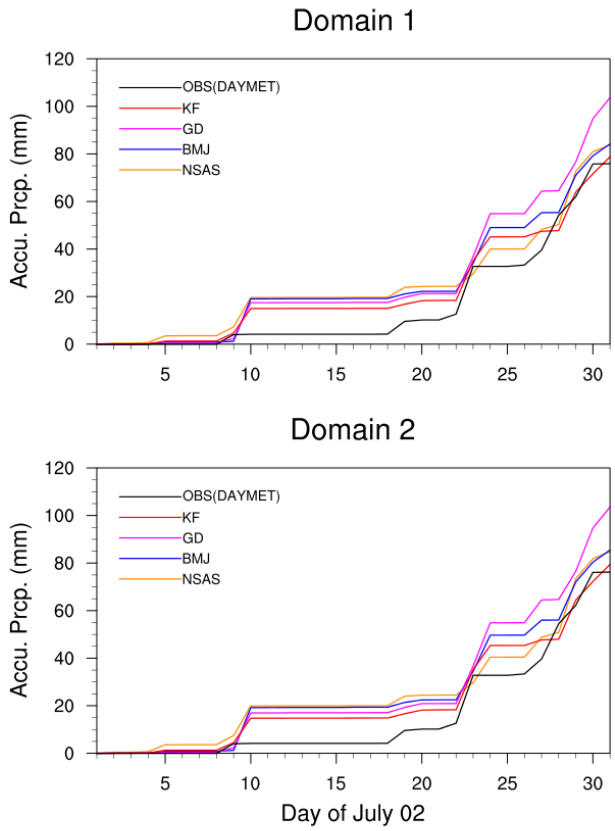

Figure 3.3: Temporal evolution of spatially and temporally averaged WRF-simulated accumulated total precipitation (mm) using four different CU schemes (KF(red), GD (magenta), BMJ(blue), and NSAS(yellow)) and DAYMET observations (black) from (a) Domain 1 (top panel) (b) Domain 2 (bottom panel) for July 2002.

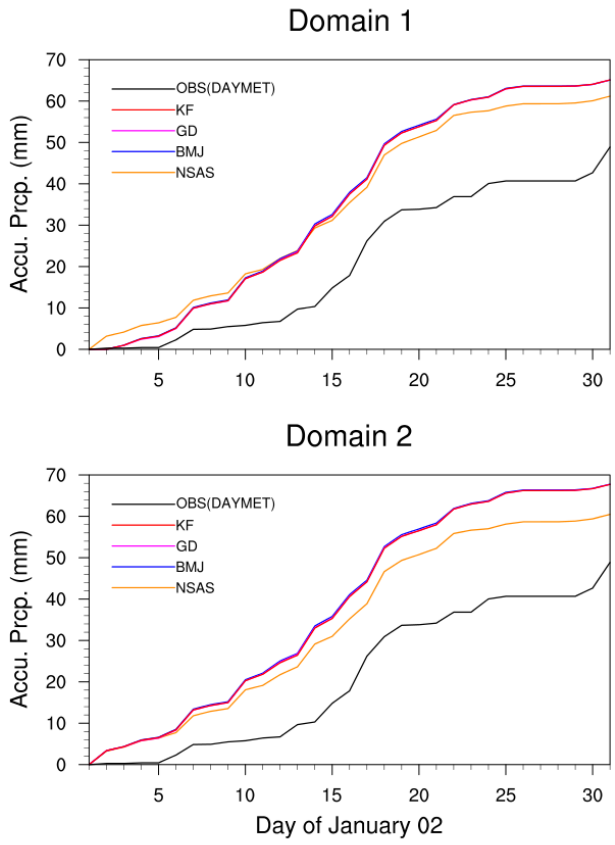

Figure 3.4: Same as Figure 3.3 but for January 2002.

Spatial Precipitation Patterns

Figure 3.5 illustrates biases in the spatial distribution of WRF-simulated monthly total precipitation (convective + grid-scale) from the DAYMET observations (WRF - DAYMET) for July 2002. The BMJ clearly produces comparatively lower spatial biases than the other CPs. Simulated-precipitation using KF and NSAS schemes show dry and wet biases, respectively. Overall, all schemes overestimated (underestimated) precipitation in the north-west (south-east) corner of southern Ontario. Over the Grand River watershed, WRF underestimated July precipitation.

In January, model-simulated precipitation shows a positive bias (less than 30mm in most of the area) over the whole domain, except over some areas in the interior (not shown). Further, over southern Ontario, January's mostly snowy precipitation (which is more dependent on micro-physical processes) demonstrate little sensitivity to CP, with none a clear superior. The NSAS-simulated-precipitation's comparatively lower biases do not differ significantly from to others.

In summary, simulated precipitation showed a systematic negative bias (underestimation) in the interior of all domains in both months, although the bias patterns differ. In general, systematic bias is higher in July (on average -50 to +30 mm) than in January (on average -10 to +30 mm).

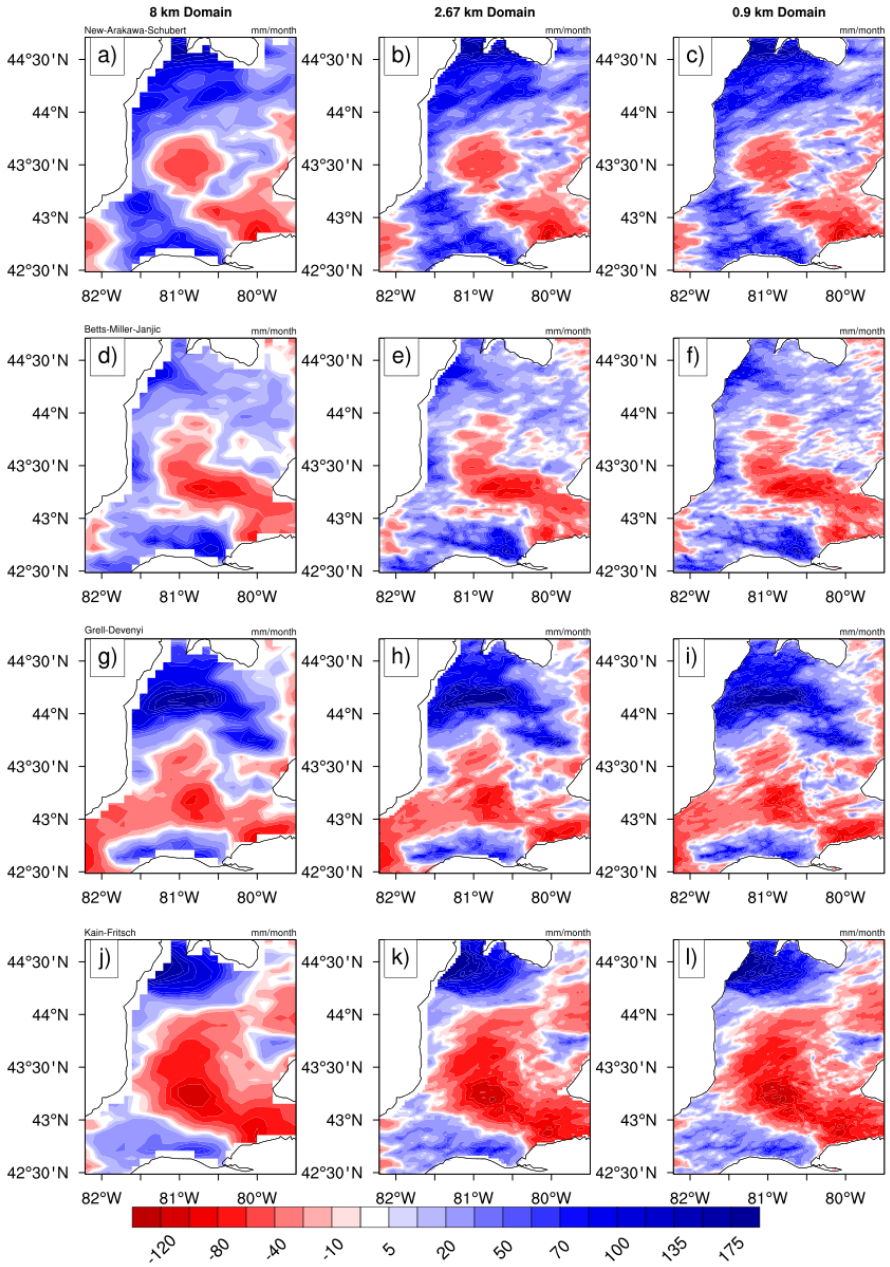

Figure 3.5: Precipitation bias (Model - Observation) of WRF compared to DAYMET gridded observation for July 2002. Results from the three nested domains: 8km, 2.67 km and 0.9km are illustrated from left to right column. Four convective parameterization schemes are arranged from top to bottom as follows: NSAS (first row), BMJ (second row), GD (third row), and KF (fourth row)

Grid and Sub-grid Scale Precipitation

Unlike earlier studies this study focus is not limited to finding a cumulus scheme explicitly based on evaluation metrics, it also aims to understand the causes of precipitation variability. In the WRF model, precipitation originates as a by-product of grid scale processes (from the MP scheme) and sub-grid scale processes (from a CP scheme). Since this study aims to identify the best-performing CPs, the big question IS whether a certain CP is over or under-active. A two-step procedure is recommended for the preliminary assessment of a set of convective parameterization schemes. First, the simulated total and convective precipitation pattern is scrutinized whether appropriate amounts of convective precipitation are produced at certain places and times. Second, one considers whether a place received unusual amounts of unexpected precipitation. Therefore, to isolate the performance of individual CPs, grid scale and sub-grid scale precipitation are analyzed separately.

For current analysis, this study compared results only from the outermost domain, which has a grid spacing of 8 km. There are two reasons for choosing the outermost domain and plotting the whole area instead of only of the area that covers the innermost domain. First, the model uses cumulus parameterization only in the outermost domain. Second, the outermost domain offers more areal coverage in which to look for a broader spectrum of convective activity.

The spatial distribution of WRF-simulated sub-grid scale precipitation clearly shows great sensitivity to CPS in July when convective activity dominates local precipitation (Figure 3.6). Monthly convective precipitation rates differ greatly; indeed, one can divide the four CPs into two groups. The KF and GD schemes generated too much convective precipitation and fall into the first group. In contrast, the NSAS and BMJ schemes produced comparatively lower convective precipitation and belong to the second group. The sub-grid-scale precipitation in July shows strong regional differences and is dominated by orography.

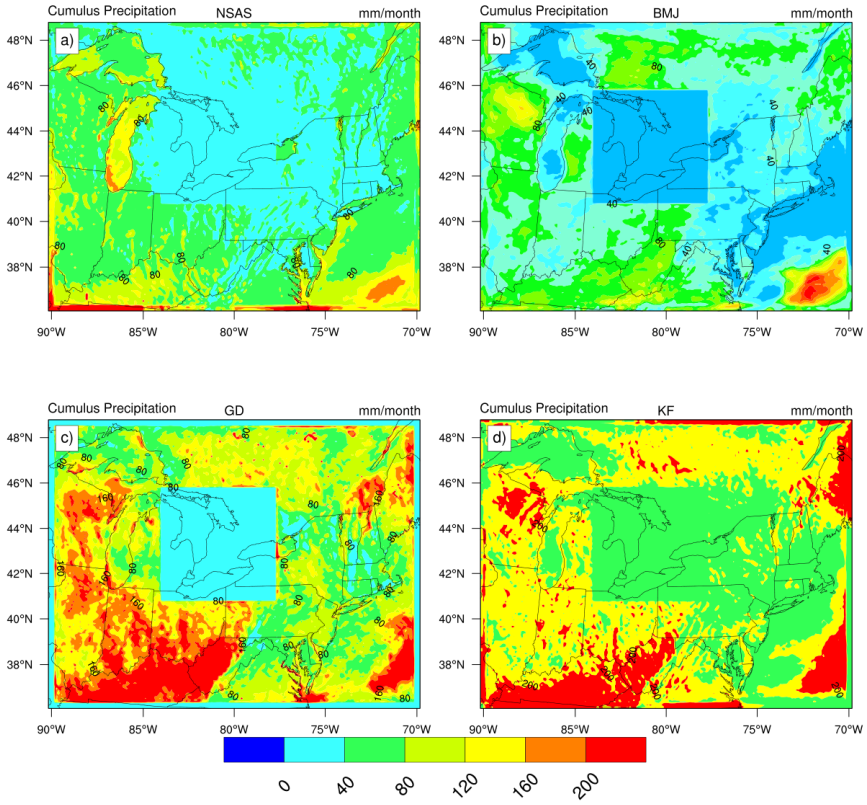

Figure 3.6: The spatial distribution of monthly accumulated sub-grid scale precipitation in mm (generated by convection parameterization scheme) from the outermost domain (d01) for July 2002: a) NSAS, b) BMJ, c) GD, and e) KF.

A visual comparison of the spatial distribution of simulated sub-gcdrid and grid scale precipitation from the outermost domain reveals that, in January, most precipitation is grid-scale, and originates from microphysical processes (Figures 3.7 and A.0.1). This grid-scale precipitation is an order of magnitude higher than the sub-grid-scale precipitation. Great Lakes' influences on the spatial distribution of precipitation far downstream is clearly seen.

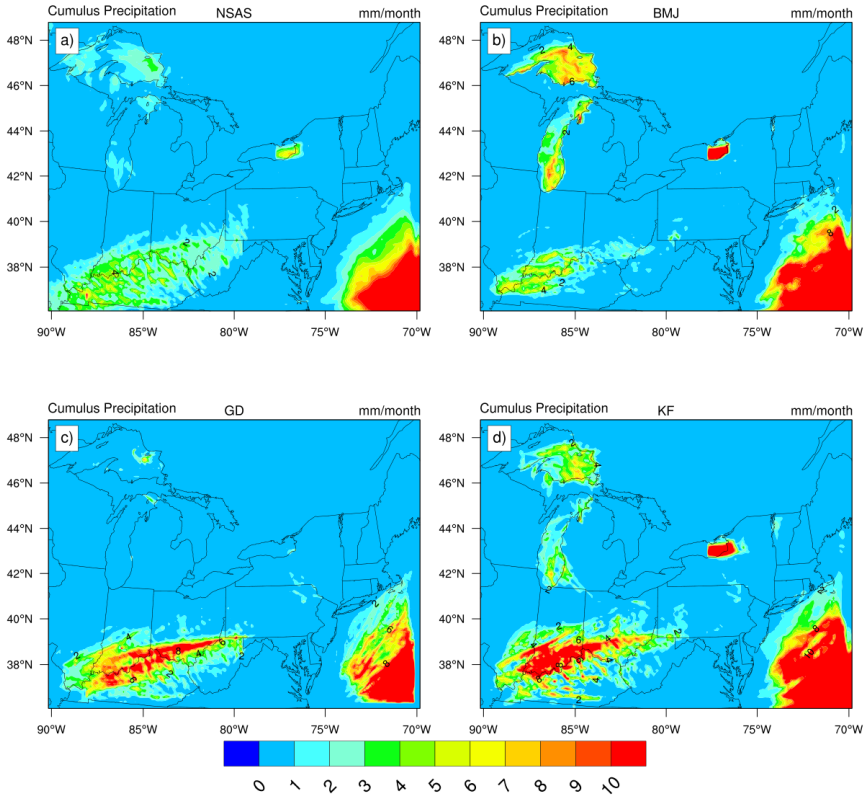

Figure 3.7: As in Figure 3.6 but for January

In summary, convective precipitation both in January and July is highly sensitive to CP schemes dominated by orographic distribution. WRF-simulated precipitation differences arise because all four cumulus schemes parameterize the orographic influences differently. This study's results agree with those of Mooney *et al.* (2013) [69] who carried out WRF-model sensitivity experiments over Europe.

3.2.2 Thermodynamic Characteristics of Precipitation Bias

The above analysis demonstrated subjective validation of the monthly mean precipitation simulated by the four CP schemes against DAYMET observations. From the spatial distribution of precipitation bias plot, it is difficult to identify the cause of observed differences.

The sensitivities of WRF-model CP schemes were tested by several scientists (Collier, 2007 [18]; Lin *et al.*, 2008 [55]), who reported substantial precipitation biases over North America in summer. Nevertheless, very few researchers have tried to identify the cause of the biases, due to lack of available observational data. Moreover, precipitation is a highly uncertain meteorological variable, dependent on topographic distribution, proximity to sea and lakes, and the latitude and longitude of study areas. Therefore, this section aims to expose the cause of the differences in precipitation bias comprehensively, considering the vertical profiles of area-averaged specific humidity (a measure of dryness), vertical velocity, skew temperature, and upper air charts at different pressure levels. It also examines individual precipitation events instead of the above monthly mean climatology, thus explicitly focusing on the physical mechanism behind simulated precipitation differences.

Figure A.0.3, depicting the spatial distribution of 3-hourly (from 0600 UTC to 0900 UTC) accumulated grid and sub-grid scale precipitation on 23 July 2002, shows several discrepancies. First, no cumulus precipitation is observed over southern Ontario. Secondly, a patch of grid-scale precipitation is observed along the northern shores of Lakes Erie and Ontario. A closer look also reveals that the simulation from the BMJ CP scheme produces more grid-scale precipitation than the other three schemes. The causes for this difference cannot be identified by simply looking at the spatial distribution of precipitation. Therefore, this study has tried to clarify the underlying physical mechanism by analyzing the vertical profile of domain-averaged specific humidity, vertical velocity, and skew temperature.

First, this analysis looked at the vertical profile of the 3-hour evolution of specific humidity profile from 2100 UTC on July 23 to 0900 UTC on July 24 (Figure A.0.4). At 2100 UTC the BMJ CP scheme clearly simulated a lower specific humidity profile than the other three CPs in the lower atmosphere (below 800 hPa). However, over time, the specific humidity profile simulated by the BMJ CP showed significantly higher values than the others. Between 0600 UTC and 0900 UTC , when the sun heated the surface, an inversion occurred in the lower atmosphere. To understand why the BMJ CP scheme simulated higher specific humidity after midnight, the vertical profiles of 3-hourly evolution of the vertical wind component for the same time period were inspected. Figure A.0.5 illustrates that the BMJ CP-scheme-simulated vertical-velocity profile is significantly lower than that of the other three schemes during the night. This study hypothesizes that the lower vertical velocity simulated by the nighttime BMJ CP scheme results in less moisture being transported to the upper atmosphere than with the other three CP schemes.

Individual Precipitation Event 1 (July 23, 2002)

To investigate whether excessive night-time moisture can produce a low level cloud, the 3-hourly evolution of skew temperature profiles from 23 to 24 July were plotted, and showed that complete saturation occurred at 0600 UTC on July 23 in the lower to middle atmosphere (Figure A.0.6). After the precipitation at 0900 UTC, the atmosphere stabilized.

As the weather forecasting community knows well, a CP is said to be overactive if the model generates excessive precipitation where convection originates and too little downstream. On the other hand, it is said to be under-active if it produces a lot of total precipitation but mostly in a non-convective form (stratiform precipitation). An under-active CP scheme produces a too-moist lower and middle atmosphere, resulting in excessive latent heat release in the lower to middle troposphere with the MP scheme. Excessive moisture and latent heat at the lower to middle atmosphere ultimately produce too much low and mid level cloud, and finally, grid-scale precipitation with the MP scheme. Therefore, based on the above thermodynamic characteristics, it is possible to say the BMJ scheme falls into the category of an under-predictive CP scheme.

Convective Available Potential Energy

The convective available potential energy (CAPE), which measures the amount of energy available for convection for different cumulus schemes, is shown in Figure A.0.8, valid at 0600 UTC on July 23. The spatial distribution of CAPE shows that a mesoscale convective system (MCS) is crossing over the Great Lakes. A closer look reveals that the MCC's trailing edge is still over Lake Erie with the BMJ CP scheme, but has already passed it with the other three schemes. In the presence of a large scale front, excess moisture in the lower level produces lower to mid level cloud, resulting in low precipitation by the MP scheme. Figures A.0.9 and A.0.10 illustrate CAPE at 1500 UTC, July 23 and 0000 UTC, July 24, respectively. During daytime, all CPs simulate equal amounts of CAPE, but at midnight under calm conditions, the BMJ CP scheme underestimates as a consequence of simulated lower vertical velocity.

Individual Precipitation Event 2 (July 28, 2002)

Figure A.0.11 shows the spatial distribution of 24-hours of accumulated grid and sub-grid scale precipitation from 0000 UTC of July 28 to 0000 UTC of July 29. Once again, the BMJ CP scheme overestimates grid-scale precipitation. Figure A.0.12 represents the

accumulated WRF-simulated precipitation bias from the innermost domain. Both the skew-temperature and vertical wind profiles indicate that the BMJ scheme produces weak wind during the night and transports less heat and moisture to higher atmospheric layers, resulting in excessive lower-atmosphere moisture. Grid-scale precipitation generates when an MCS crossover brings saturation into a stable atmosphere with relatively high moisture content. This same mechanism produced excessive rainfall in the case of the BMJ scheme in the northern side of Lake Erie. The two individual precipitation events show that the BMJ CP scheme presents a persistent wet bias along the northward side of Lake Erie. The other three schemes give a persistent wet bias around the Blue Mountain area. The later part of this study revealed that the precipitation biases over southern Ontario mainly come from inadequate representation of the boundary layer process.

Taylor Diagram Analysis of Total Precipitation

Figure 3.8 represents the Taylor statistics (Taylor, 2001 [94]) and portrays the correlation coefficient (CC), normalized standard deviation (NSD), and root mean square difference (RMSD) of the WRF-simulated total precipitation (RAINC+RAINNC) for the four CPs, as listed in Table 2.3 relative to DAYMET observations for January (left column) and July (right column). In January, the precipitation simulated by all CPs shows a lower relationship relative to the DAYMET observations in terms of the correlation coefficient (slightly 0.3), RMSD, and variability about the mean. Close clustering of the simulated points indicates lower variability in the January precipitation.

Unlike January precipitation, July precipitation agrees better with DAYMET gridded observations. The RMS difference is very high for simulated July precipitation. During summer months over North America, thermally driven convection is a major trigger of convective rainfall. Therefore, CPs contribute a significant amount of rain in the simulated precipitation as a byproduct while stabilizing the atmosphere. As expected, a higher CC ($0.6 \sim 0.7$) was observed for July precipitation. Precipitation simulation using the KF convection scheme agrees well with the DAYMET observations, and shows the highest CC (~ 0.7), lowest RMSD (~ 0.7), and variability about the mean. The NSAS scheme shows the highest RMSD (>1.5), while the BMJ scheme gives the lowest CC (~ 0.3). In the July precipitation plot, CC increases, and RMSD error and variability decrease when feedback is turned on between the inner nest and parent domain. The impact of feedback in January is not significant.

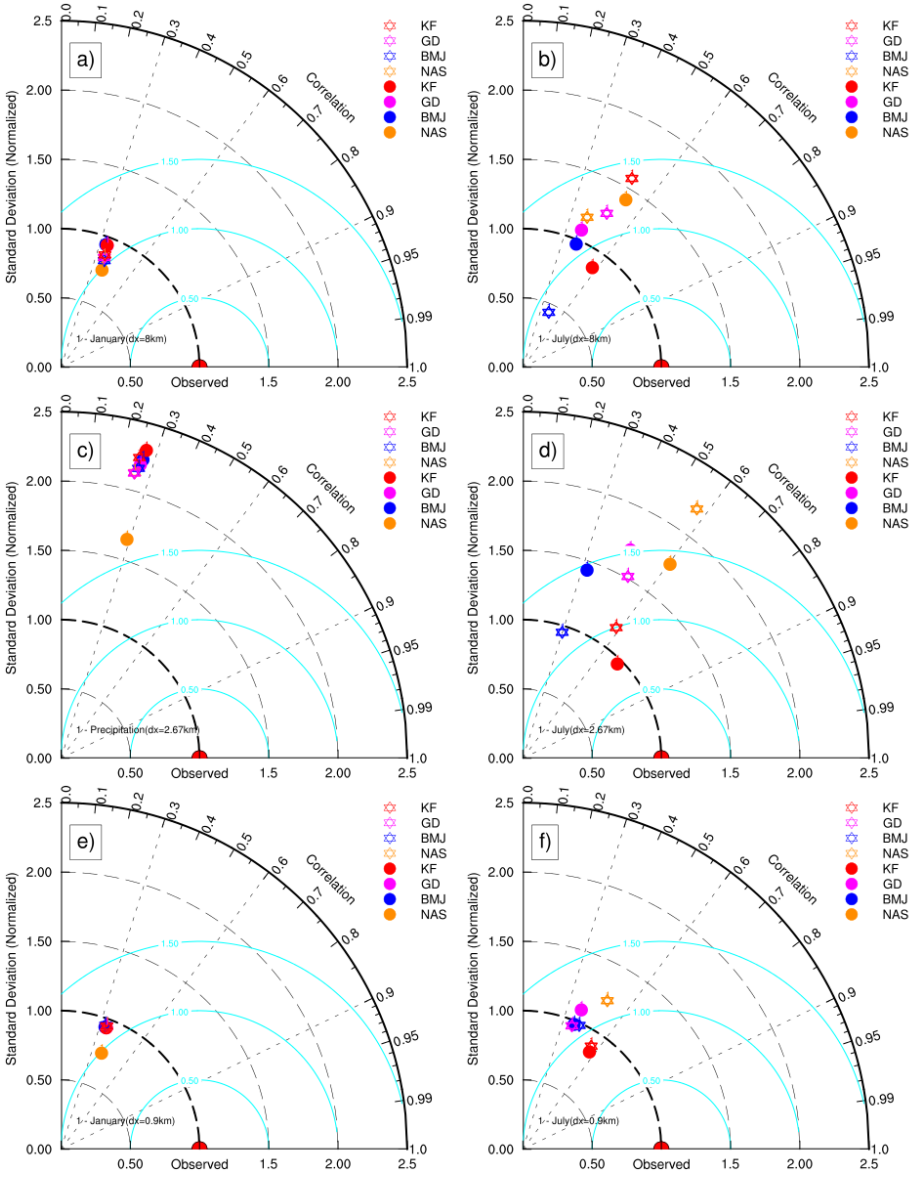

Figure 3.8: Taylor diagram showing correlation coefficient, normalized standard deviation and root mean square differences of the simulated WRF total precipitation (RAINC+RAINNC) for four convective parameterization schemes as listed in Table 2.3 relative to DAYMET observations for January (left column) and July (right column). KF (red), BMJ (blue), GD (magenta), and NSAS (dark orange). Solid circles represent simulations with feedback turned on between the inner nest and parent domain, while void stars represent simulation feedback turned off. The 1st, 2nd, and 3rd rows represent results from the outermost domain, intermediate domain, and innermost domain, respectively.

In summary, the results for precipitation show a significant dependence on CP, in particular BMJ and KF. KF is an overactive, while BMJ is under-active. The NSAS CP scheme performs slightly better than the BMJ scheme. On the other hand, GD CP scheme's performance falls between those of KF and NSAS, although it shows underestimation over the Great Lakes.

3.2.3 Temperature

Figure 3.9 compares simulated and observed skew temperatures (skew-T) and dew point profiles; simulated vertical wind profiles at Detroit, Michigan (left) and Buffalo, New York (right) radiosonde stations at 1200 UTC on 29 July for the four CP schemes (sounding station locations are shown in Figure 2.2). KF shows better agreement with in situ radiosonde observations at both locations. KF simulated dew point profile agreed best with the observed profile from 850 to 700 hPa. The NSAS, GD, and BMJ cumulus schemes come second, third, and fourth, respectively, in terms of dew point profile performance within the above atmospheric layers. An upper level chart can explain the skew temperature and dew point profiles' differences simulated with different CPs. The upper level charts for the four CP schemes at 850 hPa are shown in Figure 3.10, which illustrates the simulated temperature, relative humidity, geopotential height, and wind speed (in Knots) on July 29, 2002, at 1200hr local time. It is clearly seen from the contour plot that, unlike the KF scheme, the other three cumulus schemes underestimate relative humidity over the Detroit station.

Simulated vertical profiles of the specific humidity (SH) and vertical wind at the above two locations are presented in Figure 3.11. The high vertical velocity simulated by the GD scheme clearly transported more moisture from 850 to 700 hPa in the upper atmosphere (Figure 3.9), resulting in the driest SH profile in Figure 3.11.

For the Buffalo station, the observed wind barb is in close agreement with the BMJ-simulated wind barb (Figure 3.9), and the BMJ-simulated dew point profile corresponds closely with the observed dew point profile. Again, the SH profile resembles the vertical wind profile and further confirms their complementary relationship (Figure 3.11). When compared with 0000 UTC radiosonde observations, the WRF-simulated dew point profile at the Buffalo station shows a drier mid atmosphere on July 23 and a relatively wet middle atmospheric dew point profile on July 30 with all four schemes (Figure 3.12). Comparisons of skew-T, dew point, vertical wind, and SH demonstrate that the accuracy of the vertical wind component determines the accuracy of simulated temperature and dew point profiles.

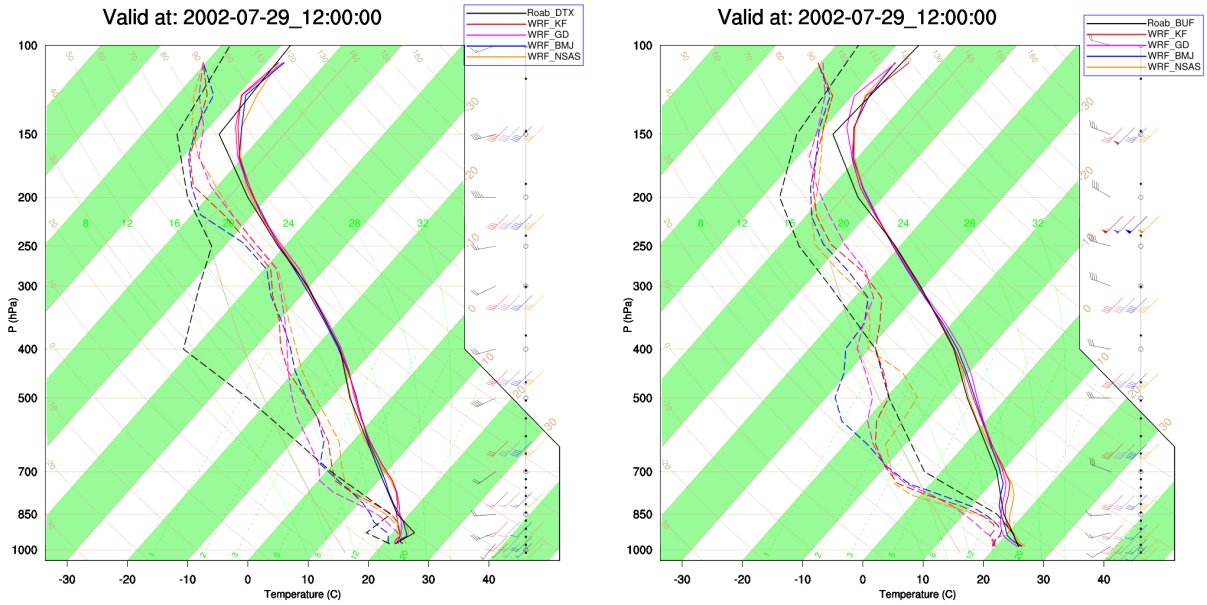

Figure 3.9: Simulated and observed skew temperature profiles at Detroit (World Meteorological Organization ID: DTX), Michigan (left) and Buffalo (World Meteorological Organization ID: BUF), New York (right), valid on July 29, 2002, at 1200 UTC.

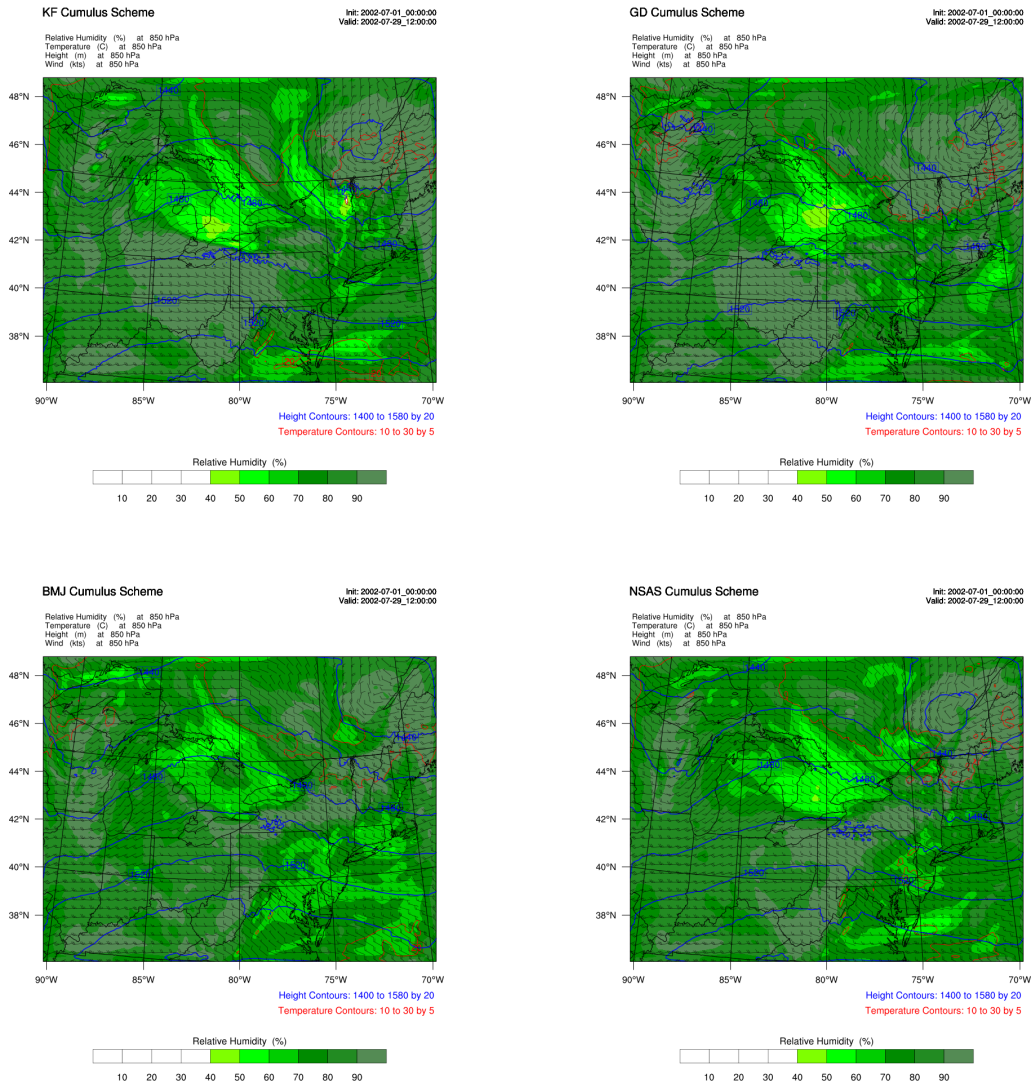

Figure 3.10: Upper air chart at 850 hPa: valid at July 29, 2002, 1200 UTC time

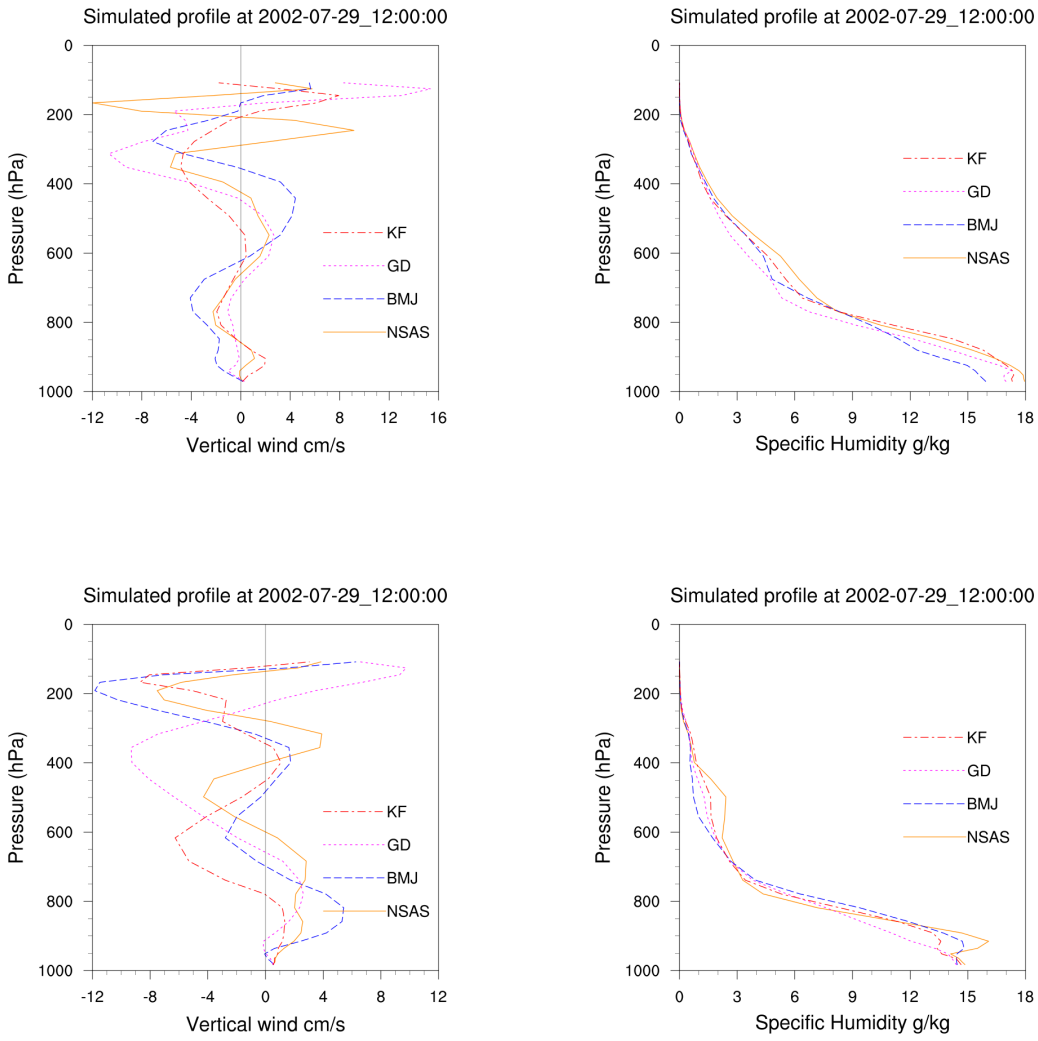

Figure 3.11: Simulated vs Observed vertical profiles of specific humidity and vertical wind at Detroit (top row) and Buffalo stations (bottom row); valid at 1200 UTC July 29, 2002.

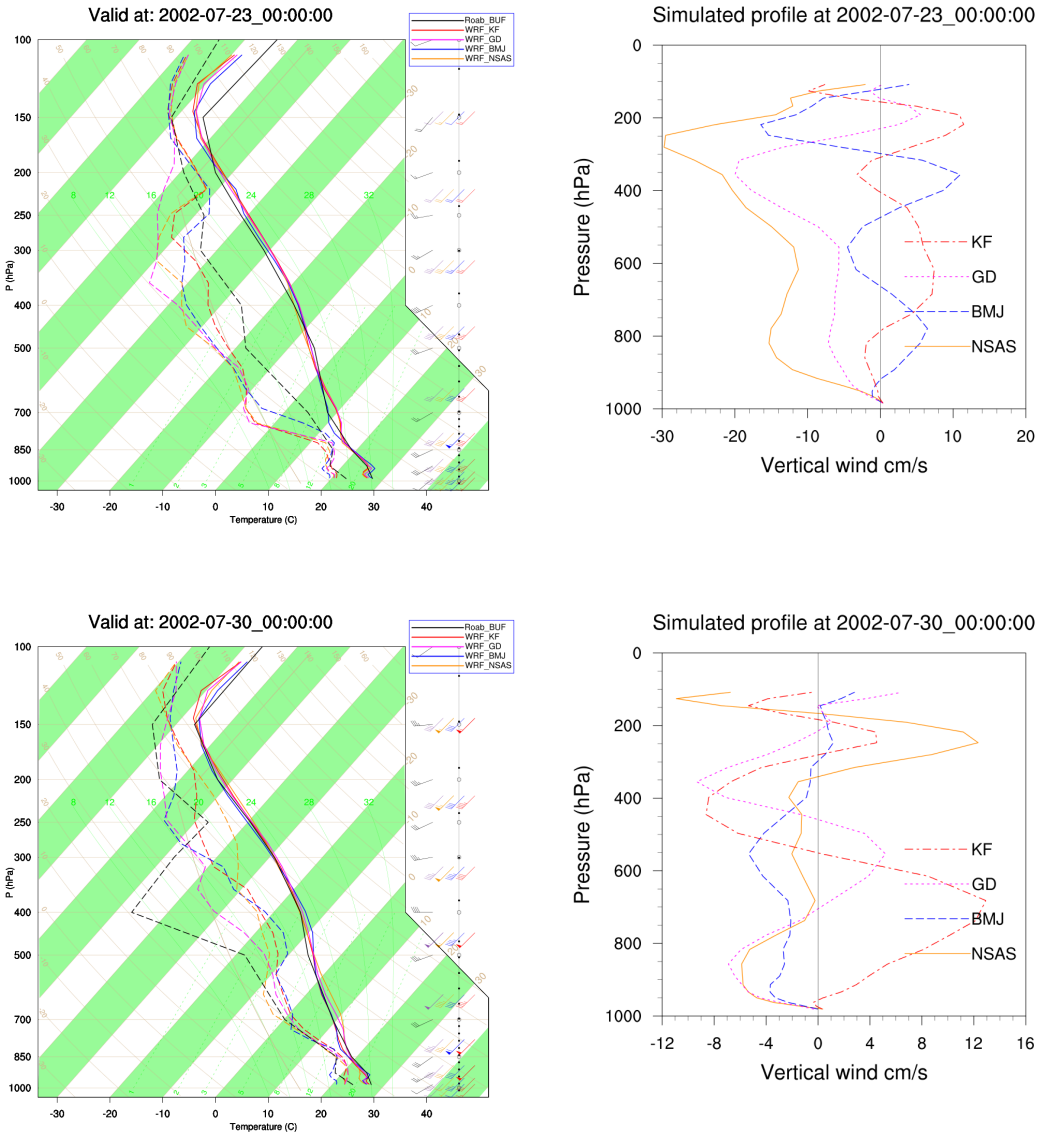

Figure 3.12: Simulated and observed Skew-T profile along with simulated vertical wind profiles at Buffalo, New York, at 0000 UTC 23 (top row) and 30 (bottom row) Jul 2002, for the four cumulus parameterization schemes.

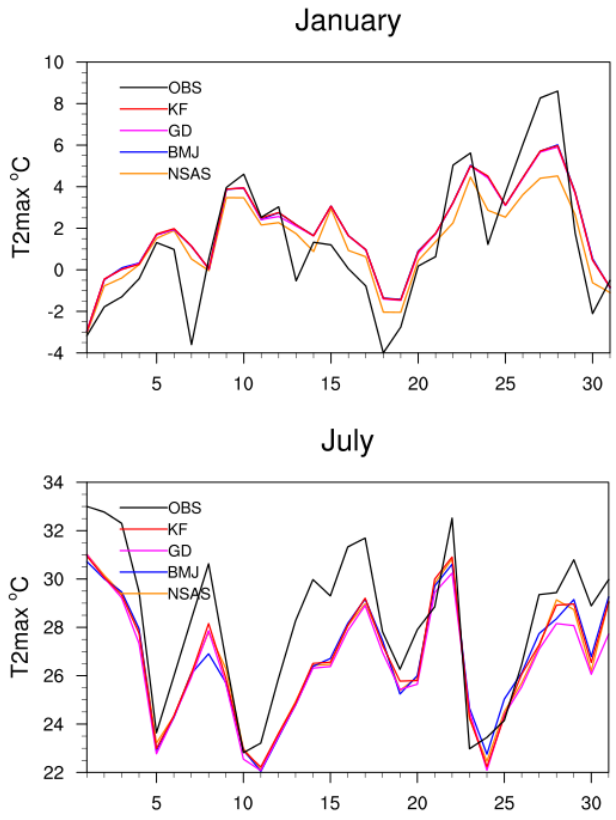

Figure 3.13: Time-series of the simulated daily maximum surface air temperature at a two-meter height from the Earth surface. In all cases, green solid line represent DAYMET observations.

In January, WRF-simulated T2max showed the same diurnal variability as observed

(Figure 3.13). The model underestimated simulated extreme temperatures. All schemes except NSAS gave the same temperature pattern. The NSAS was closer to observations. The model consistently overestimated T2min in all cases (not shown). It is also observed that, at the beginning of integration, there were no differences among the four CPs. However, after day 10, the BMJ started to deviate from the other three, becoming closer to the observed T2min. Comparison of T2max and T2min indicates that WRF underestimates T2max but overestimates T2min with respect to DAYMET observations. The model-simulated T2mean captured the observed diurnal cycle well, although it underestimated magnitude (not shown). The model realistically reproduced the observed mean temperature very well, with temperature variability clearly higher in July than January. The July temperature shows a sensitivity to CP that was absent in January simulations. Time series analysis clearly shows that temperature underestimation is higher in colder months than in warmer months. Overall, the NSAS CP scheme is best at simulating the diurnal cycle of all three temperatures.

In January, all CPs, except NSAS showed the same T2max distribution over southern Ontario (Figures 3.14). They also systematically underestimated the T2max in the lower half, while showing zero bias in the upper half of the domain. In general, the three CPs showed good reproducing skill, as the biases are within the range of -0.8° to $+0.5^\circ$ C in most parts of the domain. However, NSAS showed a wide-spread cold bias over the whole domain (Figures 3.14 a-c). In July, all four CPs showed a warm bias in the interior of the domain, where precipitation is underestimated (Figure 3.15). The assumption is that this warm bias in T2max results from an underestimation of precipitation. The July T2max bias lies in the same range as the January T2max one.

January T2min is overestimated by all CPs except NSAS, which shows small cold bias over areas where forest is present (not shown). The bias range for T2min is slightly higher than that of T2max over most of the domain. Nevertheless, simulated temperatures show a positive bias up to $> 4^\circ$ C. Unlike that of January, the July T2min was captured well by all CPs (not shown). NSAS and BMJ showed a positive bias over the entire domain. However, KF and GD CPs exhibited small negative bias in the north-western part of southern Ontario.

The T2mean temperature for January shows a gross overestimation by all CPs (not shown) except the NSAS scheme. It displays a cold bias in the eastern part of the domain, plus a narrow band of warm bias along the shores of lake Huron. Of the four CPs studied, the NSAS showed the lowest T2mean bias. The other three schemes exhibited the same bias over the entire domain. The WRF model exhibited excellent agreement with DAYMET observations in the case of the July T2mean temperature. The T2mean biases range from -0.5° to $+0.5^\circ$ C in most parts of the domain.

The temperature analysis results suggest problems in all CPs tested. No single scheme outperformed the others while simulating all three temperatures. It must be noted that some of the biases in temperature could result from incorrect representation of SW and LW radiation processes. Surface temperature forecasting is more dependent on proper parameterization of SW and LW radiation schemes than convective parameterization; hence, it would be wise to include results from their sensitivity studies. Another source of uncertainty could be inadequate representation of soil moisture and soil texture data sets during model initialization.

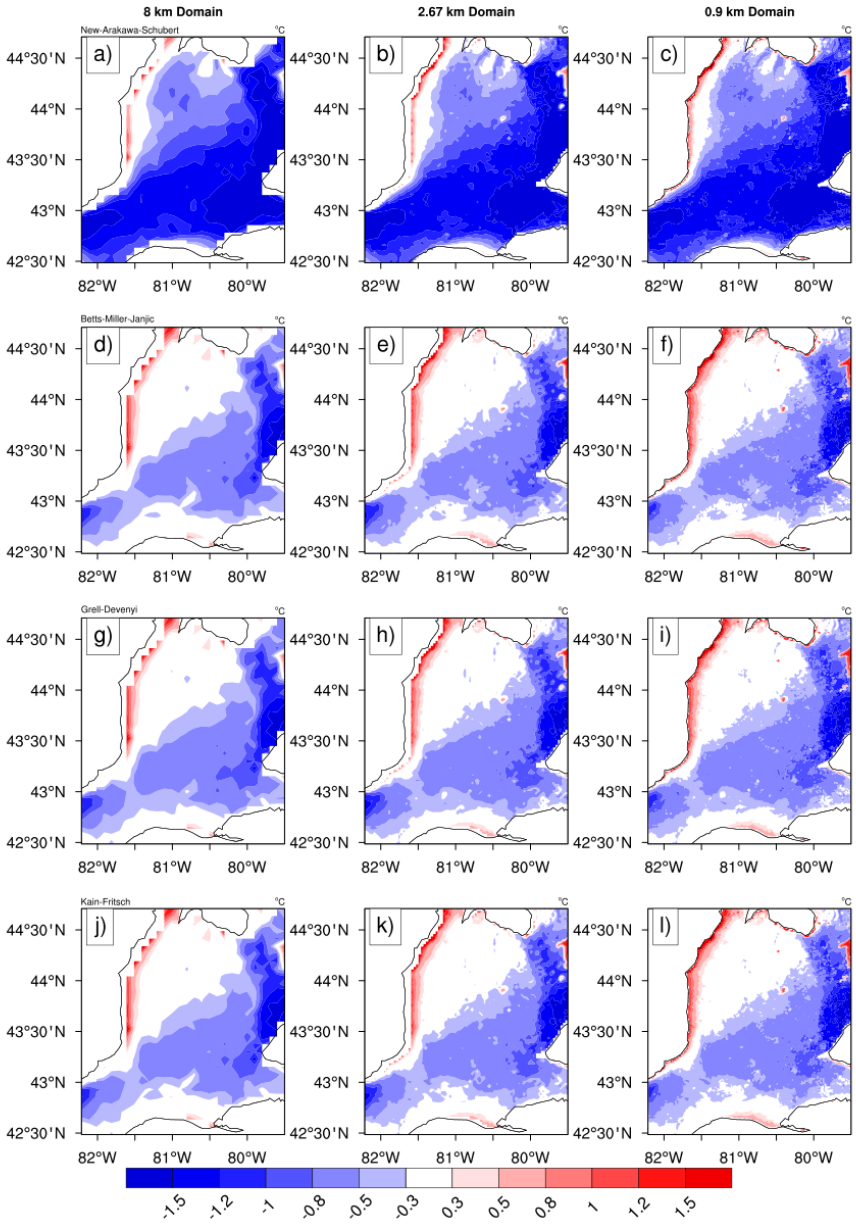

Figure 3.14: The spatial distribution of monthly mean maximum temperature bias in ° C for January 2002. Sensitivity to different cumulus schemes: New simplified Arakawa Schubert (a, b, and c), Betts, Miller and Janjic (d, e and f), Grell-Devenyi (g, h, and i), and Kain-Fritsch (j, k, and l). Sensitivity to grid spacing: 8km domain (left column), 2.67km domain (middle column) and 0.9km domain (right column).

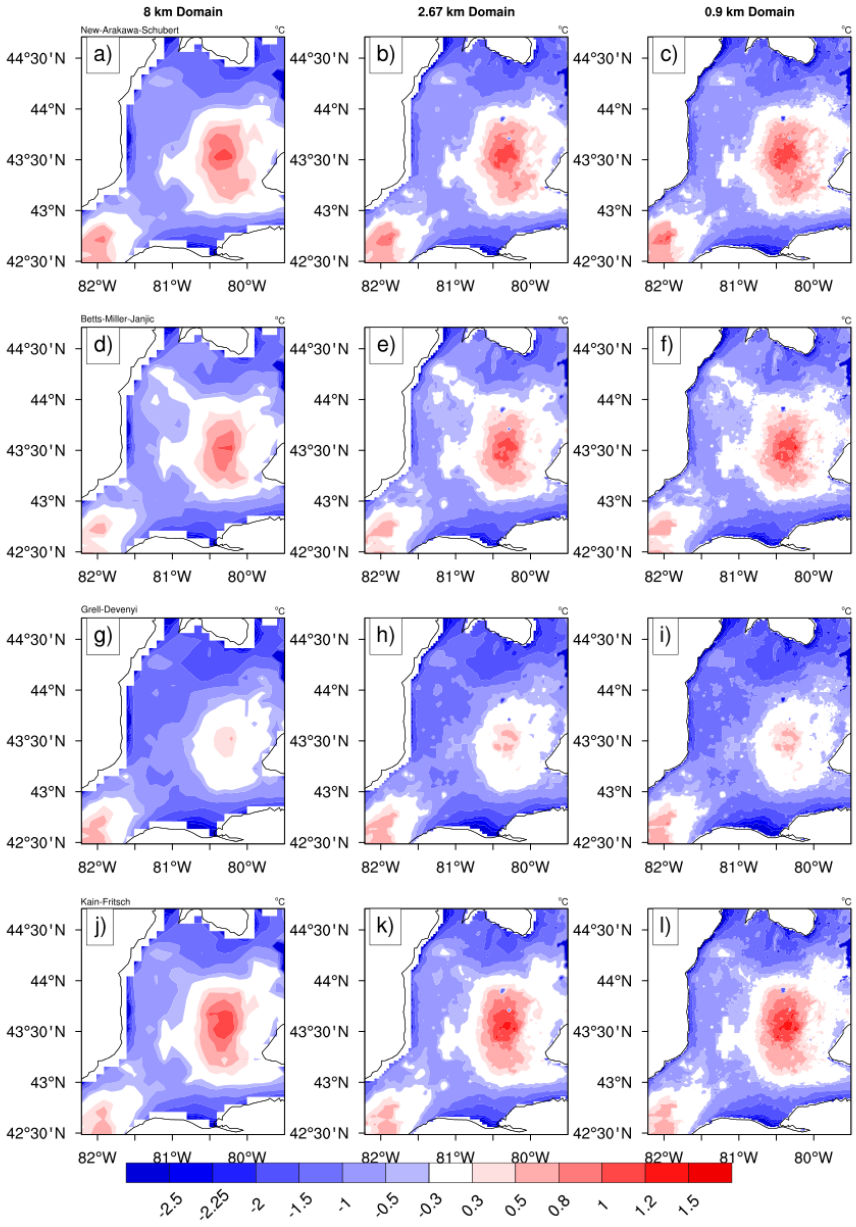

Figure 3.15: As in Figure 3.14 but for July 2002.

The Taylor diagram (Figure 3.16) indicate that the simulated daily T2max is in good agreement with the DAYMET observations, with a CC $\geq$ 0.9. The model gave a CC $\geq$ 0.95 for the other two temperatures. For all three temperatures, close clustering of the

simulated values both in January and in July clearly indicate that simulated temperatures are not very sensitive to CP. The RMSD for all three temperatures range from 0.25 ° to 0.5 ° C, which proves WRF's excellent capabilities to reproduce observed temperature patterns.

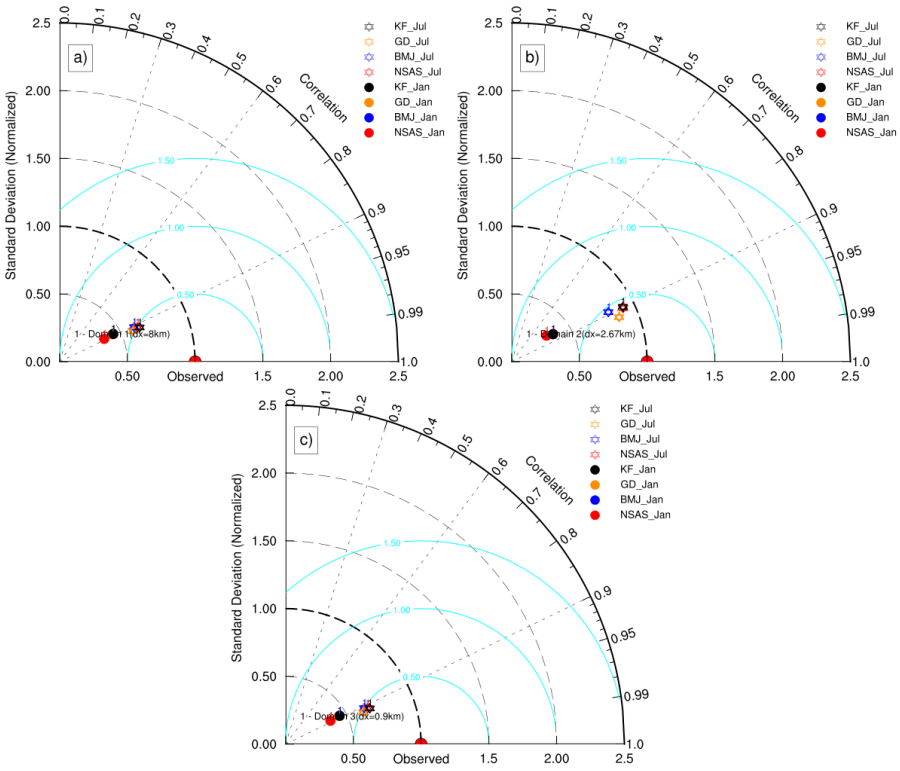

Figure 3.16: Taylor diagram showing correlation coefficient, normalized standard deviation, and root mean squared difference of daily maximum temperature (T2max) relative to DAYMET observation for the four cumulus parameterization schemes, listed in Table 2.3, for January (solid circle) and July (void star), 2002.

3.3 Conclusions

This study examined the sensitivity of WRF model convective parameterization schemes over the Great Lakes basin, by investigating the sensitivity of total precipitation (RAINC + RAINNC), daily maximum, minimum, and mean temperature to four cumulus parameterization schemes (Table 2.3). We compared model simulations, both qualitatively and quantitatively, against various observations, using multiple matrices to establish a broad and robust understanding of the CP schemes' performance.

Time series analysis of simulated precipitation showed overestimation in July but underestimation in January. WRF performed poorly while simulating extreme precipitation events in July. During summer, when convection is a crucial trigger of mid-latitude rainfall, simulated precipitation using the Kain-Fritsch (KF) cumulus parameterization scheme shows a higher pattern correlation coefficient (CC), lower normalized standard deviation (NSD), and lower root mean square difference error (RMSD) than the other three schemes studied. In January, when snow dominates local precipitation, no one cumulus scheme is superior. Minimum biases are observed in simulated temperatures using the KF scheme. In July precipitation, CC increases, and RMSD error and variability decrease when feedback is turned on between the inner nest and parent domain. The impact of feedback in January is not significant. Thermodynamic-characteristics analyses affirmed that the BMJ falls into the category of an under-predicting CP scheme.

The simulation results for the surface air temperature model confirmed that it can capture spatial heterogeneity; however, the magnitude is systematically underestimated. The underestimation is higher in colder months than in warmer ones. Simulated WRF-model temperatures showed very low sensitivity to the choice of convective parameterizations.

In summary, precipitation was also found to be more sensitive to the selection of convective parameterization than temperature. Overall, among the four cumulus schemes, the KF showed the best performance. This study has demonstrated that the Great Lakes play an important role in the atmospheric conditions of southern Ontario, ranging from the diurnal to the seasonal timescales. The results of this study give us more confidence in adopting the KF convective parameterization scheme for any WRF experiments over the Laurentian Great Lakes regions.

Chapter 4

Sensitivity Study of the WRF Model Planetary Boundary Layer Parameterization Schemes

4.1 Fundamentals of Planetary Boundary Layer (PBL) Parameterization

In the lower troposphere, turbulent layers develop due to surface heating, wind shear, and friction. PBL parameterization schemes, using various methods, are used to represent the upward transport of various surface fluxes, including heat, momentum, and moisture, by turbulent eddies. The order of interactions of the PBL physical processes among the various schemes also varies considerably, resulting in different structures for the boundary layer profile (Hu *et al.*, 2010 [40]).

PBL schemes that use first-order closure solve four partial differential equations (PDE). They approximate turbulent fluxes of momentum ($\overline{u'w'}$, $\overline{v'w'}$), heat ($\overline{w'\theta'}$), and species ($\overline{w'c'}$) using known variables, i.e., mean velocity ($\bar{U}$, $\bar{V}$, $\bar{W}$), mean temperature ($\bar{\Theta}$), and mean concentrations ($\bar{C}$), respectively. Any first-order scheme ignores third or higher order terms such as, $\overline{u'u'w'}$, $\overline{v'v'w'}$, etc., and needs only routinely measure or model resolvable meteorological variables to explicitly determine an eddy diffusivity coefficient.

Stull (1988) [93] described an idealized atmosphere-horizontally homogeneous, dry, with no subsidence-by the following prognostic equations:

$$\begin{aligned}
\frac{\partial \bar{U}}{\partial t} &= f_c(\bar{V} - \bar{V}_g) - \frac{\partial(\overline{u'w'})}{\partial z} \\
\frac{\partial \bar{V}}{\partial t} &= f_c(\bar{U} - \bar{U}_g) - \frac{\partial(\overline{v'w'})}{\partial z} \\
\frac{\partial \bar{\Theta}}{\partial t} &= -\frac{\partial(\overline{u'\theta'})}{\partial z}
\end{aligned} \tag{4.1}$$

The momentum ($\overline{u'w'}$, $\overline{v'w'}$) and heat ($\overline{w'\theta'}$) flux components in equation (4.1) are second moments and have no prognostic equations. To solve eqn. (4.1) one could approximate the above flux components in terms of known variables $\bar{U}$, $\bar{V}$, $\bar{W}$. One of the simplest turbulence closure techniques is gradient transport theory, or K-theory, which calculates the flux of an arbitrary variable, ξ', using the following equation:

$$\overline{u_j'\xi'} = -K\,\frac{\partial \bar{\xi}}{\partial x_j} \tag{4.2}$$

where K is a scaler with units of $m^2 s^{-1}$. The K is also called the eddy viscosity/eddy diffusivity/eddy-transfer coefficient/turbulent-transfer coefficient/gradient-transfer coefficient.

PBL schemes that use second-order closure assumptions need to solve prognostic equations consisting of higher-order terms or their derivatives such as: u', v', w', $\overline{u'w'}$, $\overline{v'w'}$, $\overline{w'\theta'}$, $\overline{w'q'}$, ..., etc. Nonetheless, a PBL scheme using n^th order closure will keep only those terms that have the order n+1 and smaller.

Like first-order ones, some PBL schemes solve a set of prognostic equations not only for the mean properties, but also for turbulent kinetic energy (TKE) and are hence called one and half-order schemes. The MYJ scheme uses one and half order closures. PBL schemes that use turbulent kinetic energy (TKE) closure to calculate the eddy viscosity coefficient K are more physically realistic, as they include more atmosphere physics, and users need to solve six partial differential equations (PDEs). More complex schemes that use second-order closure require solving of at least fifteen PDEs.

4.1.1 Classification of PBL Schemes

Based on their closure assumption, PBL parameterization schemes are divided into two main classes: local and non-local. The former assumes that the turbulent transport of surface fluxes explicitly depends on local values. Variables and parameters in a NWP model's

grid box are described only by the corresponding model level or values from neighboring grid boxes. Local schemes use mean state of atmospheric variables and/or their gradients to calculate turbulent fluxes at each grid point of the model domain. This assumption is less plausible during convective conditions, when turbulent fluxes are dominated by large eddies that transports air parcel at longer distances (Troen and Mahrt, 1986 [102]; Stull, 1984 [92]). Non-local schemes, in contrast, assume that parameters can depend on the whole vertical profile, or on relationships between separated levels (e.g., diffusion coefficients dependent on the PBL thickness). The four PBL schemes examined this study are briefly described below.

4.1.2 The Yonsei University (YSU) Scheme

The YSU PBL scheme of Hong *et al.*, (2006) [38] is a first-order, non-local scheme that treats non-local fluxes implicitly and includes a counter gradient flux term in the eddy-diffusion equation. This counter-gradient flux term facilitates realistic development of a well-mixed layer. Nonlocal scheme carries surface moisture to a greater degree apart from the Earth surface to higher model level, thereby reducing cold bias in the surface temperature. In the YSU scheme, the flux of a scalar variable C can be represented by (4.3).

$$\frac{\partial C}{\partial t} = \frac{\partial}{\partial z}\left[K_c\left(\frac{\partial C}{\partial z} - \gamma_c\right) - (\overline{w'c'})_h\left(\frac{z}{h}\right)^3\right] \tag{4.3}$$

where $\frac{\partial C}{\partial z}$ and γ_c represent the local gradient for C and a correction term for the local flux, respectively. The role of γ_c is to include the influence of the large eddies in the local flux of C, whereas h denotes PBL height and is calculated using a critical Richardson number. Accordingly, K_c and $\overline{w'c'}$ represent the eddy diffusivity and average subgrid-scale turbulent vertical flux for scalar quantity C.

4.1.3 The Mellor Yamada and Janjic (MYJ) Scheme

Mellor, Yamada, and Janjic (1994) [42] developed a PBL scheme that uses Mellor and Yamada (1982) [60] 1.5-order (level 2.5) turbulence closure model to represent turbulence above the surface layer. This MYJ scheme uses prognostically calculated TKE to determine PBL height, and eddy diffusion coefficients. Several limitations have been reported, including the presence of excessive near surface moisture due to weaker vertical mixing, which also transfers less heat from the surface to higher layers during the day (Bright and

Mullen, 2002 [12]; Jankov *et al.*, 2007 [46]). The result is positive temperature biases in the ABL. MYJ scheme is also known to underestimate the entrainment of free-tropospheric air into the PBL, leading to not only lower PBL height but also a smaller potential temperature decrease. The scheme predicts lower temperatures and more moisture in the PBL during late afternoon.

4.1.4 The Mellor-Yamada-Nakanishi-Niino (MYNN2) Scheme

Nakanishi and Niino (2006) [71] proposed corrections to the MYJ PBL scheme of Mellor *et al.* (1994) [42] to overcome the insufficient convective-boundary-layer mixing [13]. Both are local schemes, but the former uses 1.5-order closure approximation. Of note, the MYJ shows lower temperatures and more moisture in the PBL during the day, and also underestimates of boundary layer height.

4.1.5 The Asymmetrical Convection Model version 2 (ACM2) Scheme

Pleim (2007a,b) [81, 82] took into account both local and nonlocal closure approaches in developing his asymmetrical convection model version 2 (ACM2), which represents boundary layer processes. This scheme's advantages are that for stable or neutral conditions, it shuts off non-local transport and uses local closure. It also includes a first-order eddy-diffusion component and the explicit non-local transport of the original ACM1scheme of [83].

4.2 Results

The results presented here focus on January and July of 2002. The sub-sections below present results from precipitation, temperature, sensitivity to PBL height evolution, and thermodynamic charecteristic analysis.

4.2.1 Precipitation

Figure 4.1 represents the temporal characteristics of domain-averaged precipitation for DAYMET-gridded-observations and simulations using different PBL schemes for January

(top panel) and July (bottom panel) 2002, respectively. As is evident from the January precipitation cycle (Figure 4.1 top panel), all the PBL schemes were able to capture the observed precipitation phase, except for one or two events. Although the PBL schemes show similar temporal fluctuations, they produce the largest variability while simulating heavy precipitation events. The YSU scheme produced the highest total precipitation, most of the time (Figure 4.1), and results in the highest accumulated precipitation totals in January (Figure 4.3). The YSU and ACM2 schemes, the non-local and hybrid PBL schemes, produced most spatially and temporally averaged monthly accumulated precipitation in January and July, respectively (Figures 4.2 and 4.3). In contrast, the MYJ scheme, a local-closure based PBL scheme, produced the least monthly accumulated precipitation both in January and July, although the difference with the other PBL schemes were small in July. In summary, the domain-averaged daily precipitation time series indicates dependency on the choice of PBL scheme, and the differences in monthly accumulated precipitation totals clearly indicate the different roles of local and non-local PBL schemes in transporting surface fluxes in different seasons.

To demonstrate the impact of different PBL schemes qualitatively, the mean spatial bias for total precipitation (convective + grid-scale) patterns for January and July are plotted in Figures 4.4 and 4.5, respectively. All schemes show nearly identical distribution of precipitation bias: slight underestimation over the interior of the domain but overestimation along the shores of the Great Lakes. Overall, the YSU scheme produces a wet bias, and the MYJ scheme a dry bias. The July precipitation shows a dry bias over the Grand River watershed and a wet bias over the south-western and north-western corners of the domain. There are several possible explanations for this bias; the most-probable is erroneous initial conditions of soil moisture, temperature, and texture. Of the four schemes, ACM2 gives the wettest bias in July, and MYJ, a lower precipitation distribution bias overall.

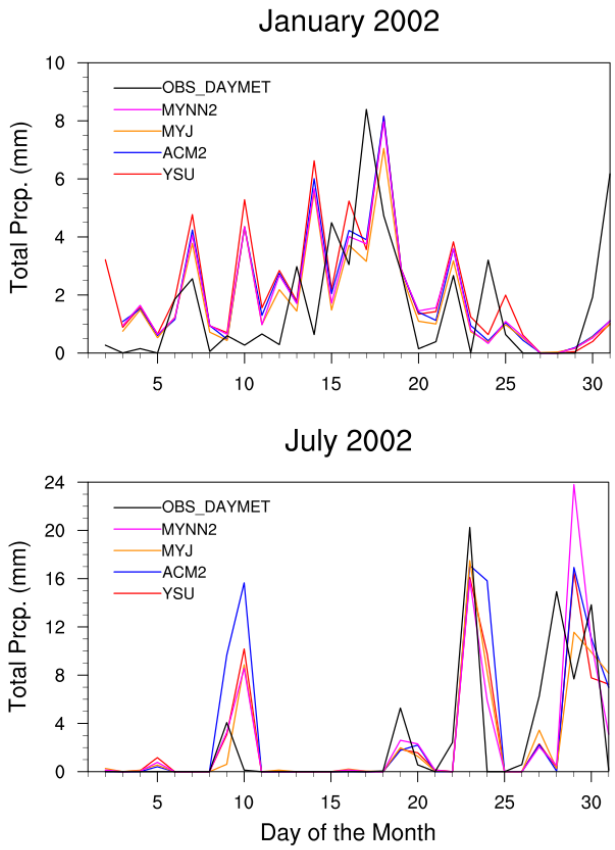

Figure 4.1: Domain-averaged daily time series of the DAYMET observation (black) and WRF-simulated total precipitation (RAINC + RAINNC) in mm using four PBL schemes: YSU (red), ACM2 (blue), MYJ (darkorange), and MYNN2 (magenta) from the innermost domain (d03).

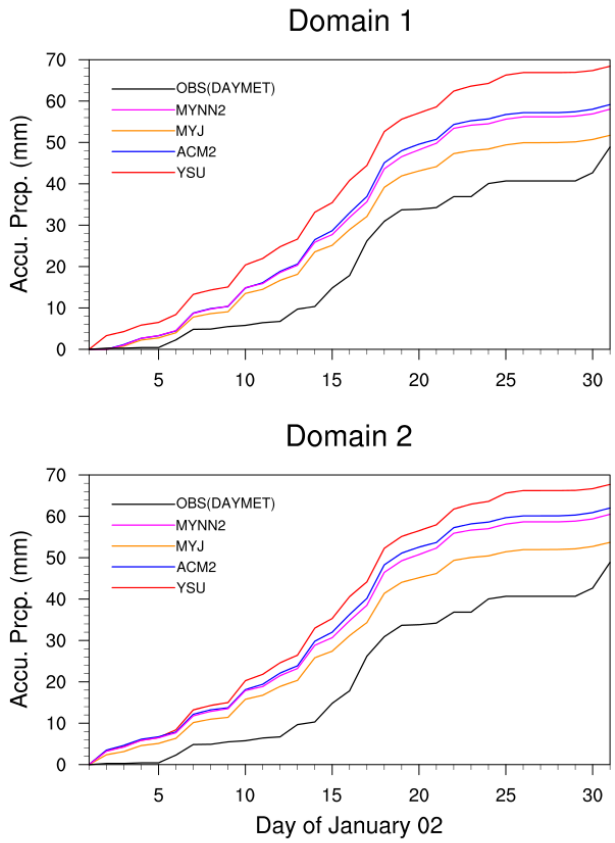

Figure 4.2: Temporal evolution of spatially and temporally averaged WRF-simulated accumulated total precipitation (mm) using four different PBL schemes (YSU(red), MYNN2 (magenta), ACM2(blue), and MYJ(yellow)) and DAYMET observations (black) from (a) Domain 1 (top panel) (b) Domain 2 (bottom panel) for January 2002.

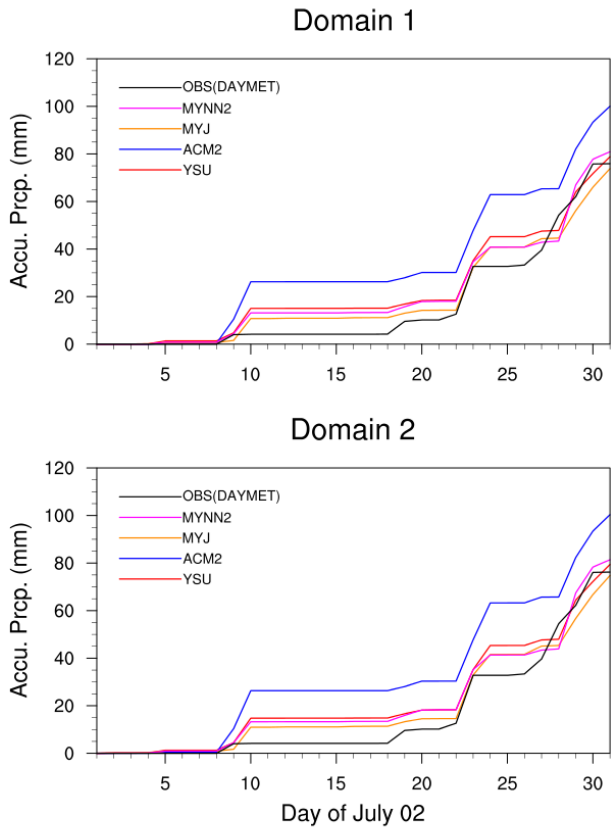

Figure 4.3: The same as Figure 4.3 but for July 2002.

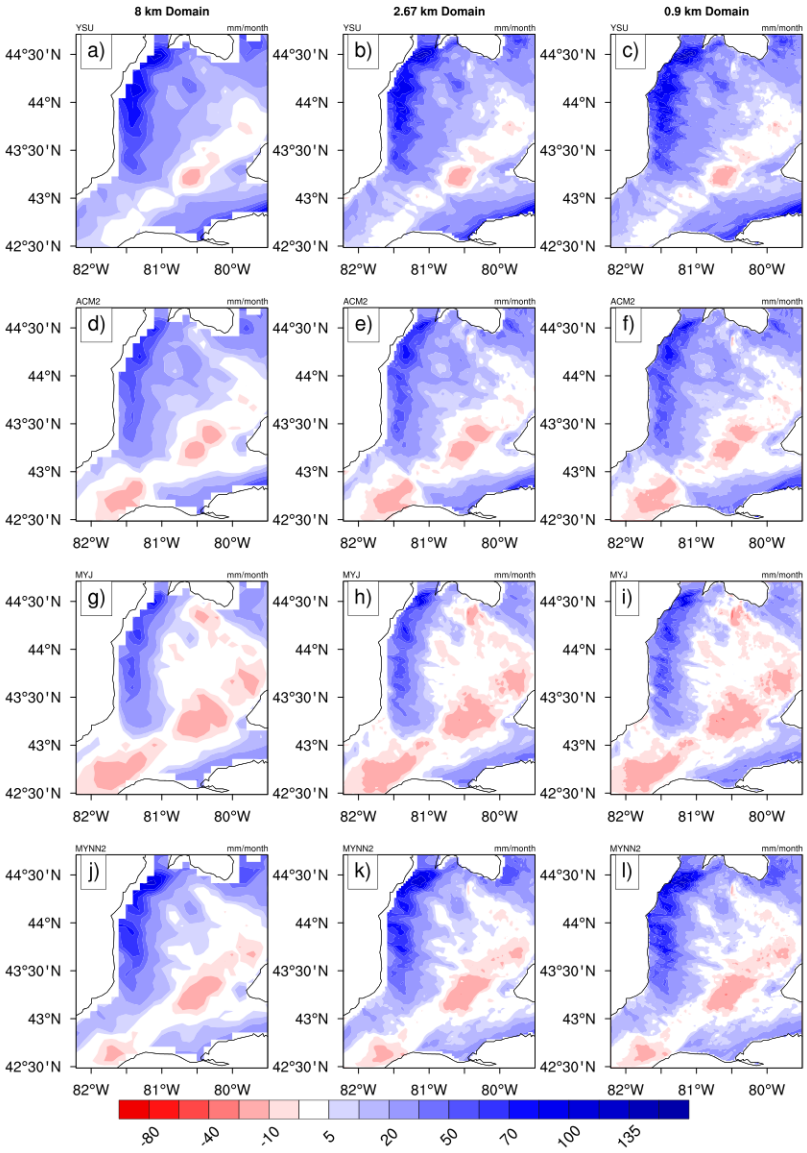

Figure 4.4: Spatial distributions of monthly accumulated total precipitation (mm) bias (WRF model - DAYMET gridded observation Observation) for January 2002. Results from the three nested domains: 8km, 2.67 km and 0.9km are illustrated from left to right column. Four PBL parameterization schemes are arranged from top to bottom as follows: YSU (first row), ACM2 (second row), MYJ (third row), and MYNN2 (fourth row)

.

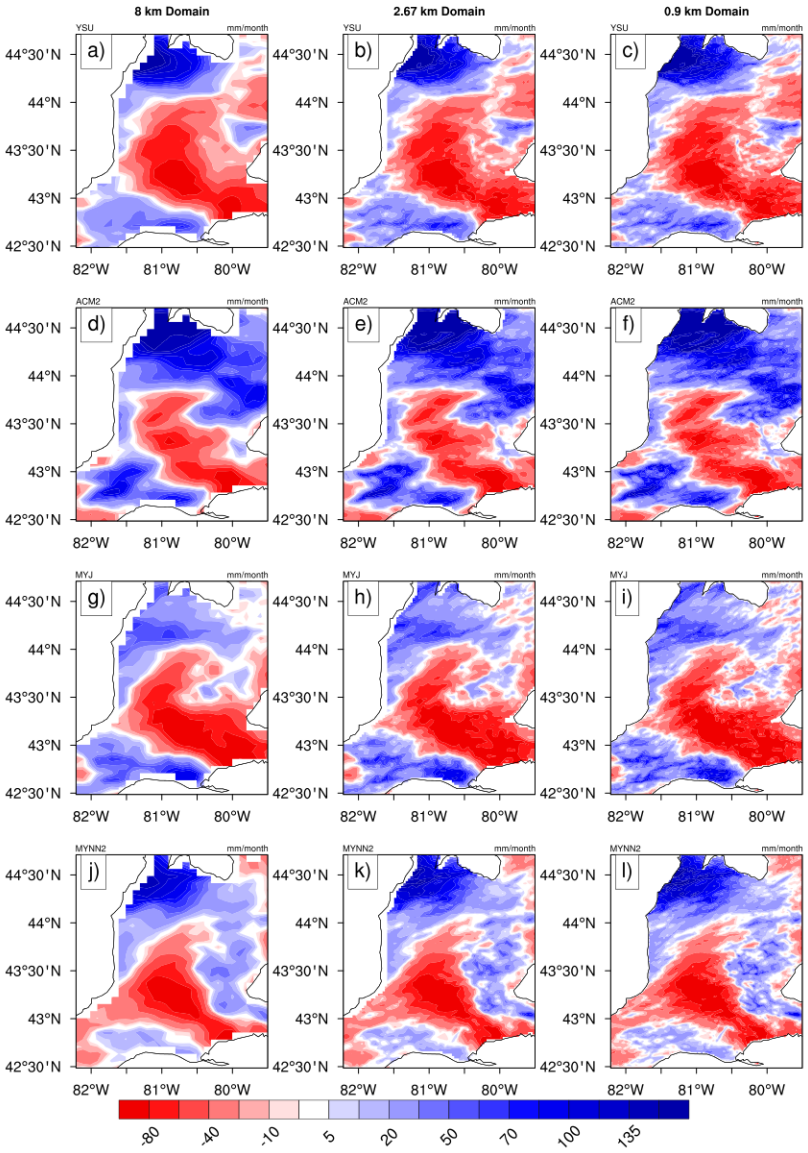

Figure 4.5: Same as Figure 4.4 but for July 2002.

The Taylor diagram (Figure 4.6) shows the CC, NSD, and RMSD of the WRF-simulated total precipitation (RAINC+RAINNC) relative to DAYMET observations for four. WRF-simulated precipitation shows CC of nearly 0.3 to 0.4 and 0.55 to 0.65 in January and July, respectively. Different values of CC in January and July indicate the different roles of PBL schemes in winter and summer months.

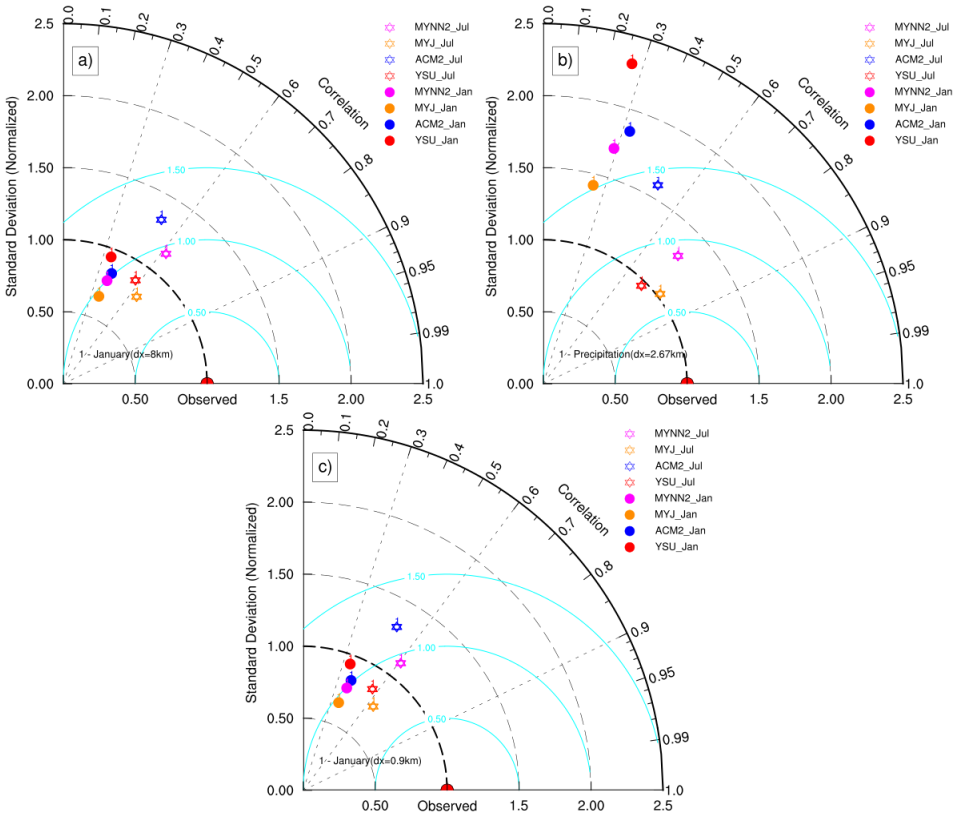

Figure 4.6: Taylor diagram showing correlation coefficient, normalized standard deviation, and root mean square differences of the WRF-simulated total precipitation (RAINC+RAINNC) for four PBL parameterization: YSU (red), ACM2 (blue), MYJ (dark orange), and MYNN2 (black) schemes relative to DAYMET observations. Solid circle and void star represent January and July simulations.

Precipitation shows low sensitivity to the choice of PBL scheme in January, when the boundary layer become more stable, than in July, when it is less so. The PBL schemes differ in their vertical mixing capacities resulting in different amounts of moisture transport to higher model levels. The result is differing amounts of precipitation. As expected from the earlier comparison of spatial distributions of monthly accumulated total precipitation, the MYJ run produces slightly higher pattern CC than the YSU run in both January and

July. In contrast, the YSU scheme produces slightly lower NSD than the MYJ scheme. Examining the Taylor diagram, it can be seen that, in July, the 2.67 km domain produces slightly higher CC and lower NSD and RMSD compared to the 8.0 km domain. However, in the case of domain 3 (0.888 km), model simulated precipitation shows decreased CC and an increased NSD and RMSD relative to domain 2 (2.67 km).

Figure 4.7 presents modeled vs observed probability density functions (PDF) for precipitation for January and July of 2002. For January, the PDFs of the four PBL schemes agree quite well with DAYMET gridded-observations. On the other hand, in July, the PDFs show many variabilities. Of the four schemes tested, the YSU receives the maximum skill score for reproducing an extreme precipitation event. The performance of the YSU scheme outperforms that of the others overall.

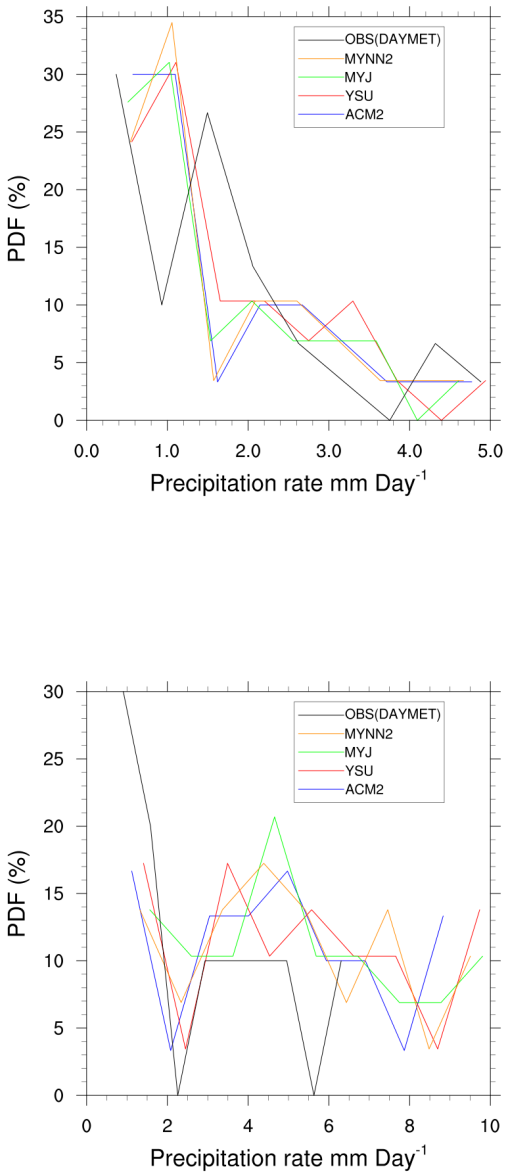

Figure 4.7: Probability density functions (PDFs) for precipitation for January (top panel) and July (bottom panel) of 2002 for the four PBL schemes listed in Table 2.4 and DAYMET observations.

4.2.2 Temperature

The spatial distribution of simulated January T2max (Figures 4.8) shows that the YSU scheme agrees quite well with DAYMET observations over a large part of the domain, whereas the ACM2 and MYNN2 schemes show an overall cold bias over most parts of the domain, being lower in the north-west and higher in the south-east of the domain. A generalized cold bias of less than 1.0 °C is observed in most parts of the domain with the YSU, ACM2, and MYNN2 schemes, reaching −2.0 °C in some areas. The MYJ scheme performed poorly while simulating the January T2max. It is easily distinguishable from the YSU, ACM2, and MYNN2 simulations that a relatively large bias is found along the shores of lake Ontario, especially over the cities of Toronto, Mississauga and Hamilton, where the land-use and land-cover patterns are very complex. It is to be noted that this study used no urban canopy model (UCM) or building energy model (BEM) in its WRF simulations. The UCM takes into account surface effects for roofs, walls, and streets, whereas the BEM is a multi-layer UCM model that can better represent properties of taller building, especially those that are higher than the lowest model levels. WRF experiments using UCM and BEM to identify these cities' role in diurnal temperature cycles can add invaluable information. However, that is beyond the scope of this study.

The domain-averaged root-mean-square-error (RMSE) of daily T2max, T2min, and T2mean temperatures are presented in Table 4.1. The YSU PBL scheme gives the lowest RMSE for daily T2max and T2mean temperatures, both in January and July. In contrast, the lowest RMSE for the T2min is given by the MYNN2 scheme. In most cases, the domain-averaged RMSE values range from 1.0 °C to 2.5 °C. The PBL schemes studied give nearly the same RMSE value, but the YSU scheme clearly outperforms the others.

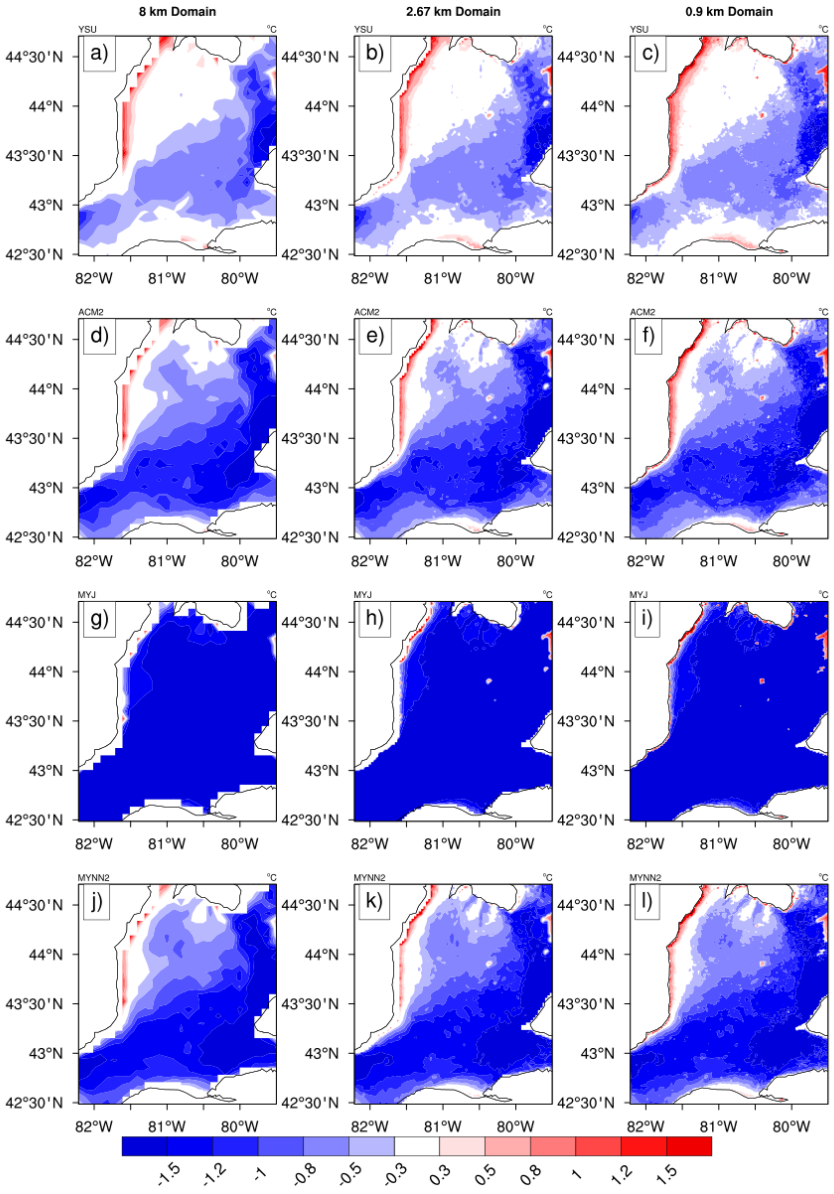

Figure 4.8: Mean maximum temperature bias (WRF-DAYMET) in ° C for the four different PBL schemes listed in Table 2.4 in January, 2002.

Figure 4.9 (a-c) represents the Taylor diagram (Figure 4.9 (a-c)) for daily T2max. A pattern CC $\geq$ 0.9 and RMSD $\leq$ 0.5, for all four PBL schemes demonstrate that the simulation results match the calculations. From the diagram it can be seen that dynamical

Table 4.1: Root mean square error of surface temperature for different WRF PBL schemes studied

	$T2_{max}$			$T2_{min}$			$T2_{mean}$		
	$d01$	$d02$	$d03$	$d01$	$d02$	$d03$	$d01$	$d02$	$d03$
Jan 2002									
$ACM2$	1.84	2.57	1.83	3.16	1.96	2.96	2.11	1.75	2.02
YSU	1.78	2.19	1.76	3.50	1.93	3.31	2.30	1.45	2.22
MYJ	2.07	3.48	2.10	1.96	1.92	1.76	1.40	2.42	1.35
$MYNN2$	1.73	2.67	1.73	2.19	1.58	2.59	1.79	1.63	1.69
Jul 2002									
$ACM2$	2.19	2.09	2.01	1.48	1.41	1.31	0.82	1.37	0.776
YSU	2.13	2.03	1.95	2.00	1.93	1.84	0.81	1.82	0.77
MYJ	2.21	2.09	2.00	1.90	1.83	1.74	0.90	1.21	0.84
$MYNN2$	2.44	2.34	2.26	1.55	1.48	1.39	0.89	1.43	0.85

downscaling from 8 km to 2.67 km results in decreased values of NSD (i.e., simulated T2max patterns approach closer to observations). In contrast, further downscaling from 2.67 km (Figure 4.9 b) to 0.888 km (Figure 4.9 c) triggers model solution deviations away from the observations. There are several possible explanations for spatially dependent T2max variability, including that the model simulates its own dynamics due to increased spatial variability. Another possible explanation is that the uncertainty in parameterizing small-scale processes increases with increased spatial resolution. The Taylor diagram (Figure 4.10 a-c) for T2min demonstrates WRF's better forecasting skill compared to the T2max, with a higher CC (≥ 0.95) and lower RMSD than the T2max. The model showed excellent performance in simulating T2mean, as can be seen in Figure 4.11 a-c). In general, WRF showed better skill in simulating daily maximum temperatures than the other two temperatures. Very close clustering of the points indicates that the simulated T2max is less sensitive to the choice of PBL schemes. The model-simulated temperatures show very little sensitivity to dynamical downscaling in January. In January, midlatitude weather is dominated by large-scale weather conditions and prevents the model from developing its own internal dynamics.

In summary, WRF shows very high skill scores in simulating daily T2max, T2min, and T2mean temperatures with respect to DAYMET observations in the case of all three matrices of Taylor statistics. The model's ability in simulating observed temperatures indicates a higher skill score in July than in January. Overall, the intermediate domain (domain 2) and YSU scheme gave the best overall performance in simulating all three temperatures.

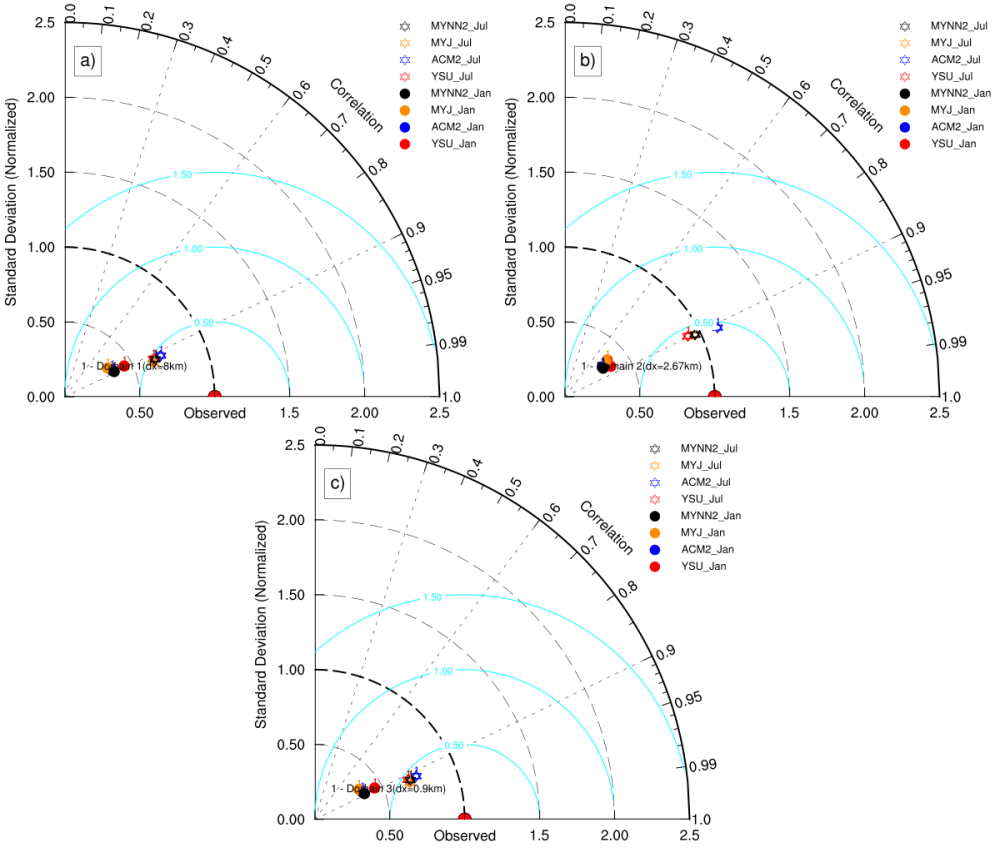

Figure 4.9: Taylor diagram showing the correlation coefficient and standard deviation of the simulated daily maximum temperatures (T2max) relative to DAYMET observations for the four PBL schemes listed in Table 2.4 for the month of January (solid circle) and July (void star) of 2002.

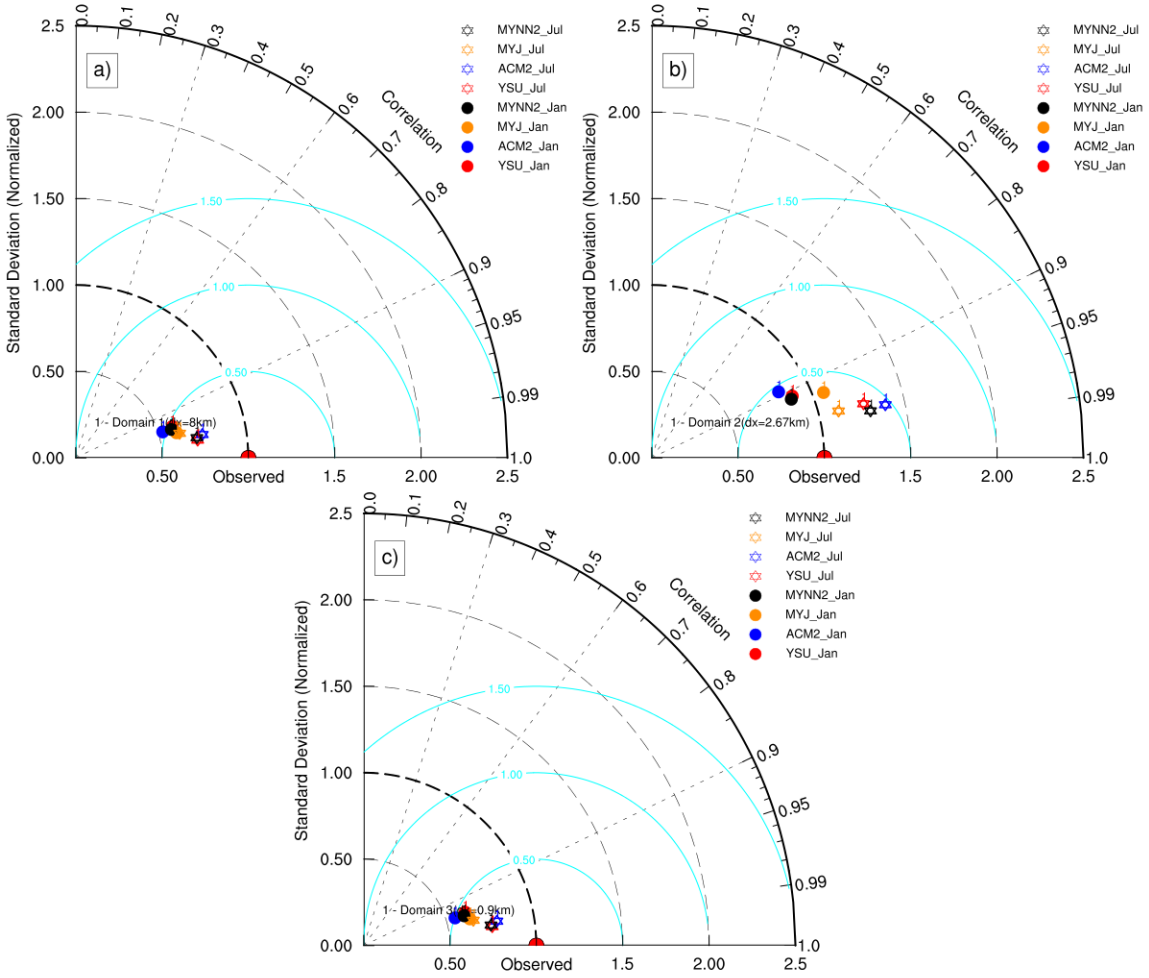

Figure 4.10: The same as Figure 4.9 but for the daily minimum temperature (T2min).

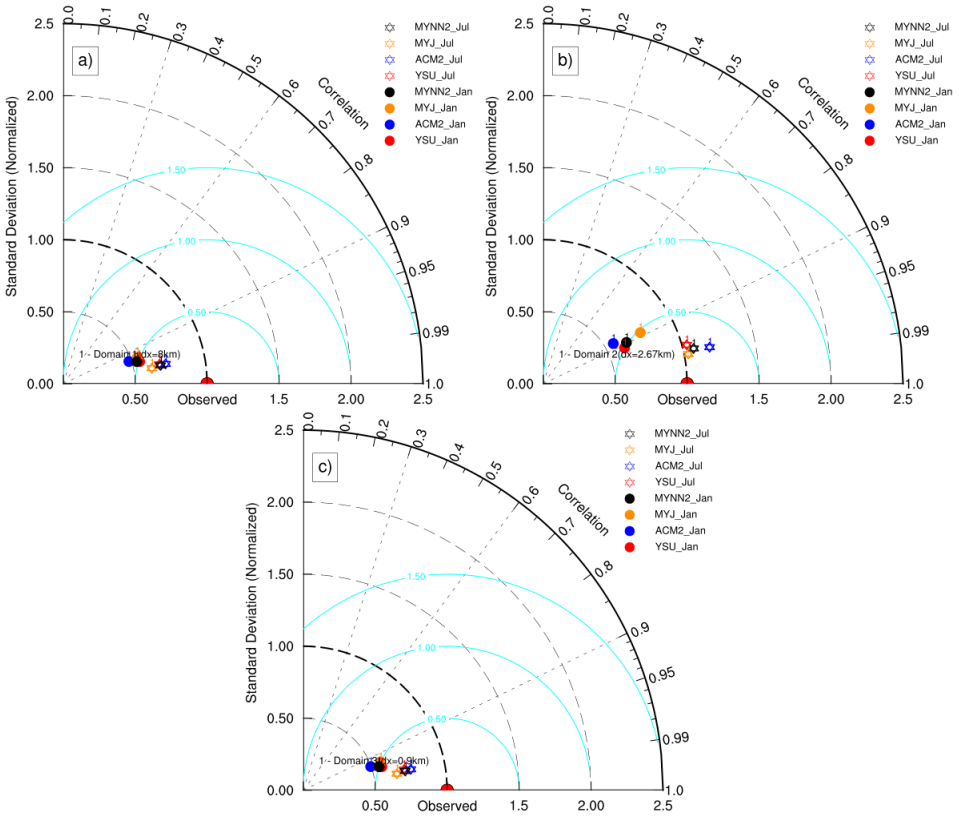

Figure 4.11: The same as Figure 4.9 but for the daily mean temperature (T2mean).

The PDFs of daily maximum (Figures 4.12) and minimum (Figures 4.13) temperatures at a two-meter height above the surface indicate that the MYJ scheme shows largest overestimation of T2max both in January and July. Although the difference among the four PBL schemes are small, the YSU gives the lowest overall underestimation. The comparison of January and July PDFs clearly show seasonal dependence of PBL scheme's performance. All PBL schemes were able to reproduce observed extreme temperatures range for both January and July. In January, simulated T2max and T2min show nearly perfect Gaussian distribution (top right and bottom right panels).

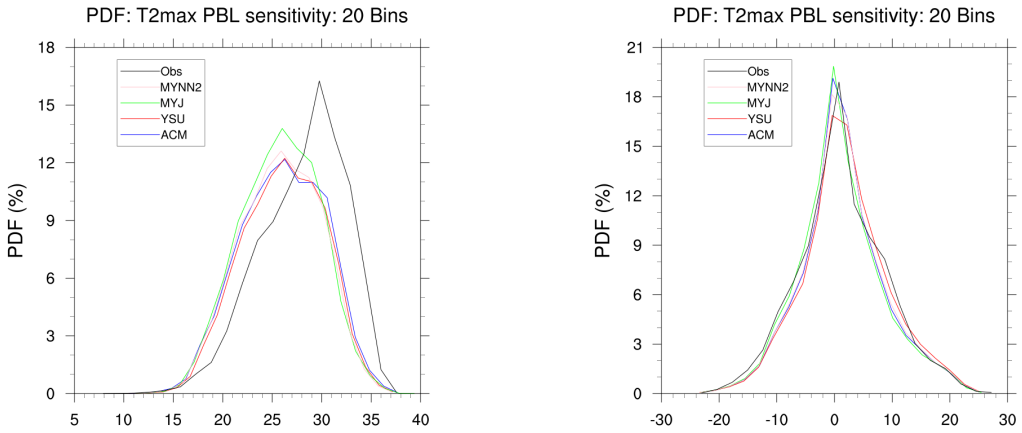

Figure 4.12: Probability density function for the daily maximum temperature (T2max) at a two-meter height above the surface for July (left) and January (right), 2002.

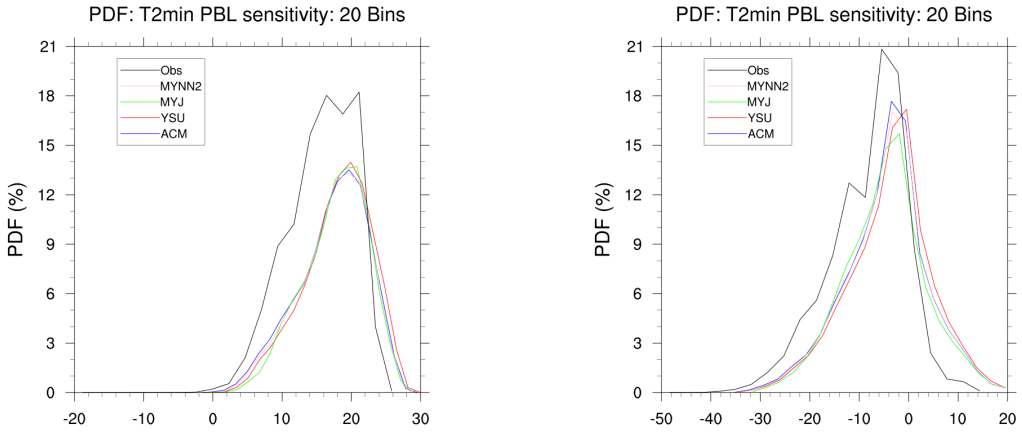

Figure 4.13: The same as Figure 4.12 but for the daily minimum temperature (T2min).

4.2.3 Sensitivity to PBL Height Evolution

Figure 4.14 illustrates the spatial distribution of WRF-simulated PBL height bias against the NCEP FNL (Final) operational global analysis data for July 28, 2002 at 0000 UTC. Visual comparison indicates that the YSU PBL scheme corresponds best with NCEP FNL analysis, followed by the MYJ scheme; whereas the MYNN2 scheme shows the highest bias among the four PBL schemes. A separate analysis shows that on July 28, 2002, at 0000 UTC, nearly all PBL schemes simulated a PBL height slightly above 300 hPa. Consider Figure 4.15, which plots the vertical profile of the simulated vertical wind component versus pressure (valid at the same day and time). At around 300 hPa height, the WRF-simulated vertical wind component shows sensitivity to PBL schemes. The YSU scheme simulated vertical wind velocity is almost double that of ACM2 and MYNN2 and matches with that of the MYJ scheme. These higher values of vertical wind velocity can explain the lower bias in WRF-simulated PBL height bias against NCEP FNL analysis. A high vertical velocity transports more heat and moisture to the upper atmosphere. Of the four PBL schemes, the MYNN2 scheme gives the highest bias both on July 28 and July 23 (figure not shown). This study observed that during the night, the YSU PBL scheme, a non-local closure-based PBL scheme, does a better job than the rest.

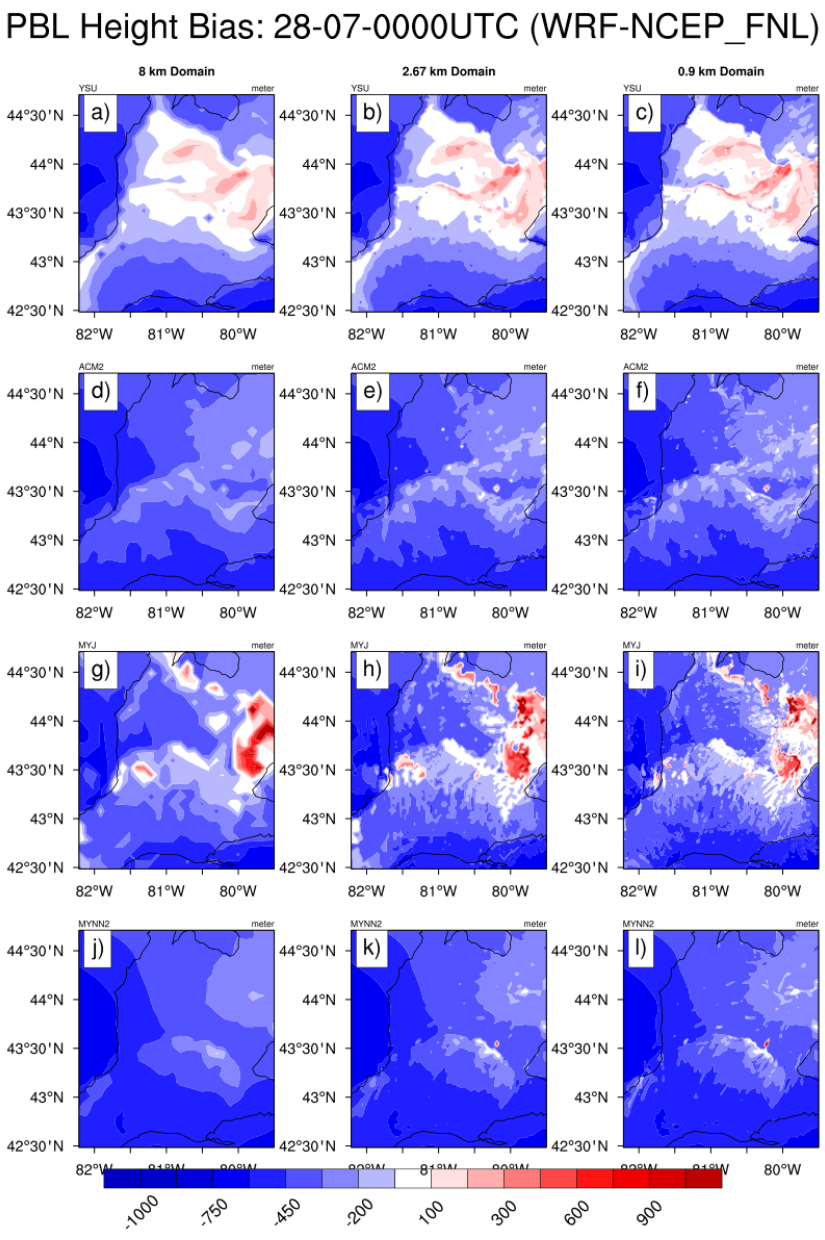

Figure 4.14: The spatial distribution of planetary boundary layer height bias (WRF-NCEP-FNL) valid at 0000 hr July 28, 2002.

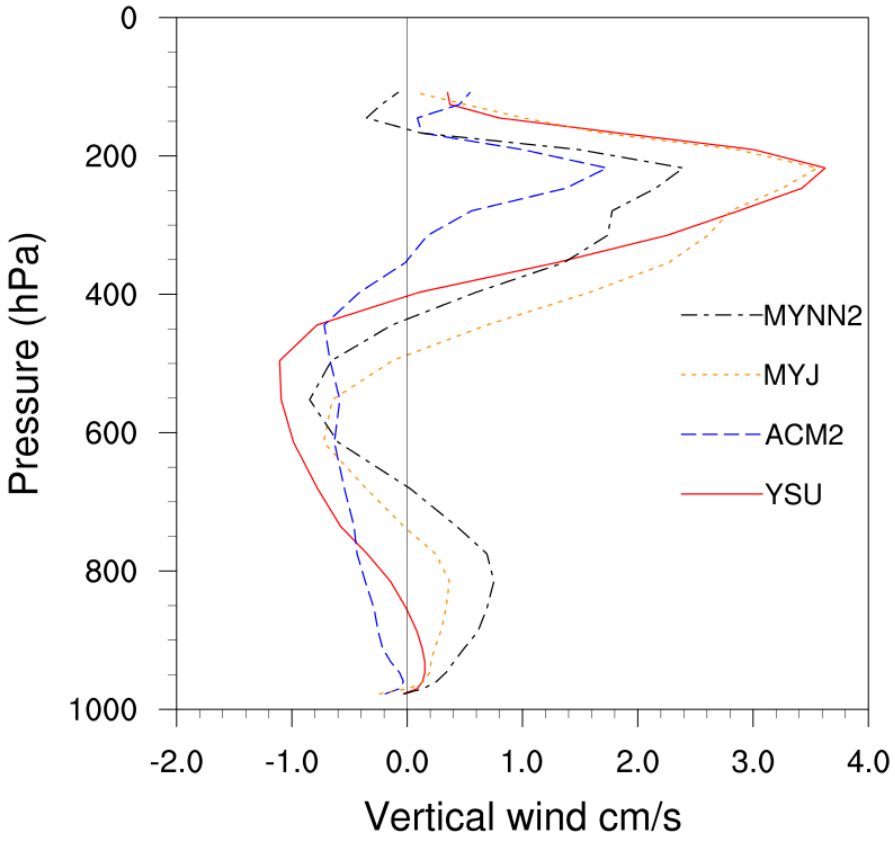

Figure 4.15: Vertical profile of domain-averaged simulated vertical wind component for the four PBL schemes valid at 0000 hr July 28, 2002.

4.2.4 Thermodynamic Characteristics Analysis

Figure 4.16 compares the simulated and observed skew temperature and dew point profiles and the simulated vertical wind profile at Buffalo and Albany, New York, at 0000 UTC 23 Jul 2002. Below 850 hPa all four PBL schemes show nearly similar dew point profile structures. This agreement can be explained by the simulated vertical wind profile of the corresponding PBLs. Likewise, one can also explain the simulated dew point profile difference in the middle atmosphere. Overall, the YSU-scheme-simulated dew point profile shows closer agreement with the observed radiosonde profile. It is observed from the vertical wind profile that the MYJ-simulated wind is approximately 5 cm/s higher than that of the other three PBLs, from 400 to 200 hPa. The simulated dew point profile exhibits the same kind of behavior. Further, in July 10 at 0000 UTC, the YSU simulated skew-T profile outperforms the other schemes (Figure 4.17). During the night, the MYJ scheme gives a moist low-level atmospheric profile. The excessive low level moisture generates spurious precipitation when mesoscale convective (MCS) passes over it or energizes the air parcel to overcome capping inversion, thereby triggering convection.

Any biases in simulated low level circulation affect water vapor transport, which in turn generates erroneous precipitation. Brown (1996b) [14] and Brown *et al.* (2006) [15] found too weak model-simulated wind compared to 850 hPa radiosonde observations and attributed the wind bias to faulty mixing in the convective boundary layer. Inadequate vertical mixing deliver less surface-water-vapor to higher layers and may result in dry bias (wet bias) in the vertical profile of specific humidity at the upper part (lower part) of the ABL. In addition, during the, poor vertical mixing moves less heat from the surface to upper levels. A common characteristic of non-local schemes is that they are capable to transport adequate amounts of moisture apart from the surface and deposit at higher model levels.

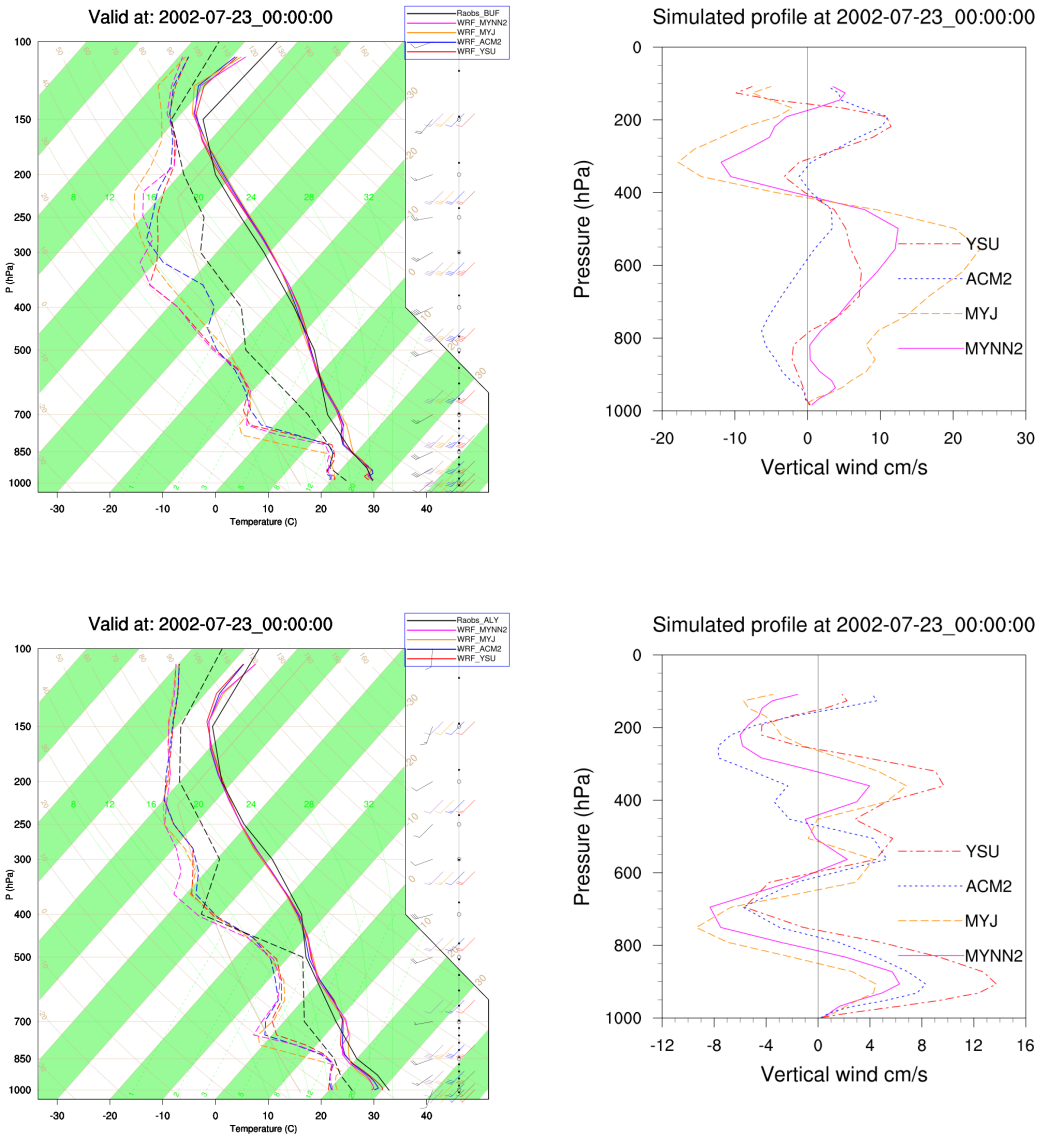

Figure 4.16: Simulated vs observed Skew-T and vertical wind (W) profiles at Buffalo (top row) and Albany (bottom row), New York, valid at 0000 hr of Jul 23, 2002.

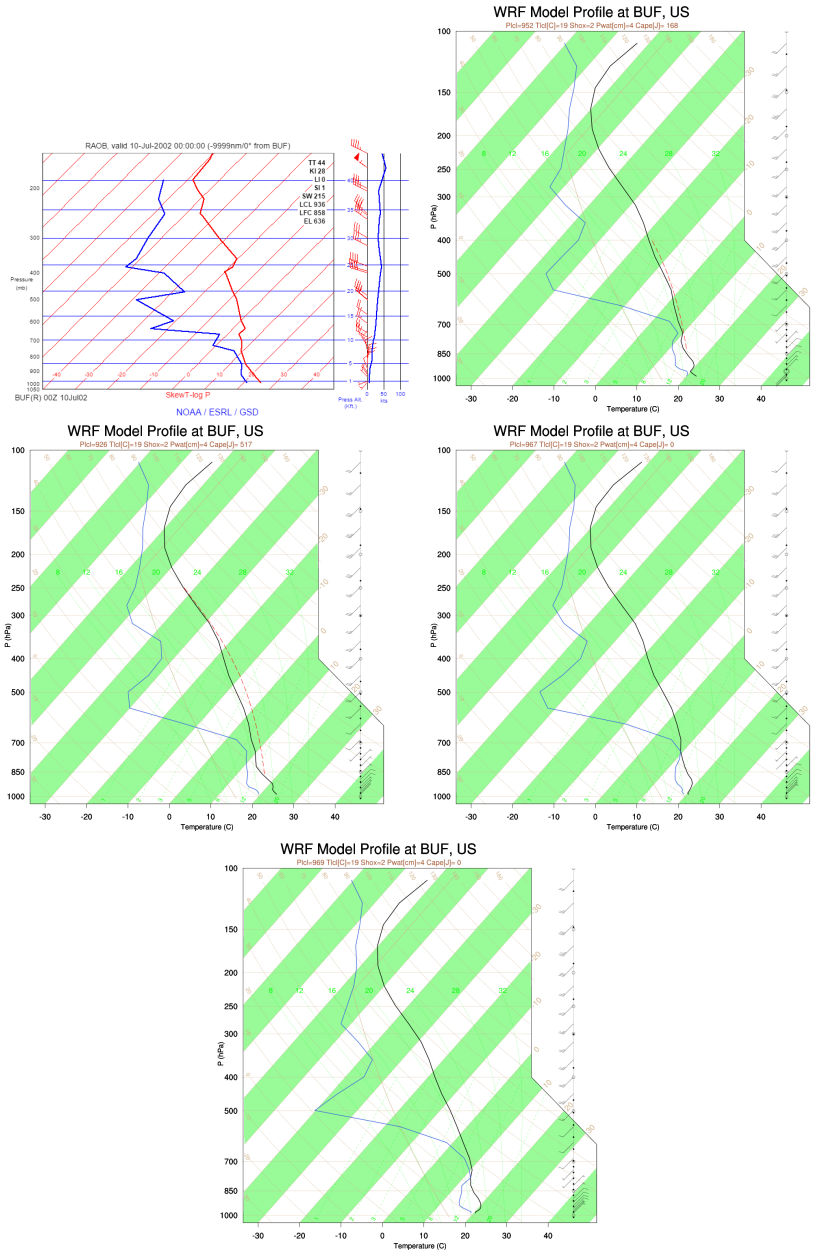

Figure 4.17: Skew-T profiles: ROAB (top row, left column), YSU ((top row, right column), ACM2 (middle row, left column), MYNN2 (middle row, right column), and MYJ (bottom row)) valid at 0000 hr of July 10, 2002.

Table 4.2 presents a quantitative comparison of observed lifting condensation level (LCL) height in mb (hPa) at different sounding locations (Albany, NY (ALB), Buffalo, NY (BUF), Pittsburgh, PA (PIT), Gaylord, MI (APX), and Petawa, ON-CN (YWA)) and corresponding WRF-simulated values for the different PBL schemes. The WRF simulations at 0000 UTC and 1200 UTC for July 10 and 23, 2002 were also validated. The different PBL schemes give different LCL heights at the same location. It is evident from vertical wind profiles that PBL scheme's ability in simulating thermodynamic structures of the atmosphere largely depend on accurate representation of vertical wind component as observed in skew-T analysis.

Table 4.2: Model simulated and observed lifting condensation level (LCL) height in mb (hPa)

	Valid at 00 UTC					Valid at 12 UTC				
	ALB	*APX*	*BUF*	*PIT*	*YWA*	*ALB*	*APX*	*BUF*	*PIT*	*YWA*
Jul 10, 2002										
OBS	975	000	936	942	886	958	000	916	959	902
YSU	874	000	952	935	850	906	000	898	933	906
ACM2	962	000	926	916	867	922	000	896	951	918
MYJ	911	000	969	949	876	937	000	924	949	925
MYNN2	902	000	967	934	859	916	000	913	925	917
Jul 23, 2002										
OBS	904	850	904	865	967	952	876	000	933	963
YSU	864	851	896	832	894	933	851	872	948	938
ACM2	891	851	874	856	916	945	942	869	956	943
MYJ	910	887	891	892	945	971	954	904	970	947
MYNN2	896	865	877	842	911	930	865	874	959	939

4.3 Discussion and conclusions

In the NWP model, PBL parameterization is important in simulating near-surface atmospheric conditions, which are then fed back to other components of the model solver. Simulation errors can propagate to other model components, and over time, amplify and significantly deteriorate a model's forecasting skill due to the stochastic nature (butterfly effect) of the atmosphere.

The WRF simulations for January that used non-local closure-based PBL schemes not only produce slightly higher precipitation along the Great Lakes shores but also diffuse precipitation bias far inland compared to simulations that used local closure-based assumptions. Corresponding PBL schemes give similar LHF bias patterns along the shores in January, perhaps because excessive moisture and latent heat in the lower to middle atmosphere produce excessive cloud cover, which eventually produces spurious non-convective precipitation with the microphysics scheme.

In July, all PBL schemes show a systematic wet and dry bias over the north-western corner of southern Ontario and the Grand River watershed, respectively, although the local closure-based MYJ scheme produces the lowest bias over the first area. Earlier studies found that local closure-based PBL schemes transport less moisture downwind, which may explain the lower precipitation bias over the north-western corner of southern Ontario, a peninsular-like area in Lake Huron. The dry bias over the Grand River watershed is probably due to erroneous initial soil moisture, temperature, and texture conditions. ACM2 gives the wettest bias in July of the four PBL schemes, and overall, MYJ gives a lower precipitation-distribution bias. In addition, the relatively higher bias in the spatial distribution of precipitation along the three Great Lakes shores of southern Ontario in January and the north-western corner of southern Ontario in July indicates the limited capability of PBL schemes to represent boundary layer processes.

In addition to time-series and spatial-pattern analyses, PDFs of the total-precipitation for the PBL schemes further confirm that precipitation is less (more) sensitive to PBL parameterization in January (July). As shown by the PDFs of July precipitation, all PBL schemes except MYJ can replicate high frequency but lower-precipitation events very well. In general, the PBL schemes strongly disagree with one another in the case of low-frequency but intense total precipitation amount events. Although simulated January precipitation shows lower sensitivity to PBL parameterization, the YSU scheme is somewhat better at reproducing observed low-frequency extreme-precipitation events.

Our study has demonstrated that the local and non-local PBL schemes differ in their capabilities to transfer moisture to upper model levels, resulting in differences in condensate

and associated latent heating profiles, and ultimately in precipitation totals, rates, and intensities. Our results agree with those of earlier sensitivity studies (Efstathiou *et al.*, 2013 [22]; Krogsaeter and Reuder, 2015 [50]; Ruiz *et al.*, 2010 [88]; Borge *et al.*, 2008 [10]), who reported similar kinds of persistent vertical mixing biases for local and non-local closure based PBL schemes.

The Skew-T analysis for January shows that the ABL is relatively cold and dry, resulting in a stable atmosphere with shallow PBL. In contrast, in July, the PBL scheme helps stabilize the atmosphere, by transporting various surface fluxes from the lowest couple of meters of the Earth's surface to the upper atmosphere. The PBL scheme directly influences summer precipitation by transporting necessary energy up to the LCL to initiate convection. The MYJ scheme shows persistent weakness in carrying heat and moisture from the Earth's surface to entrain warmer and drier air into the PBL, resulting a colder PBL. A warmer PBL in late afternoon with the YSU and ACM2 schemes results from excessive upward mixing. At night, in the lower atmosphere, the WRF model with the YSU PBL scheme produces higher temperatures and less moisture than with the other three schemes because of its heavier mixing capability. Lower night-time PBL height bias can be explained by the higher vertical wind velocity simulated by the YSU scheme. The PBL schemes also show spatial and temporal variabilities in simulating LCL heights. It is possible to conclude that a PBL scheme's ability to accurately simulate vertical wind components is key to correctly simulating thermodynamic structures of the atmosphere. The PBL systematic errors depend on time of day and also on large-scale atmospheric conditions. The findings of the present study agree well with the findings of García-Díez *et al.* (2013) [29], who investigated WRF model's PBL sensitivity over Europe.

The YSU and MYJ schemes give the best and worst performance in reproducing observed temperature distributions, respectively and reaffirm the inherent advantage and disadvantages of non-local and local closure-based PBL schemes. In general, WRF showed better skill in simulating daily maximum temperatures than the other two temperatures. The model's ability in simulating observed temperatures indicates a higher skill score in July than in January. In January, mid-latitude weather is dominated by large-scale weather conditions and prevents the model from developing its own internal dynamics. Dynamical downscaling beyond a threshold horizontal resolution leads WRF-simulated temperatures to deviate from the observations. The most-probable explanation is that the model simulates its own dynamics due to increased spatial variability. Another possible explanation is that the uncertainty in parameterizing small-scale processes increases with increased spatial resolution.

The evaluation matrices discussed above indicate that among the four PBL schemes studied, YSU gives more robust results over southern Ontario. Overall, the YSU PBL

parameterization scheme outperformed the others over southern Ontario. Our study has demonstrated that despite major efforts to design an appropriate PBL scheme that represents surface atmospheric conditions, success is still limited. The present research supports previous findings and contributes to existing knowledge of PBL parameterization's role in NWP models.

The study findings have a number of important immediate implications for the following activities:

- Better prediction of pollutant dispersion.
- Accurate forecasting of fog, which is a very important meteorological phenomenon for transportation safety, especially in the field of aviation meteorology.
- Commercial applications, such as offshore wind energy potential assessment along the Great Lakes shores.
- Accurate prediction of boundary layer height, which will help clarify urban heat island effects, which in turn will improve the forecasting of current and future energy demand.

Chapter 5

Performance Study of Four Cloud Microphysics Schemes in the WRF Model

5.1 Introduction

Microphysics (MP), an important physical parameterization scheme, is as important as convective parameterization. In an NWP model, a MP parameterization scheme is used to simulate the evolution of various forms of hydrometeor species (e.g., cloud water, cloud ice, water vapor, rain, snow and graupel/hail), their interactions, growth, and precipitation at each model grid point. The complexity of MP schemes significantly influences the evolution of surface precipitation. This study investigates the performance of five MP schemes with complexities across the spectrum in reproducing observed precipitation and temperature variabilities. The goal is to identify an MP parameterization scheme that provides the overall best performance over southern Ontario. Section 5.2 briefly introduces fundamentals of cloud microphysics parameterization followed by an introduction of various hydrometeor properties in Section 5.3. The key characteristics of the five MP schemes are summarized in Section 5.4. The data and methodology are already discussed in Chapter 2. Section 5.5 gives results and discussion, and section 5.6 summarizes the main conclusion of this chapter.

5.2 Fundamentals of Cloud Microphysics Parameterization

In a broader sense, microphysics parameterization schemes can be divided into: Bulk and Bin (spectral) schemes. The Bulk MP schemes first assume an underlying shape (e.g., gamma, exponential) for a particular hydrometeor size distribution, and then predicts one or more bulk quantities (e.g., mixing ratio, number concentration) for the distribution (Morrison *et al.*, 2009 [70]). On the other hand, Bin MP schemes divide microphysical particles into bins according to their different sizes, and explicitly predict the evolution of each particle size distribution (Figure 5.1).

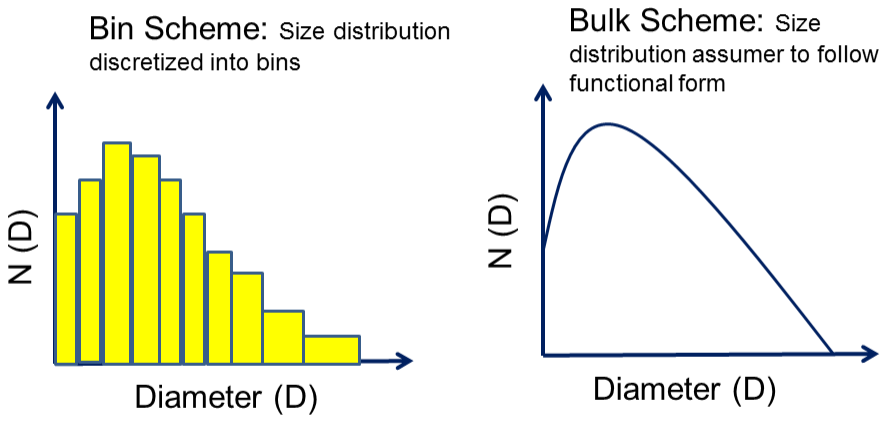

Figure 5.1: Example of assumed shape distribution for the size (mass) distributions of various hydrometeors.

Most Bulk MP schemes (Lin, 1983 [56]; Milbrandt and Yau, 2005 [62]; Hong and Lim, 2006 [37]) use a three-parameter (intercept, shape and slope) gamma distribution function to describe the size spectra of each precipitating hydrometeor category and can be computed using the following equation:

$$N(D) = N_0 D^{\alpha} e^{-\lambda D} \tag{5.1}$$

where N_0, α, and λ represent the intercept, shape, and slope parameters, respectively. When $\alpha = 0$, equation (5.1) takes the form of an inverse-exponential distribution.

The Bulk MP scheme is characterized by the number of moments (M_n) a scheme uses to predict the particle size distribution of each hydrometeor species within a grid volume [67]. The equation that describes the n^{th} moment of a size distribution can be written as

$$M_n = \int_0^{\infty} \mathrm{D}^n \, N(D) \, \mathrm{d}D \tag{5.2}$$

where M_n represents the moment of a size distribution, n is the moment order, and N is the number concentration of particles in a given hydrometeor class with diameter D. The higher the number of predicted moments an MP scheme uses, the larger the degrees of freedom it will have to characterize particle size (mass) distribution (Morrison *et al.*, 2009 [70]; Milbrandt and Yau, 2005 [62, 63]). A multi-moment MP scheme can predict the size (mass), shape and number concentration of each prognostic hydrometeor species more independently than a single-moment scheme.

The single-moment CMPs predict only the mass mixing ratios of the hydrometeor species, whereas the two-moment (double moment) schemes predict not only the mass mixing ratios but also the number concentration of the hydrometeor species. The MP moment is defined mathematically by the following equation (5.3):

$$r = \frac{\pi}{6} \times \rho_{water} \times N \times D^3 \tag{5.3}$$

where r represents the mixing ratio, ρ_{water} is the density of water, and N and D are as stated above in equation (5.2). Although a particular type of bulk MP scheme (e.g., single or double moment) uses the same number of prognostic hydrometeor species and the same number of predicted moments, individual schemes can differ significantly. In particular, different numbers of microphysical processes contribute to the sources and sinks of each hydrometeor class. Even if the number of microphysical processes is the same, they can have a different order of execution.

A recent study by Molthan and Colle (2012) [67] documented that MP schemes can also differ in their assumed shape of particle size distributions, and the functional relationship among particle mass, diameter and terminal-fall speed.

5.3 Properties of Hydrometeors

The parameterization schemes (Table 2.5) studied in this experiment contain a maximum of six classes of hydrometeors: cloud water, cloud ice, water vapor, rain, snow, and graupel/hail. Rain, snow, graupel, and hail particles possess large size (mass) distributions compared to cloud water and cloud ice, and gravitational force results in their significant fall velocity. Ice particles with higher fall velocity (snow, graupel, and hail) are called precipitating, whereas low-velocity cloud ice is termed non-precipitating.

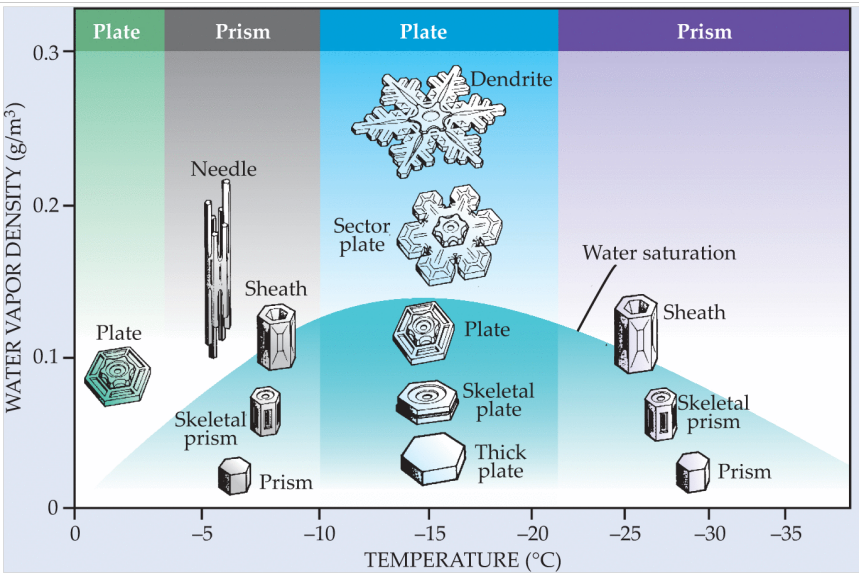

Figure 5.2: snow crystal growth behavior in cloud with temperature and humidity. From Furukawa, Yoshinori, and John S. Wettlaufer (2007). The Y axis of the diagram represents the density of water vapor in excess of saturation with respect to ice.

5.3.1 Snow

The American Meteorological Society's Glossary of Meteorology defines snow as *"Precipitation composed of white or translucent ice crystals, chiefly in complex branch hexagonal form and often agglomerated into snowflakes."* Japanese physicist Ukichiro Nakaya extensively studied snow characteristics in his lab (having taken more than 3,000 microphotographs) and proposed a snow crystal morphology diagram that is widely accepted in the scientific community and has became known as the Nakaya Diagram (Figure 5.2). It illustrates

the snow crystal growth behavior in clouds with changes in temperature and humidity (adapted from Furukawa and Wettlaufer, 2007 [28]).

Kenneth G. Libbrecht, a physics professor at the California Institute of Technology (Caltech) constructed a resource-dense website describing the art and science behind the beautiful shapes of snow crystals:http://www.snowcrystals.com/science/science.html .

5.3.2 Ice

When a parcel of unstable air ascends, its temperature starts decreasing, and its water vapor starts to condense and form clouds. If the cloud water continues to ascend, at some point its temperature drops below 0 °C. The water droplets with temperature below 0 °C are known as supercooled water. In the absence of cloud condensation nuclei (CCN), water needs to be cooled down to below −40 °C to become frozen. This kind of freezing is called homogeneous freezing. The real atmosphere is full of aerosol particle and acts as CCN. Hence, the water droplets freeze at just a few degrees below zero.

Figure 5.3: Hail is a form of frozen precipitation that forms when rain is forced above the freezing level by a thunderstorm's updraft and takes the form of irregular lumps of ice or balls.[Figure courtesy of NOAA National Severe Storms Laboratory]

5.3.3 Hail

In the Glossary of Meteorology, hail is defined as *"precipitation in the form of balls or irregular lumps of ice"*. An ice crystal starts to fall under the influence of gravity once it grows to a critical size and mass. Along its way, it collides with other ice crystals and

supercooled water (liquid water with temperature below 273 K) droplets. If the collisions are predominantly with ice crystals, it takes the form of snowflakes. If the collisions are with supercooled water droplets, it takes the form of graupel or hail.

5.4 Characteristics of the selected Microphysics Schemes

All five MP schemes selected for sensitivity testing over the Great Lakes basin belong to the bulk MP parameterization (BMP) class: the WRF single moment six class (WSM6) scheme of Hong and Lim, 2006 [37]; ETA grid-scale cloud and precipitation scheme (sometime known as Eta-Ferrier scheme) of Rogers *et al.* (2001) [87]; Purdue university's Lin (PLIN) scheme of Lin *et al.* (1983) [56]; Thompson (THOM) scheme of Thompson *et al.* (2008) [97]; Morrison two moment (M2M) scheme of Morrison *et al.* (2009) [70]. The prognostic water substance variables that all CMPs, except ETA, predict include the mixing ratios of water vapor (q_v), cloud water (q_c), cloud ice (q_i), snow (q_s), rain (q_r), and graupel (q_g). The ETA scheme excludes graupel and ice. The M2M scheme also predicts the mixing ratio of hail (q_v).

The primary difference between PLIN and WSM6 schemes lies in their treatment of ice-phase microphysical processes (Table 5.1). The WSM6 scheme, unlike the others, computes the sedimentation of falling hydrometeors before the microphysical processes. Hong and Lim (2006) [37] calculated the mass wighted terminal velocity V_G for graupel according to equation (5.4).

$$V_G(ms^{-1}) = \frac{a_G \Gamma(4 + b_G)}{6} \sqrt{\frac{\rho_0}{\rho}} \frac{1}{\lambda_G^{b_G}} \tag{5.4}$$

where a_G and b_G are the empirical coefficients for terminal velocity, λ_G is the slope parameter, ρ is the density of air, and ρ_0 is the density of air at reference state. The PLIN scheme uses the same formula, but with different values for the coefficients, a_G and b_G (Table 5.1).

The THOM scheme assumes a gamma distribution function to illustrate the particle size distribution for all hydrometeor types except snow, and predicts cloud ice mixing ratio and number concentration explicitly. Most bulk MP schemes assume snow to be a spherical particle with constant density. However, in the THOM scheme, it is considered to be non-spherical particles with variable density. In contrast to the other schemes, THOM represents snow size distribution as a function of both ice water content and temperature, and progonostically calculates total ice and rain number concentrations in addition to their

Table 5.1: Major differences between WSM6 and PLIN MP parameterization schemes. From Hong *et al.* (2009). [39]

Properties	WSM6	PLIN
Ice number concentration, N_I (m^{-3})	$5.38X10^7$ $(\rho q_I)^{0.75}$	$10^{-2}exp[0.5(T_0 - T)]$
Ice nuclei number, N_{10} (m^{-3})	$10^3exp[0.1(T_0 - T)]$	$10^{-2}exp[0.5(T_0 - T)]$
Snow intercept parameter, N_{0s} (m^{-4})	$2X10^6exp[0.12(T_0 - T)]$	$3X10^6$
Density of graupel, ρ_G (kgm^{-3})	500	400
Constant a_G	330	82.5
Constant b_G	0.8	0.5
Constant a_s	11.72	4.836
Constant b_s	0.41	0.25

mixing ratios. Doing so increases the model's capability to represent some microphysical processes more realistically, for example, sedimentation. Its more-realistic representation of the number of ice nuclei helps the model accurately forecast formations of cloud ice and mixed-phase hydrometeors such as snow and graupel. Of course, the accuracy comes at the cost of increased model integration time. The THOM scheme is often called a hybrid scheme, as it tries to incorporate the computational efficiency advantage of a one-moment scheme with the greater precision of a two-moment scheme (Otkin and Greenwald, 2008 [75]). This scheme was originally designed to simulate drizzle conditions for aviation management.

Among the five MP schemes tested, the M2M scheme not only uses a prognostic equation to predict the mixing ratios of the hydrometeors but also predicts number concentrations for four hydrometeor species (water droplets, cloud ice, rain, and snow). It also uses new physically based parameterizations that represent homogeneous and non-homogeneous ice nucleation separately.

5.5 Results and Discussion

5.5.1 Precipitation

Temporal Precipitation Patterns

Figure 5.4 compares the diurnal variation of simulated total precipitation (convective + grid-scale) using five MP schemes against DAYMET-gridded observations for January (top plot) and July (bottom plot). Model performances were mixed for simulated precipitation. For example, a certain scheme was able to reproduce the magnitude and phase in one precipitation event but showed poor performance in another. All MP schemes showed good performance while simulating heavy precipitation events. Meanwhile, a number of times, the simulated precipitation phase lagged behind the observations. In fact, the model delayed starting some precipitation events in January.

One can clearly see from the January time series that the PLIN scheme usually produced the highest total precipitation of the five MP schemes. Accordingly, the PLIN scheme produces the most accumulated precipitation (Figure 5.5). The same scheme also gave the highest total precipitation over the Colorado headwaters region, as reported by Liu *et al.* (2011) [57], who also investigated the sensitivity of five different MP schemes for wintertime precipitation. Overall, the WSM6 and PLIN gave nearly the same precipitation totals and showed higher reproducibility than DAYMET observations. January 2014 was observed to be the coldest month in a decade, temporal evolution of the WRF-simulated surface precipitation showed low sensitivity to the choice of MP schemes (Figure not shown).

The July time series showed all MP schemes to have nearly equal skill in capturing precipitation phases (Figure 5.4). On the other hand, precipitation magnitude varies from scheme to scheme. In contrast to January, the MP schemes for July show different precipitation maxima in different precipitation events, although the PLIN scheme produces an unusually high total precipitation in one event. Unlike in January, the simulated precipitation amount in July shows lower variability than observed precipitation. In fact, the WSM6 scheme exactly replicates the observed precipitation total, although other schemes show low bias as well.

In summary, this study finds that the simulated total precipitation bias for July is less than that for January. The WSM6 scheme shows better skill in simulating surface precipitation. The performance of MP schemes shows a strong dependence on annual climatological conditions. Moreover, the Great Lakes ice cover statistics influence the performance of MP schemes (as detailed in Chapter 6).

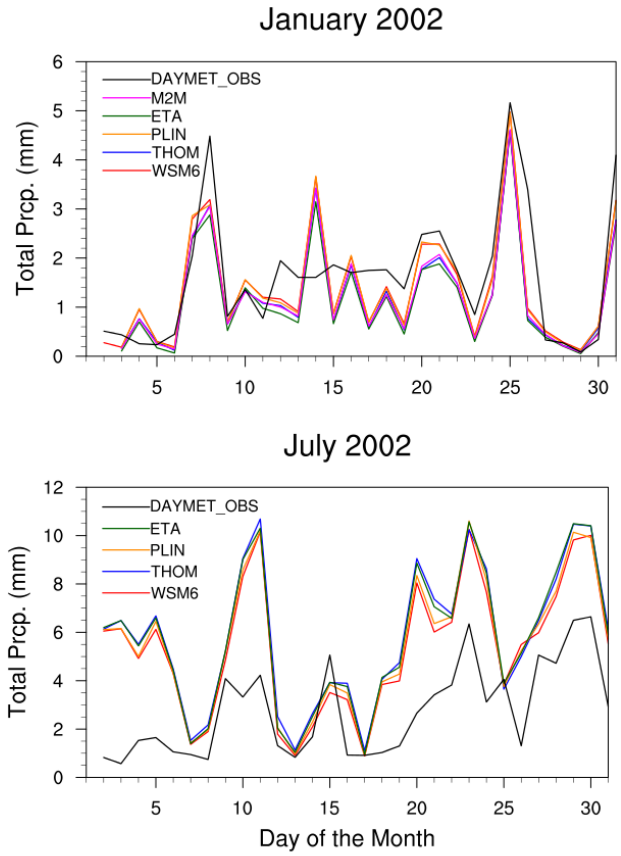

Figure 5.4: Domain averaged daily time series of the DAYMET observation (black) and WRF-simulated total precipitation (RAINC + RAINNC) by five microphysics schemes: WSM6 (red), THOM (blue), PLIN (dark orange), ETA (green), and M2M (magenta) from innermost domain equivalent areas of the outermost domain (domain 1).

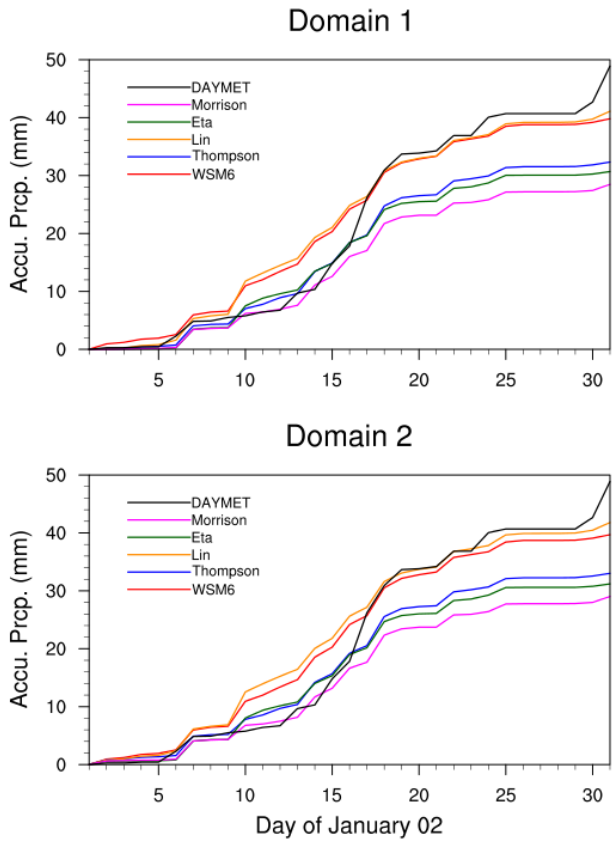

Figure 5.5: Temporal evolution of spatially and temporally averaged WRF-simulated accumulated total precipitation (mm) using five different MP schemes (WSM6(red), Thhompson(blue), Lin(yellow), Eta(green), and Morrison (magenta)) and DAYMET observations (black) from (a) Domain 1 (top panel) (b) Domain 2 (bottom panel) for January 2002. Spatially and temporally averaged accumulated total precipitation.

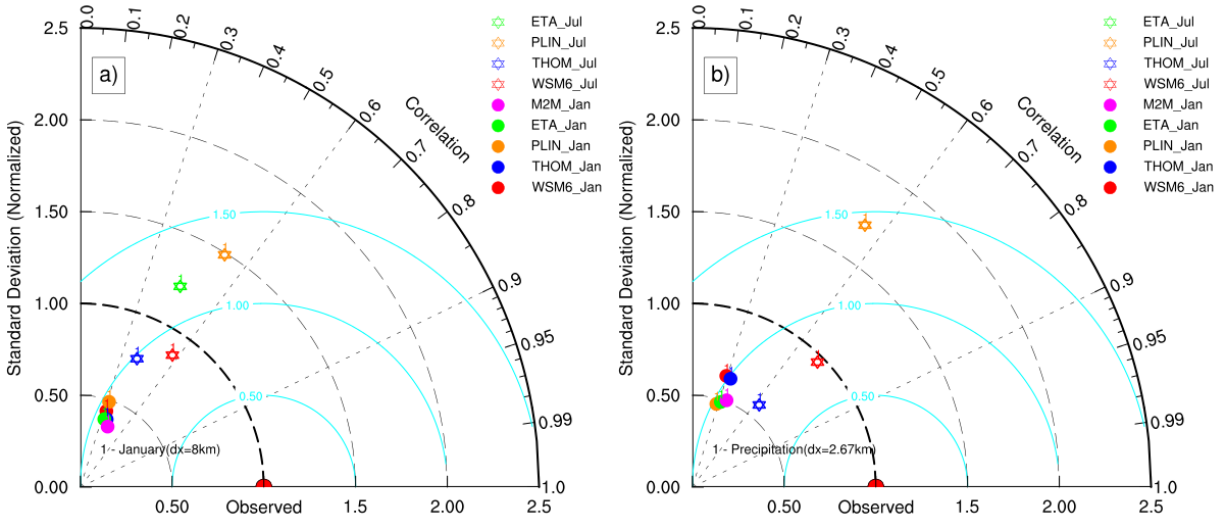

Figure 5.6: Taylor diagram showing correlation coefficient, normalized standard deviation and root mean squared difference of daily total precipitation relative to DAYMET observations for five MP schemes listed in Table 2.5 for January (solid circle) and July (void star) of 2002.

Box plots (Figure 5.7) represent the median, minimum/maximum value, and the 25th/75th percentiles of the WRF-simulated and DAYMET-observed daily total precipitation. The plots allow quick visualization of the seasonal dependence of MP-scheme sensitivity. The simulated precipitation again shows more sensitivity to MP schemes in January when most precipitation falls as snow, than in July, when it falls as rain.

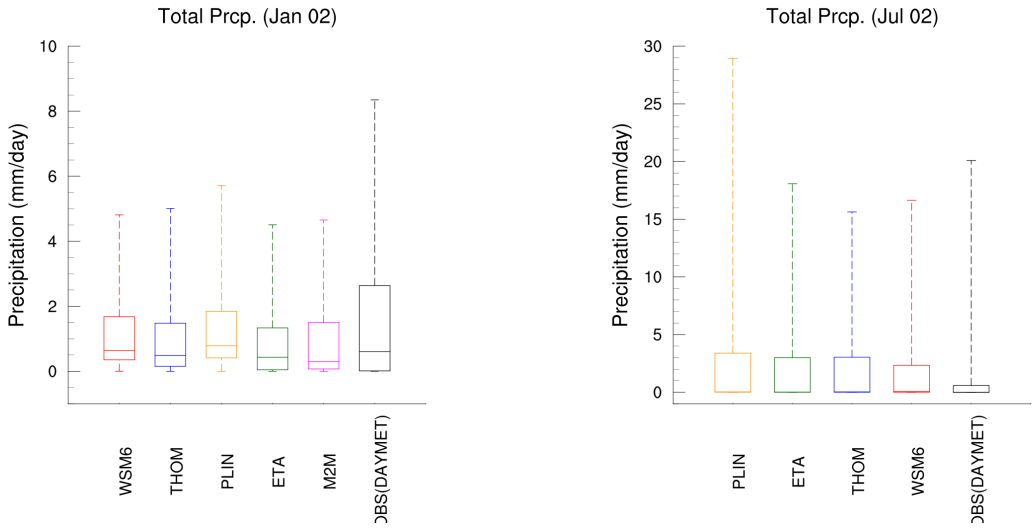

Figure 5.7: Boxplots showing distributions of daily precipitation using various cloud MP schemes: (a) January (left panel) (b) July (right panel). The top and bottom of the boxes represent 25th and 75th percentiles of the distributions, respectively. The lower and upper end of the Whisker represent the minimum and maximum value of precipitation, respectively.

As reported by Gilmore *et al.* (2015) [30], RCMs can show very little to no sensitivity to the choice of physical parameterization scheme in the case of average statistics on an extreme event such as total precipitation. However, hourly precipitation reveals dependency on the choice of physical scheme. Therefore, the probability density function (PDF) analysis done on model-simulated precipitation examined each MP scheme's skill in capturing precipitation frequency and magnitude.

Figure 5.8 shows the probability density functions (PDFs) of total precipitation using the five schemes and corresponding DAYMET observations. The PDF analysis confirms that the WSM6 scheme captures high frequency/low precipitation events very well. The

PLIN scheme follows the WSM6 scheme in capturing low frequency events. Evidently, WSM6 and PLIN perform equally while capturing low frequency extreme events. Among the schemes tested, ETA gives a low skill score in terms of PDFs and also showed the highest root mean squared error (RMSE), normalized standard deviation (NSD), and pattern correlation coefficient (CC) in Taylor diagram analysis (Figure 5.6).

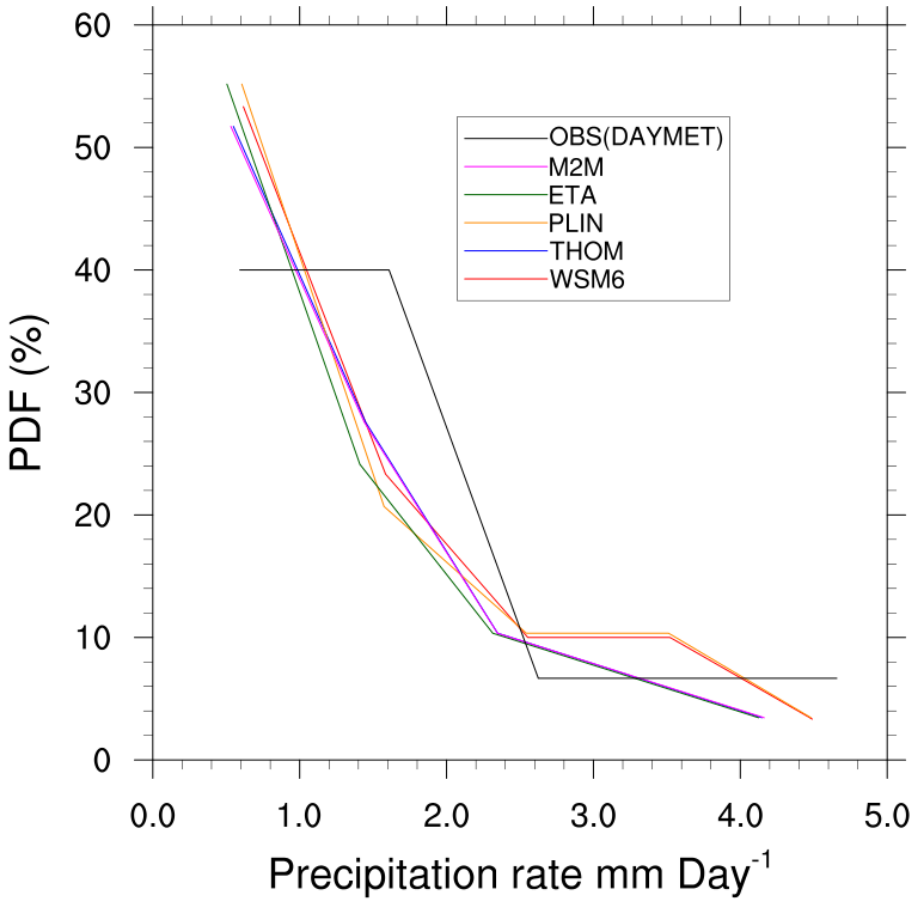

Figure 5.8: Probability density function of total precipitation for January 2002.

Spatial Precipitation Patterns

The spatial distribution of monthly total precipitation (convective + grid-scale) bias for January is shown in Figure 5.9. All schemes perform almost equally, except that the ETA scheme gives a slightly better precipitation distribution. The ETA and THOM schemes, the most simple and the second-most-complex MP schemes among the five tested, show comparatively lower bias at the interfaces between land and the Great Lakes. In July, no single scheme is obviously the best (Figure 5.10). However, when looking at the Taylor statistics of precipitation (Figure 5.6), one finds that the WSM6 scheme outperforms the other three in all three metrics (CC, SD, and RMSD).

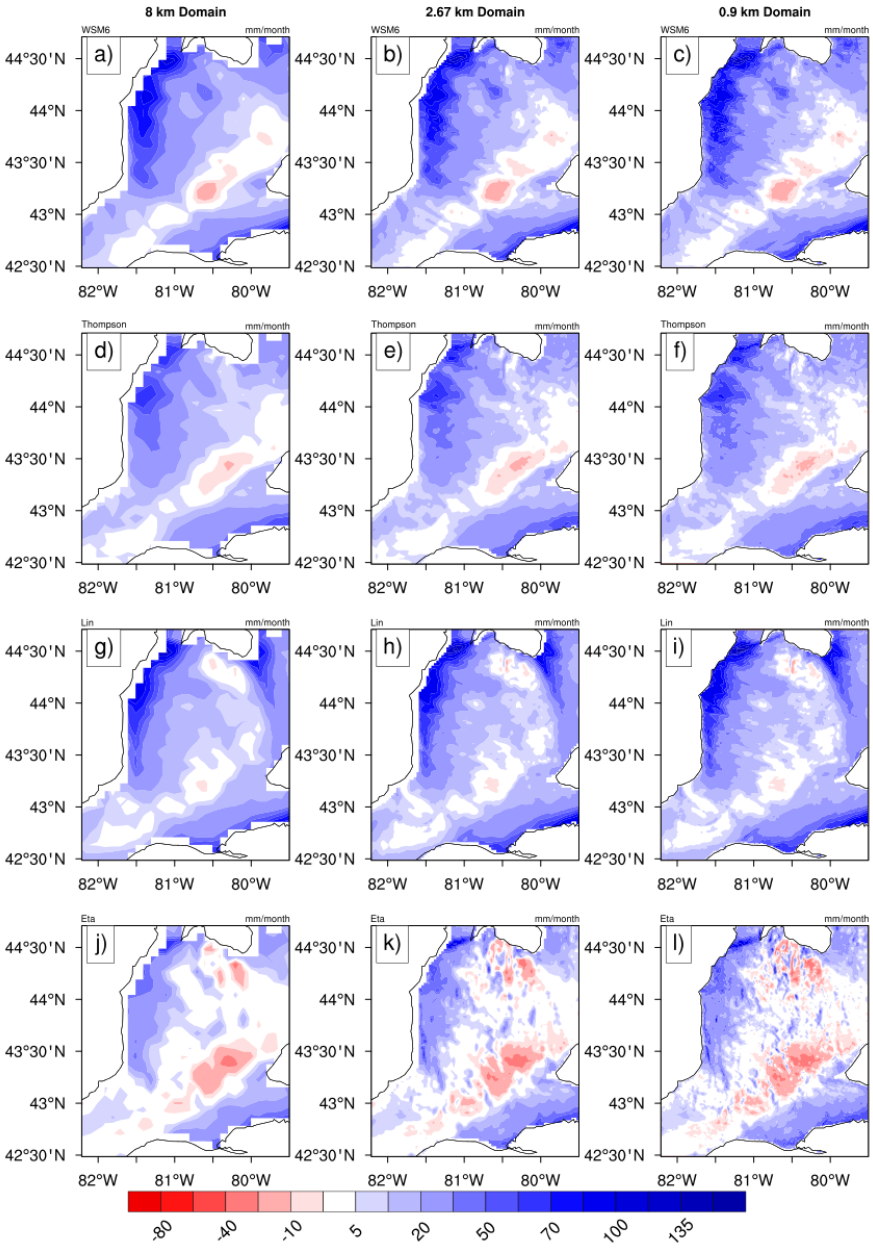

Figure 5.9: The spatial distribution of total precipitation bias for January 2002 for five MP schemes: WSM6 (a, b, and c), Thompson (d, e, and f), Lin (g, h, and i), and Eta (j, k, and l); for three horizontal grid resolutions: 8km domain (left column), 2.67km domain (middle column) and 0.9km domain (right column).

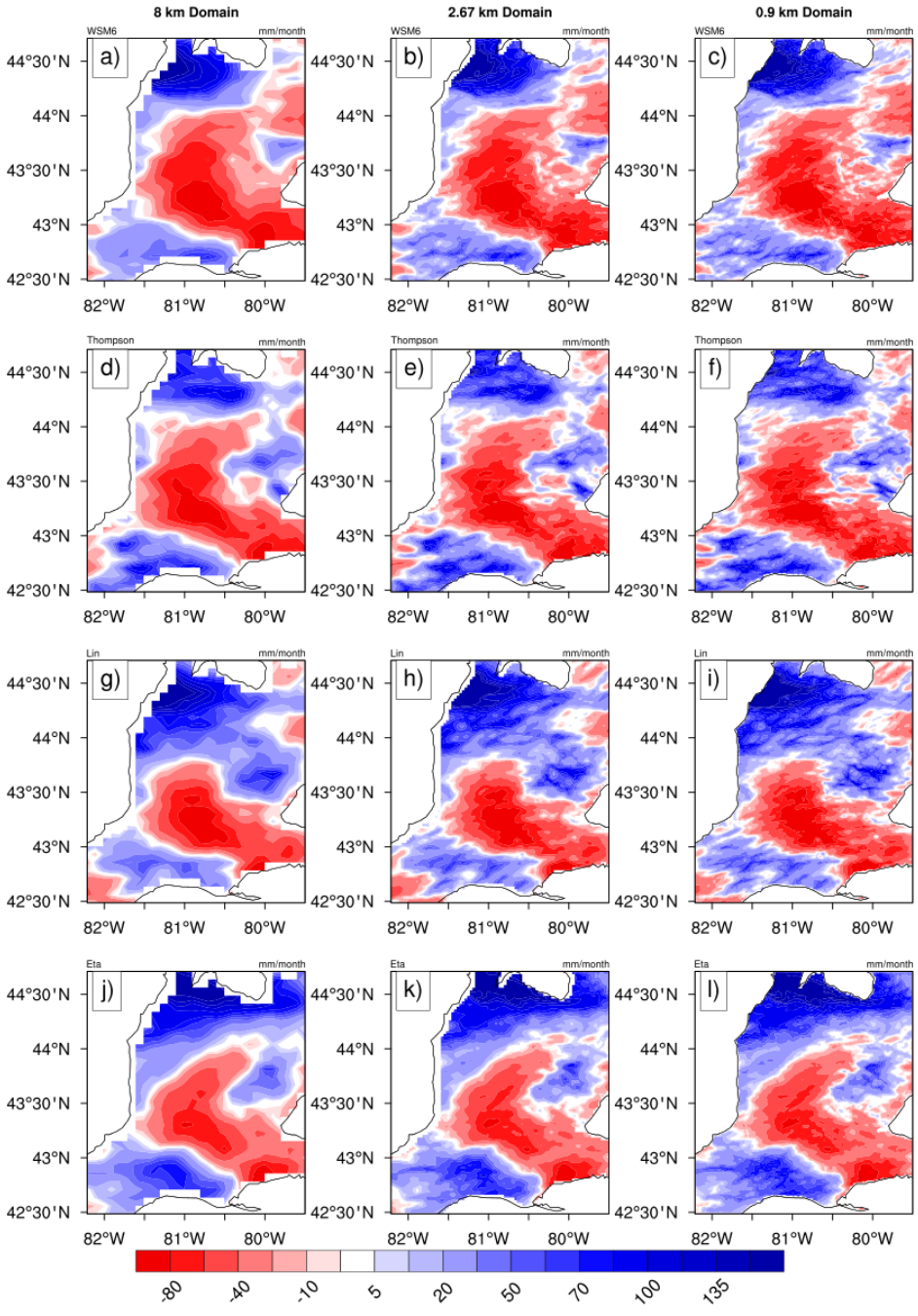

Figure 5.10: As in Figure 5.9 but for July 02

Physical Interpretation of Precipitation Characteristics

To better understand the spatio-temporal differences in precipitation patterns, area-averaged vertical profiles of the five hydrometeor species plus the graupel mixing ratio from the innermost domain equivalent areas of the outermost domain (grid spacing 8km) are presented in Figure 5.11 (a-e). The ETA scheme does not contain ice and graupel categories. As can be seen from the plots, sub-domain averaged hydrometeor profiles show significant variability to the choice of microphysics schemes.

Figure 5.11 (c) indicates that, except for WSM6, all MP schemes show a lower amount of ice from the mid to lower troposphere, especially in the below-600 hPa column. It is not surprising to see that WSM6 scheme simulates more ice in the lower atmosphere with a warmer temperature, given that its formula does not depend on temperature.

In Figure 5.11 (d), snow clearly dominates all hydrometeor types, followed by cloud water, except for the PLIN, which produces the largest amount of graupel. The relatively higher falling velocity of the graupel [56] among all hydrometeor categories can partially explain the highest accumulated total precipitation (refer to Figure 5.5) simulated by the PLIN scheme. As shown in Figure 5.11 (e), the two most-sophisticated MP schemes, THOM and M2M, produced a negligible amount of grauple and the least accumulated total precipitation (also refer to Figure 5.5).

The hydrometeor species change their phase by absorbing (releasing) heat from (to) the environment in the form of latent heat (LH), which influences the vertical velocity, cloud cover, and thermodynamic profile throughout the troposphere. Therefore, the vertical profiles of the area-averaged cloud cover and diabatic heating rate is presented in Figure 5.12 to better clarify the characteristics of different hydrometeor species.

Increased values of LH in the middle troposphere act as positive feedback, energizing air parcels to transport to higher levels. When an air parcel reaches freezing levels, cloud ice begins to form, as can be seen in Figure 5.11 (c). It should be noted that in the case of PLIN and THOM schemes, with temperatures warmer than $-27\,^{\circ}\mathrm{C}$, cloud ice auto-converts to snow (Otkin *et al.*, 2006 [74]). Furthermore, upon contact with cloud ice and mixed phase hydrometeors (snow and graupel), water vapor freezes and releases LH from the middle to upper troposphere. The higher values of LH from the middle to upper troposphere in Figure 5.12 (b) and (d) can be explained by the physical mechanism described above. Indeed, the higher concentration of mixed-phase hydrometeors in the middle tropospheric column produces increased rain-water masses successively (Figure 5.11 (b)).

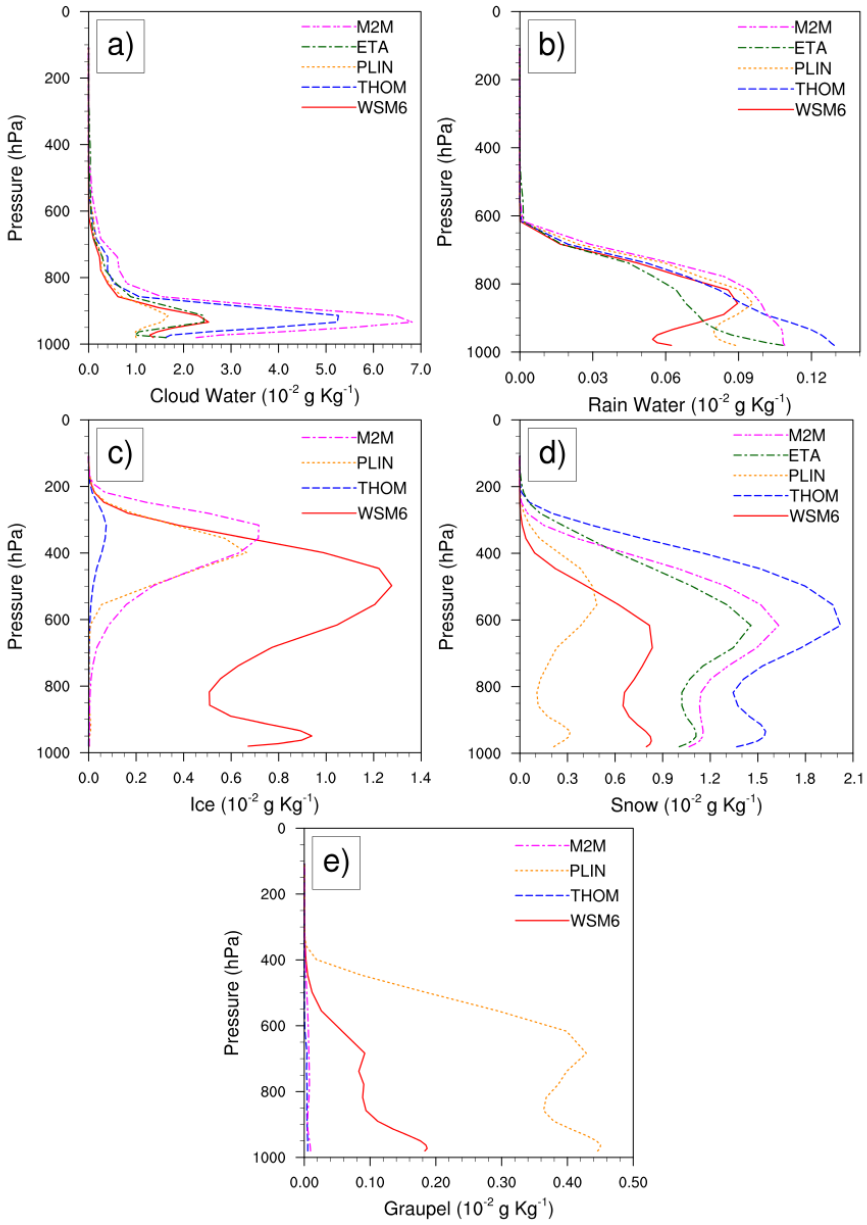

Figure 5.11: Spatially and temporally averaged WRF-simulated hydrometeor profiles of (a) cloud water, (b) rain water, (c) ice, (d) snow, and (e) graupel using five different microphysics schemes Table 2.5.

Surprisingly, the THOM scheme produces comparatively lower amounts of surface pre-

cipitation, although it shows large values of snow and rain water mixing ratios (Figure 5.11 (d)). As stated earlier, the THOM scheme uses prognostic equations to predict the total ice particle and rain droplet number concentration; therefore, for this scheme can produce large numbers of tiny droplets with small fall velocity, which may result in a low surface precipitation total. The above analyses demonstrate the strong relationship among microphysical processes, atmospheric dynamics, and thermodynamics.

In conclusion, performance of MP schemes clearly depends on various factors, including the type of hydemeteor species, annual climatological conditions, and Great Lakes ice cover statistics. All CMPs have some limitations. Overall, the WSM6 scheme is better at simulating surface precipitation totals, both for January and July 2002. Accordingly, the WSM6 scheme gives higher CC, the lowest RMSD, and NSD. Results from this study are in agreement with those of [57], who carried out WRF model MP sensitivity experiments to simulate winter time precipitation over the Colorado headwaters region.

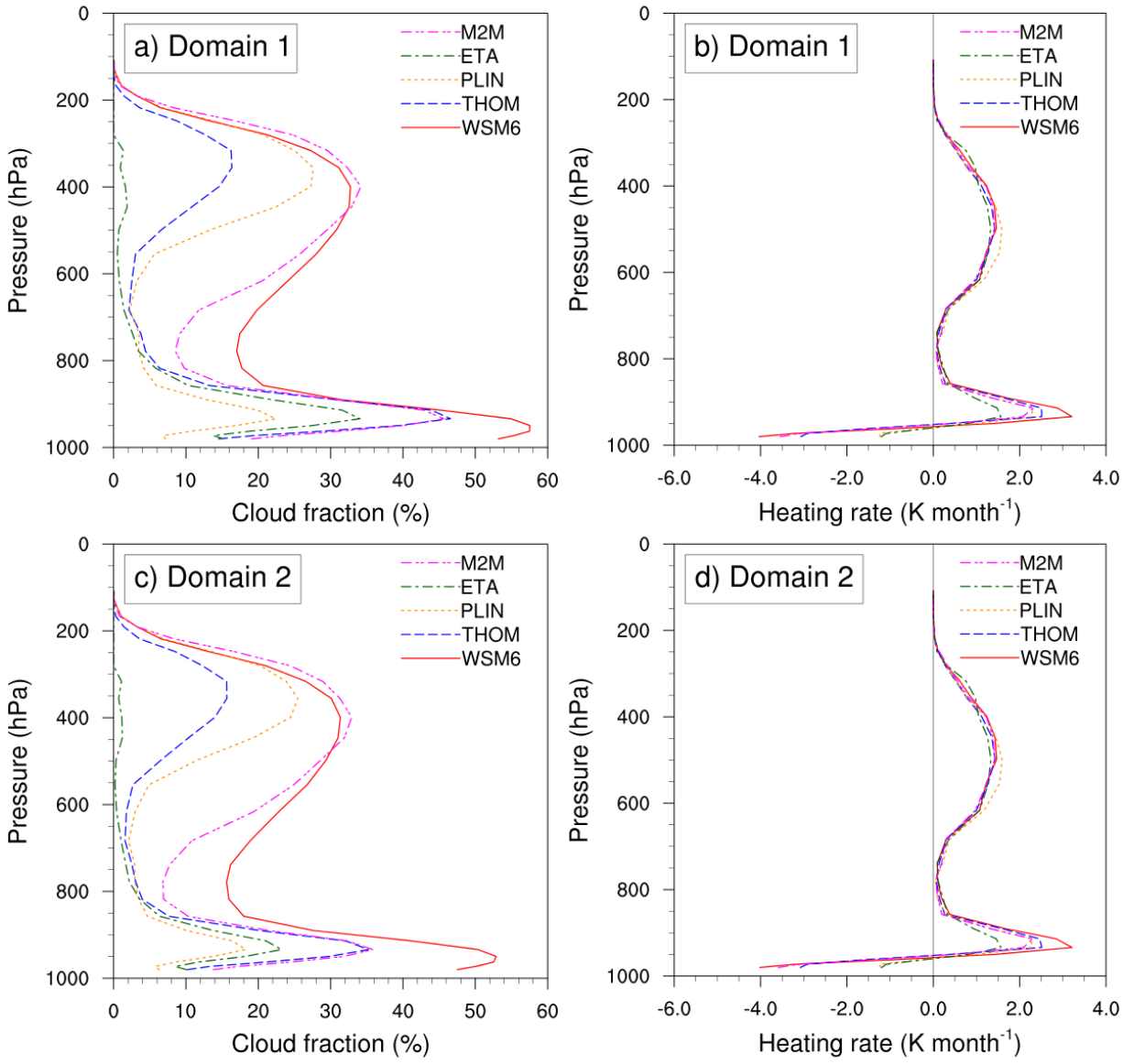

Figure 5.12: Spatially and temporally averaged cloud fraction and diabatic heating profiles using five different microphysics schemes for domain 1 (a, b) and domain 2 (c, d).

5.5.2 Temperature

Figure 5.13 compares the diurnal cycles of maximum temperature at two meter height. Generally, all the MP schemes simulated similar temporal fluctuations, ones that match quite well with observations. In the same way, WRF shows a large temperature bias during extreme temperature conditions for all schemes, both in January and July, 2002. Surprisingly, the model showed an underestimation on January 27 and 28. During those two days, a major winter storm passed over southern Ontario, leading to large accumulation of snow. The model overestimated both the daily maximum and minimum temperatures during the period of clear sky conditions in January (Figures 5.13 and 5.14). In a typical winter night with a cloud-free sky, the temperature at the earth's surface drops sharply, a fact which supports observed temperature patterns. On average, the simulated two-meter temperature is $2\,^{\circ}C$ higher than that observed. The time series of the WRF-simulated mean temperatures at the two-meter height (T2mean) averaged over the innermost domain areas shows very good agreement with DAYMET observations, except for a small overestimation in January (not shown). All the MP schemes show a large mean temperature bias while simulating extreme cold temperatures.

Figures 5.15 and 5.16 illustrate the spatial distribution of monthly maximum temperature biases at the two-meter height for January and July 2002, respectively. All the schemes display nearly identical distribution in January, except for ETA's relatively lower bias. As a result, this study concludes that the broad patterns are generally insensitive to the MP scheme. In July, the Thompson scheme shows a slightly lower bias than the other three schemes, although the general patterns are nearly identical. In the case of maximum temperature, all schemes show a common temperature distribution, with underestimation along the shore of the Great Lakes and overestimation in the interior of the domain. Comparing Figures 5.17 and 5.18 indicates that the spatial distribution of January minimum temperatures shows large overestimation by all five schemes. All MP schemes show a characteristic maximum and minimum temperature bias over the Niagara Escarpment (Ontario's greenbelt). In the case of the mean two-meter temperatures (Figures 5.19 and 5.20), all schemes give their lowest temperature bias over the Niagara Escarpment.

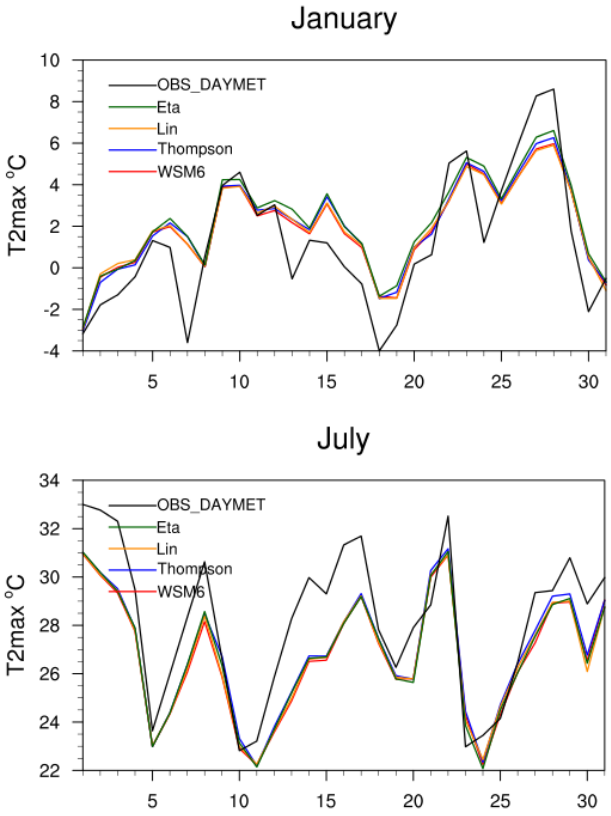

Figure 5.13: Time-series of simulated daily maximum surface air temperature at a two-meter height from the Earth's surface. In all cases, the black lines represent DAYMET observations.

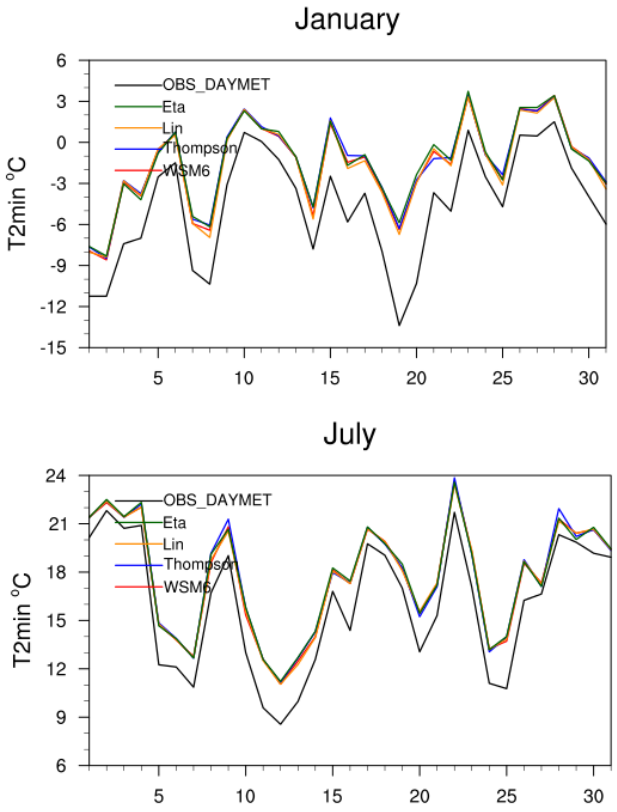

Figure 5.14: The same as Figures 5.13 but for T2min.

The domain-averaged root-mean-square-error (RMSE) of daily T2max, T2min, and T2mean temperatures at a two-meter height are presented in Table 5.2. A comparatively large bias in the spatial distribution of the T2min is also evident in the RMSE calculations.

Table 5.2: Root mean square error for WRF MP schemes

	$T2_{max}$			$T2_{min}$			$T2_{mean}$		
	$d01$	$d02$	$d03$	$d01$	$d02$	$d03$	$d01$	$d02$	$d03$
Jan 2002									
$WSM6$	1.79	1.78	1.77	3.50	3.40	3.32	2.30	2.25	2.20
$Thompson$	1.83	1.81	1.80	3.64	3.55	3.46	2.39	2.34	2.29
Lin	1.83	1.82	1.80	3.40	3.31	3.22	2.29	2.24	2.19
Eta	1.91	1.89	1.88	3.65	3.58	3.49	2.42	2.37	2.32
Jul 2002									
$WSM6$	2.134	2.030	1.956	2.004	1.937	1.849	0.806	0.784	0.773
$Thompson$	1.993	1.892	1.820	2.095	2.031	1.945	0.843	0.828	0.820
Lin	2.094	1.992	1.917	2.007	1.939	1.851	0.835	0.815	0.804
Eta	2.051	1.947	1.873	2.092	2.029	1.942	0.784	0.763	0.750

The WSM6 MP scheme gives the lowest RMSE both in January and July, except for the T2max in July, when the THOM scheme gives the lowest RMSE.

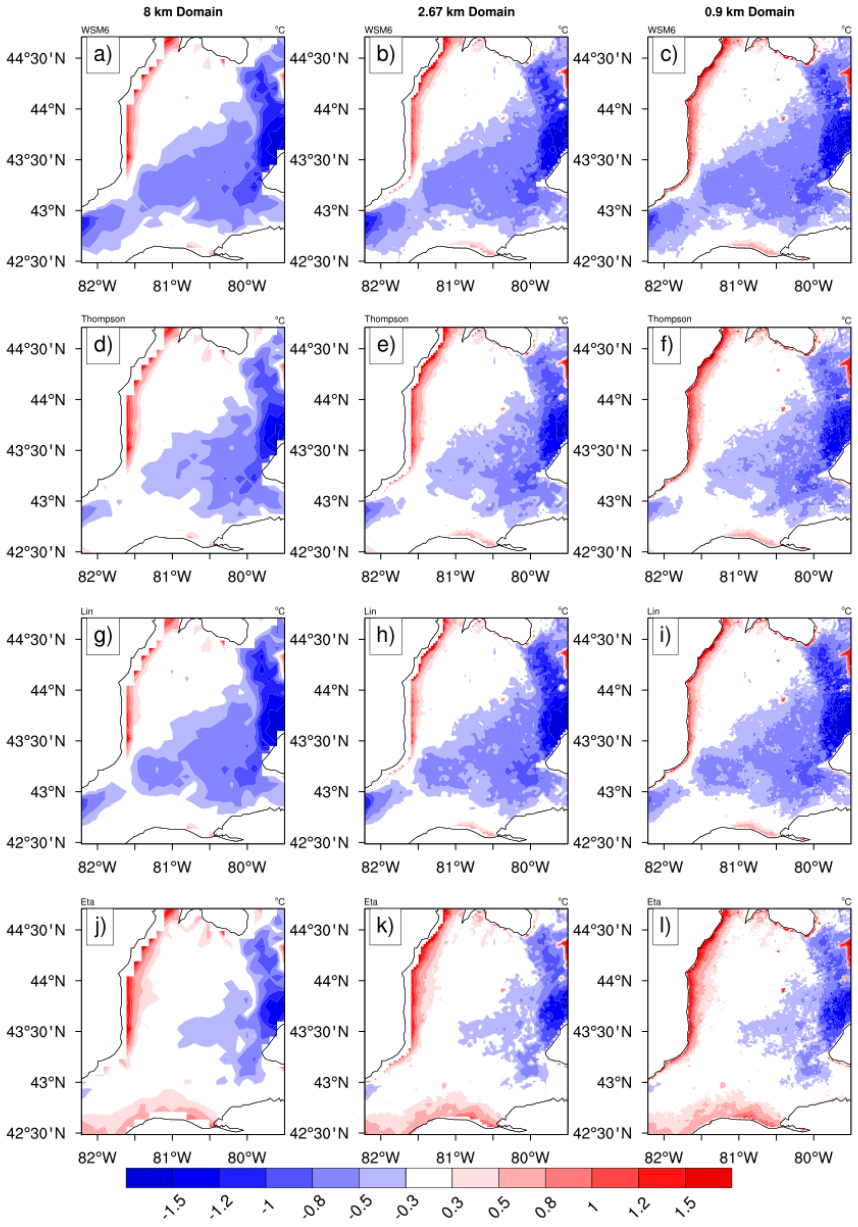

Figure 5.15: The spatial distribution of mean maximum temperature bias in ° C for January 2002. Sensitivity to different MP schemes: WSM6 (a, b, and c), Thompson (d, e and f), Lin (g, h, and i), and Eta (j, k, and l). Sensitivity to grid spacing: 8km domain (left column), 2.67km domain (middle column) and 0.9km domain (right column).

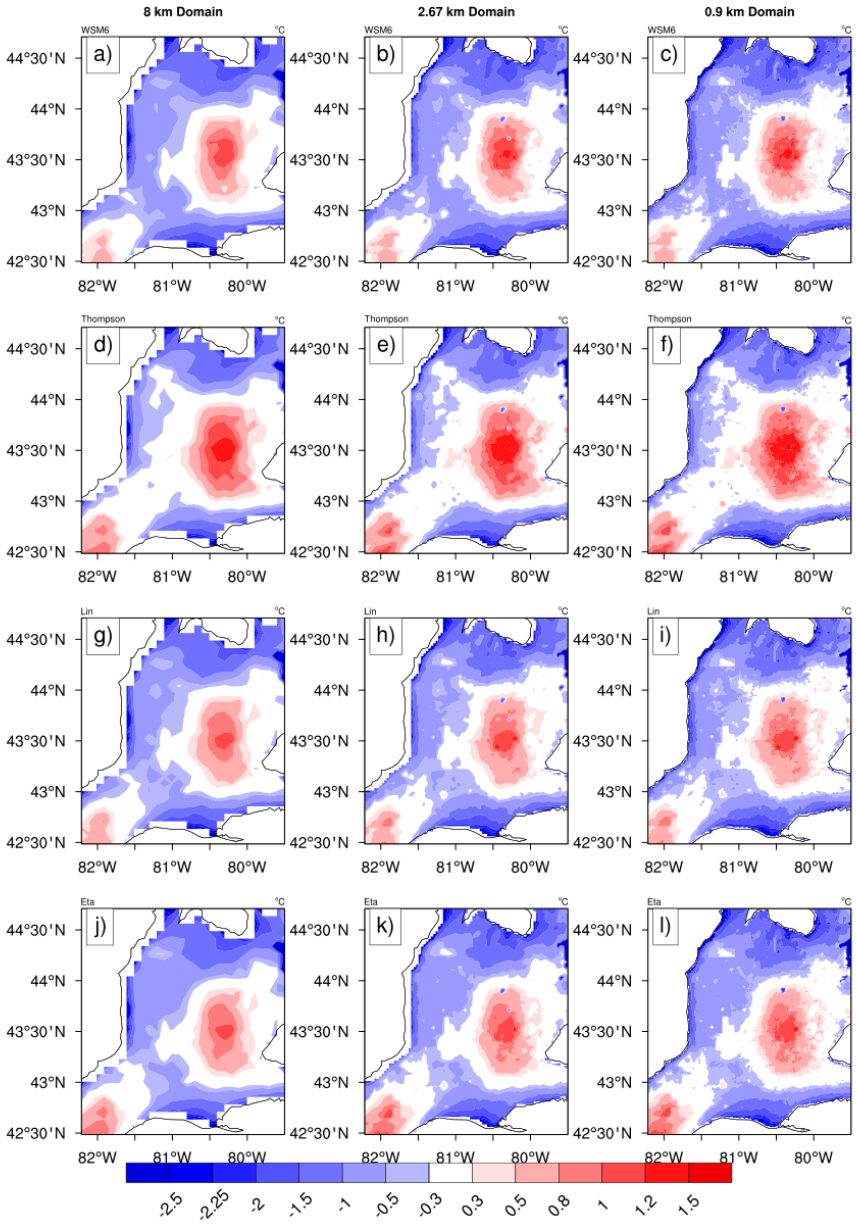

Figure 5.16: As in Figure 5.15 but for July

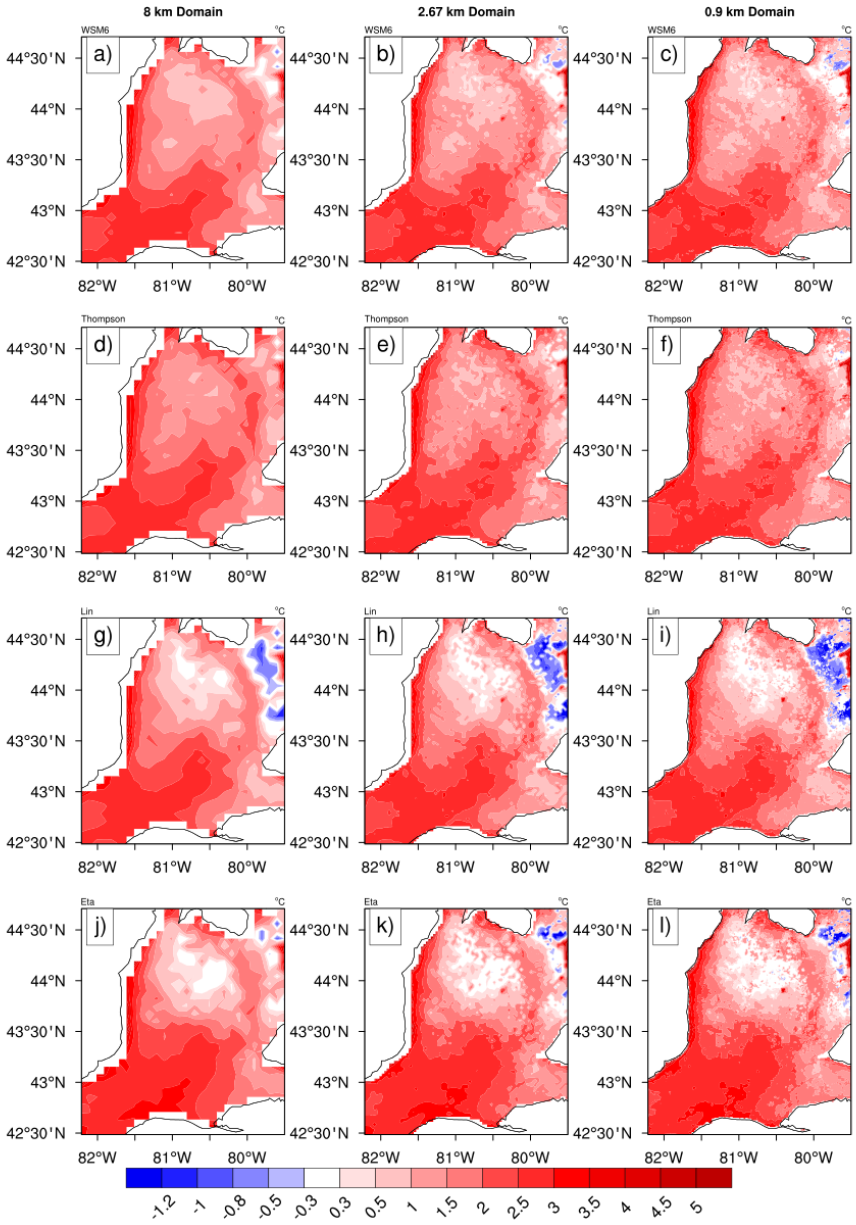

Figure 5.17: The spatial distribution of monthly mean minimum temperature bias in ° C for January 2002. Sensitivity to different MP schemes: WSM6 (a, b, and c), Thompson (d, e and f), Lin (g, h, and i), and Eta (j, k, and l). Sensitivity to grid spacing: 8km domain (left column), 2.67km domain (middle column) and 0.9km domain (right column).

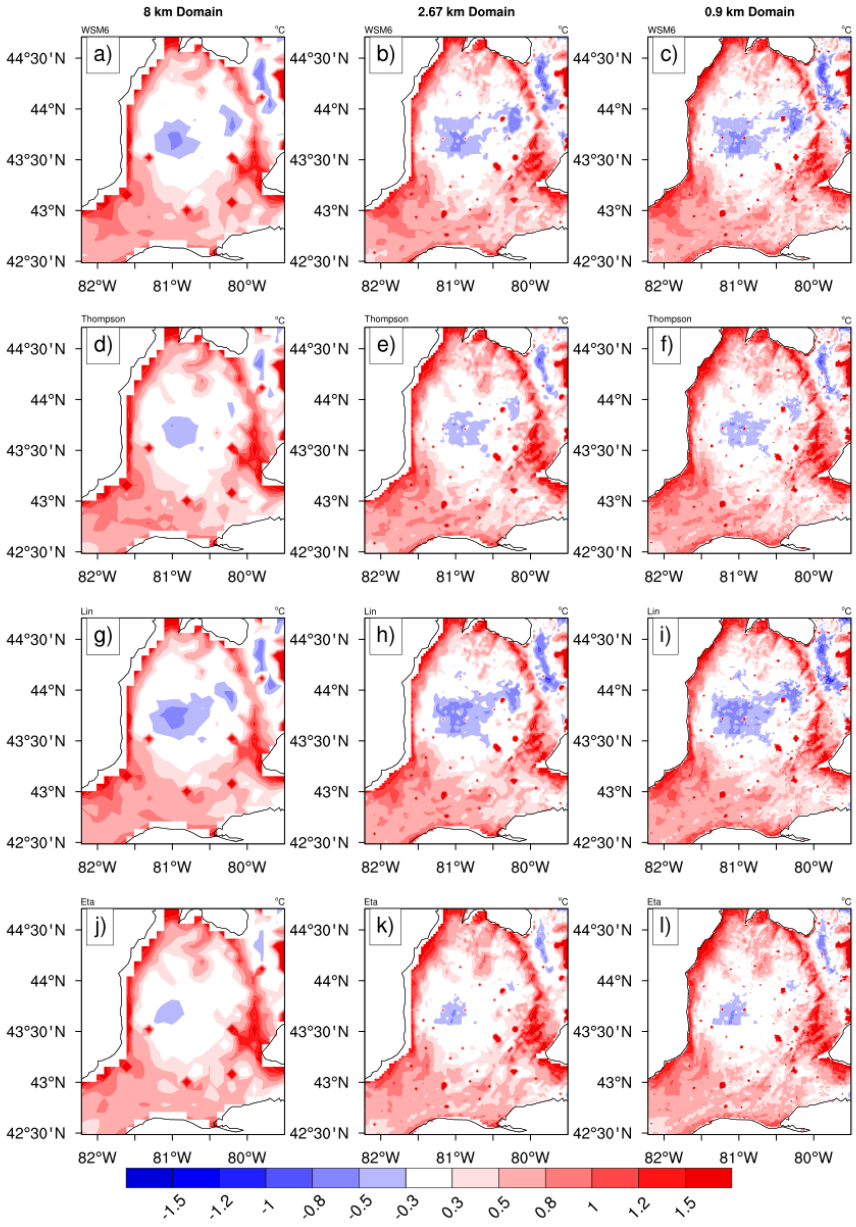

Figure 5.18: As in Figure 5.17 but for July.

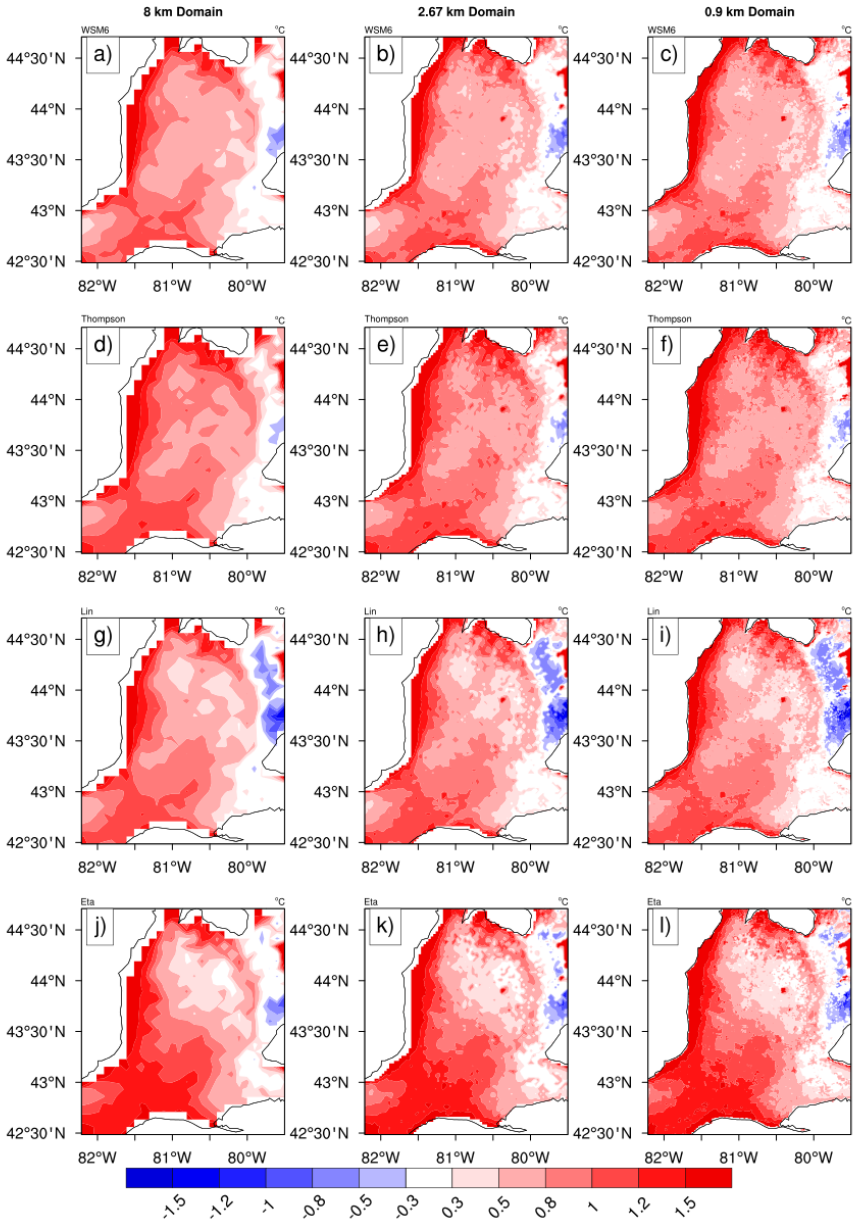

Figure 5.19: The spatial distribution of monthly mean temperature bias in ° C for January 2002. Sensitivity to different MP schemes: WSM6 (a, b, and c), Thompson (d, e and f), Lin (g, h, and i), and Eta (j, k, and l). Sensitivity to grid spacing: 8.0 km domain (left column), 2.67 km domain (middle column) and 0.89 km domain (right column).

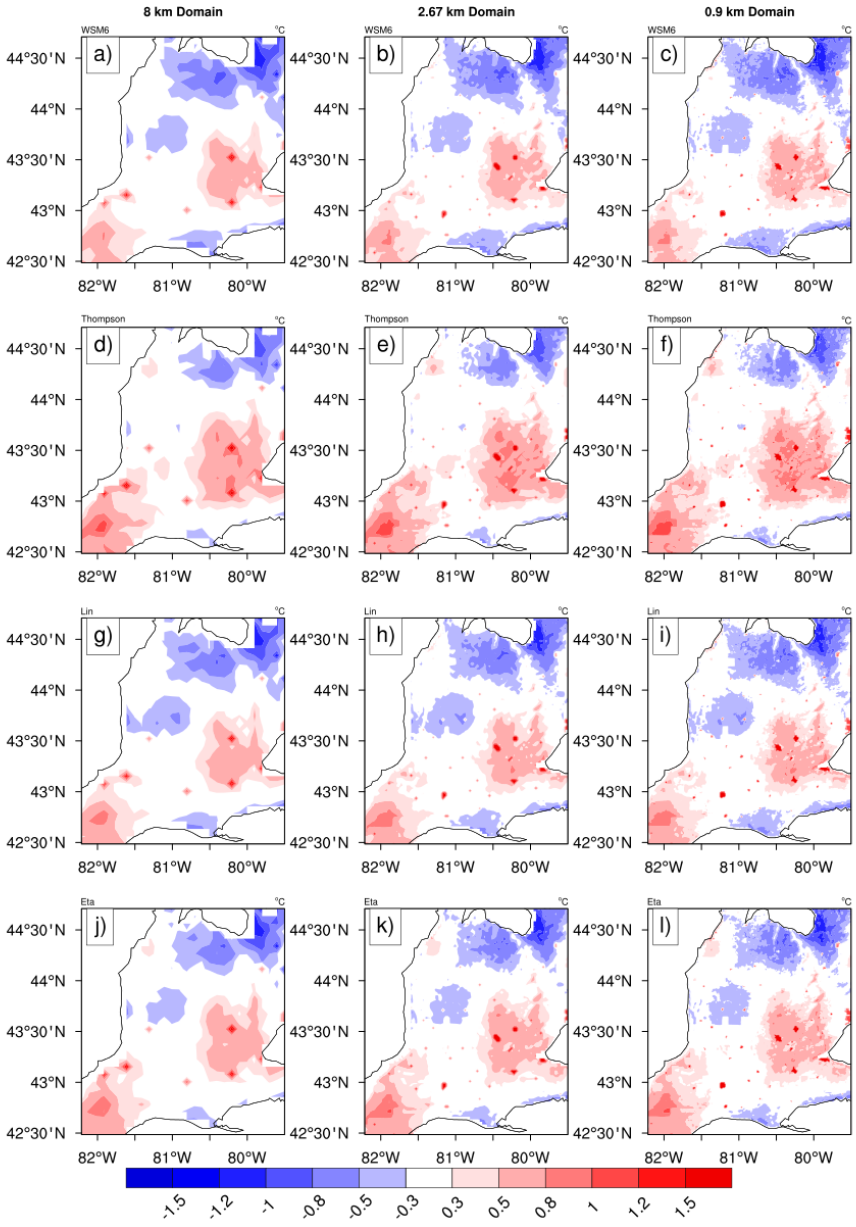

Figure 5.20: As in Figure 5.19 but for July.

Figures 5.21, 5.22, and 5.23 represent the Taylor statistics for the daily maximum, minimum, and mean temperatures, respectively. The Taylor diagram of the daily maximum temperature at the two-meter height shows CC ~ 0.9, low RMSD $\sim 0.5\,^{\circ}C$ and lower SD

(0.5) in both January and July, 2002. Close clustering of the points indicates that the simulated daily maximum temperature is not very sensitive to the choice of MP scheme. The WRF model is skillful in simulating the daily minimum temperature with a CC higher than 0.95. The WRF model's performance was outstanding for the two-meter temperature, with almost perfect skill in July and a very low bias in January.

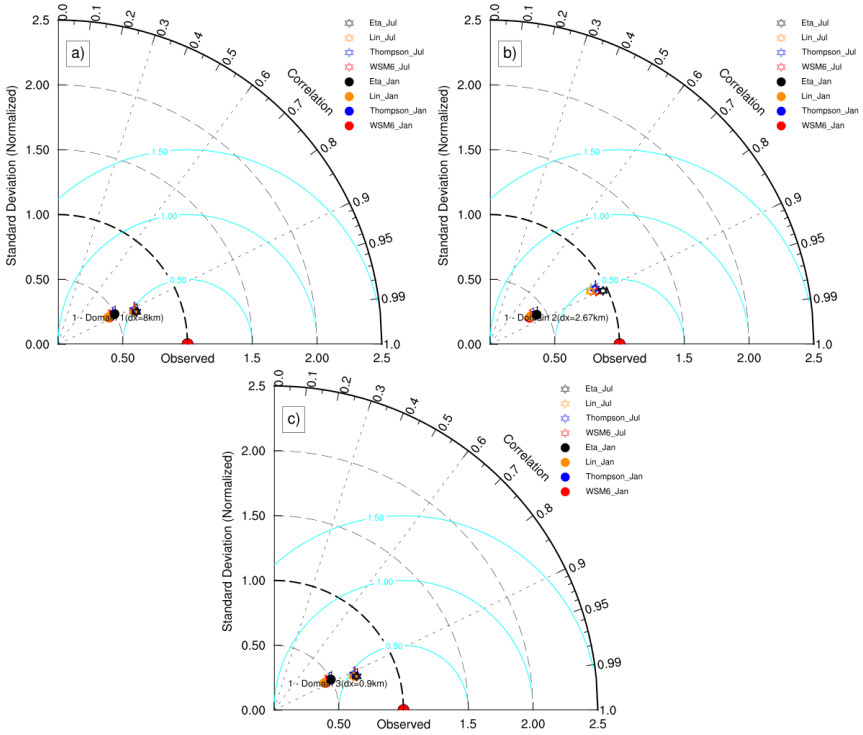

Figure 5.21: Taylor diagram showing correlation coefficient, and standard deviation of daily maximum temperature relative to DAYMET observation of the twelve WRF simulations listed in Table 2.2 for the month of January (left panel) and July (right panel) of 2002 over Southern Ontario, Canada.

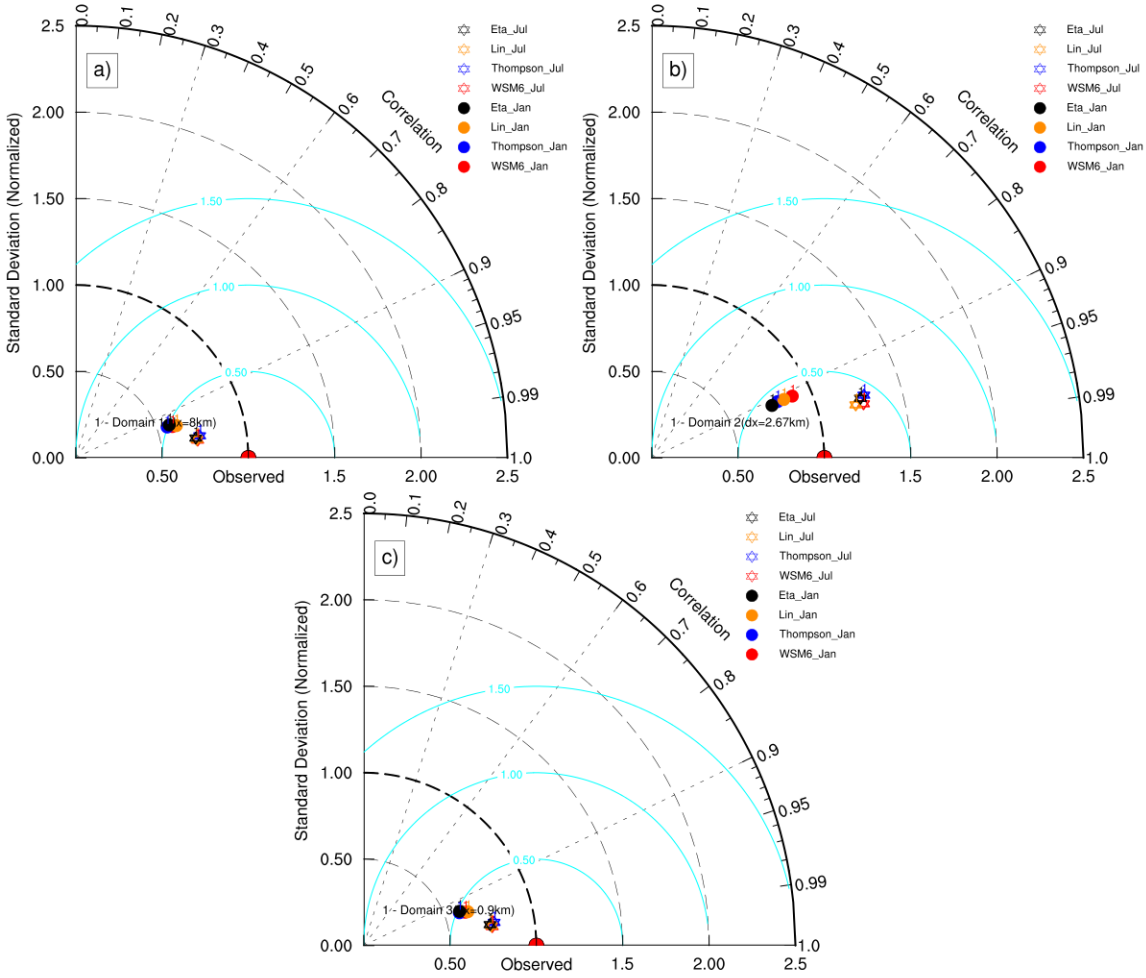

Figure 5.22: As in Figure 5.21 but for daily minimum temperature.

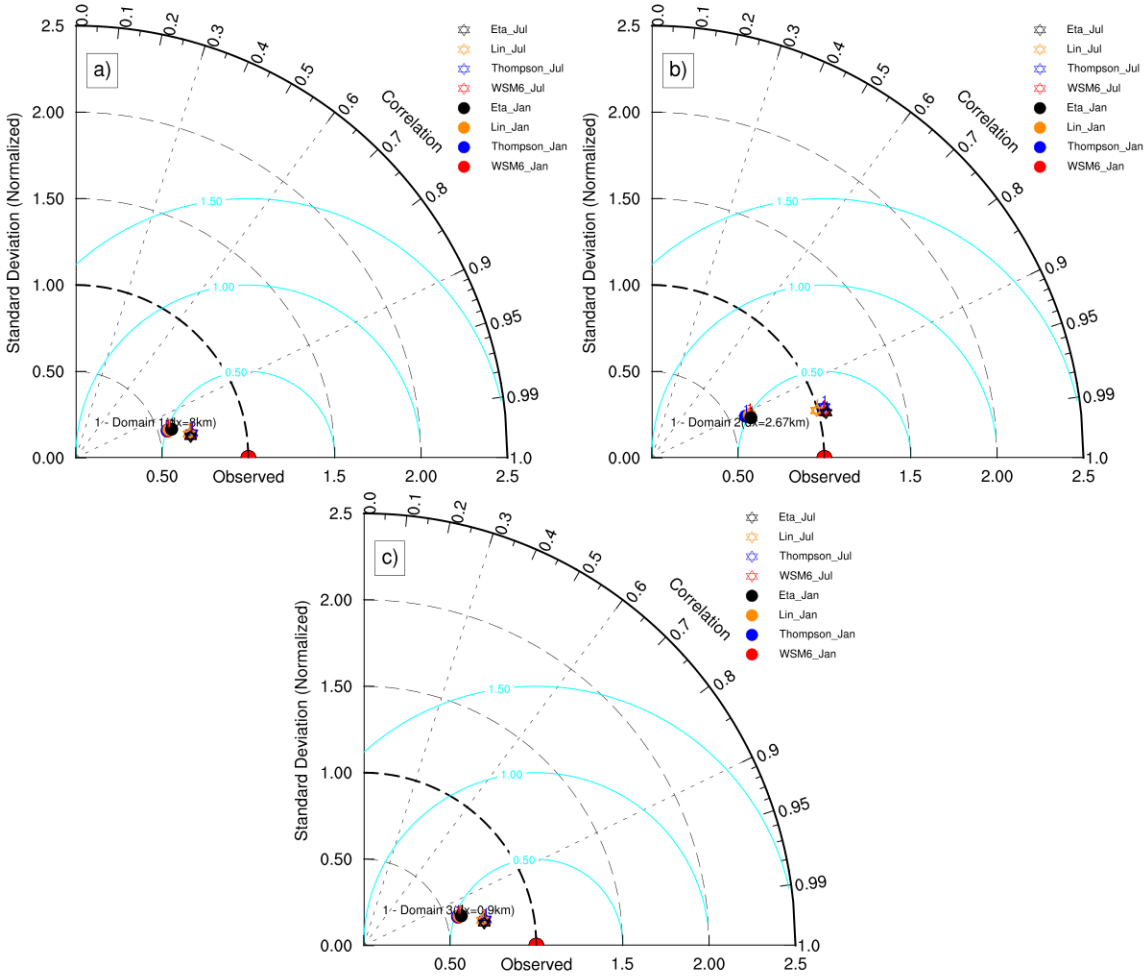

Figure 5.23: As in Figure 5.21 but for daily mean temperature.

5.6 Conclusion

In the WRF model, grid-scale precipitation results when the MP scheme removes atmospheric instability. In a cloud-resolving simulation, all precipitation results from micro-

physical parameterization; therefore, it is very important to assess a microphysical parameterization scheme's performance before using it. This study investigated the performance of five MP schemes in reproducing observed variabilities of precipitation and temperature variables.

The results reveal that all the CMPs tested perform almost equally for the spatial distribution of precipitation. The Taylor statistics indicate that the WSM6 scheme slightly outperforms the others in terms of pattern CC and RMSE. The PDF analysis clearly indicates that the WSM6 scheme shows better skill in capturing both low- and high-frequency precipitation events than the others. Overall, the WSM6 MP scheme performed best in simulating surface precipitation totals both for January and July, with the best results for January. Model-simulated temperatures were found to be not very sensitive to the choice of MP scheme. All the MP schemes showed a large mean temperature bias while simulating extreme cold temperatures and a characteristic maximum and minimum temperature bias over the Niagara Escarpment (Ontario's greenbelt). The WSM6 scheme also gives the best overall performance in simulating maximum, minimum, and mean temperature variabilities at a two-meter height. Even though the Thompson (THOM) and Morrison two-moment (M2M) were two most-sophisticated MP schemes, they did not produce the best forecasting skill score.

In conclusion, this study has shown that the WSM6 MP scheme outperforms the other schemes in the scale of matrices applied. Nevertheless, interesting and relevant questions still need to be answered, such as which MP scheme shows better performance in simulating vertical profiles of different hydrometeor species. The MP scheme performance depends on several factors, including the type of hydrometeor species, annual climatological conditions, and Great Lakes ice cover statistics.

Chapter 6

Evaluation of WRF Model Performance in Simulating Surface Energy Balance

6.1 Introduction

This study examines the WRF model's ability to simulate major surface energy fluxes over southern Ontario, Canada. To the best of our knowledge, this is the first sensitivity study that investigates the WRF model's credibility in simulating major energy flux components over the Great Lakes regions. Examining surface energy flux sensitivity along with the WRF model's physical parameterizations offers the opportunity to test the WRF model's forecast performance over a particular area, highly affected by lakes, large seasonal temperature difference, Jet stream, and synoptic disturbances. A detailed descriptions of the model, data, and experimental design are discussed in Chapter 2. The results from this study are presented in Section 2, followed by a discussion of the results in Section 3. Finally, the conclusion and recommendations are presented in Section 4.

6.2 Results

This study evaluates WRF model's forecast skill in simulating SHF, LHF, and GHF and also investigates their sensitivity to different PBL parameterization schemes and annual

climatic conditions of the input atmospheric initial and boundary conditions. The subsection below present results from diurnal evolution of surface energy fluxes, PBL parameterization, and annual climatological atmospheric conditions sensitivity studies. The abbreviations used in the following sections and subsections are summarized in Table 2.1.

6.2.1 Diurnal Evolution of Surface Energy Fluxes

Figure 6.1 compares the diurnal evolution of WRF-simulated LHF and SHF against Strawberry Creek EC tower observations. It can be seen that the model consistently overestimated LHF for the whole time period (top row in Figure 6.1). However, the model's performance in capturing the diurnal variability of SHF is excellent compared to EC observations both 2007 and 2008 (bottom row in Figure 6.1). The findings of this study agree well with the findings of Eder *et al.* (2014) [21], who reported the model's persistent underestimation of turbulent heat fluxes compared to EC measurements. The conventional wisdom is that, because of the coarse grid resolution of RCM, it does not see the surface level roughness heterogeneity the same way as an EC tower does. Hence, the disagreement between the model and EC measurement.

It should be noted that Strawberry Creek EC observations represent energy fluxes only for small areas of the southern Ontario domain. Therefore, in order to increase the reliability of the current study, WRF simulations must be evaluated against observations or an analysis data set that contains horizontal coverage at least for the entire study area. This study thus compares WRF simulations with the NLDAS-2 LSM-gridded analysis generated by the above-three LSMs.

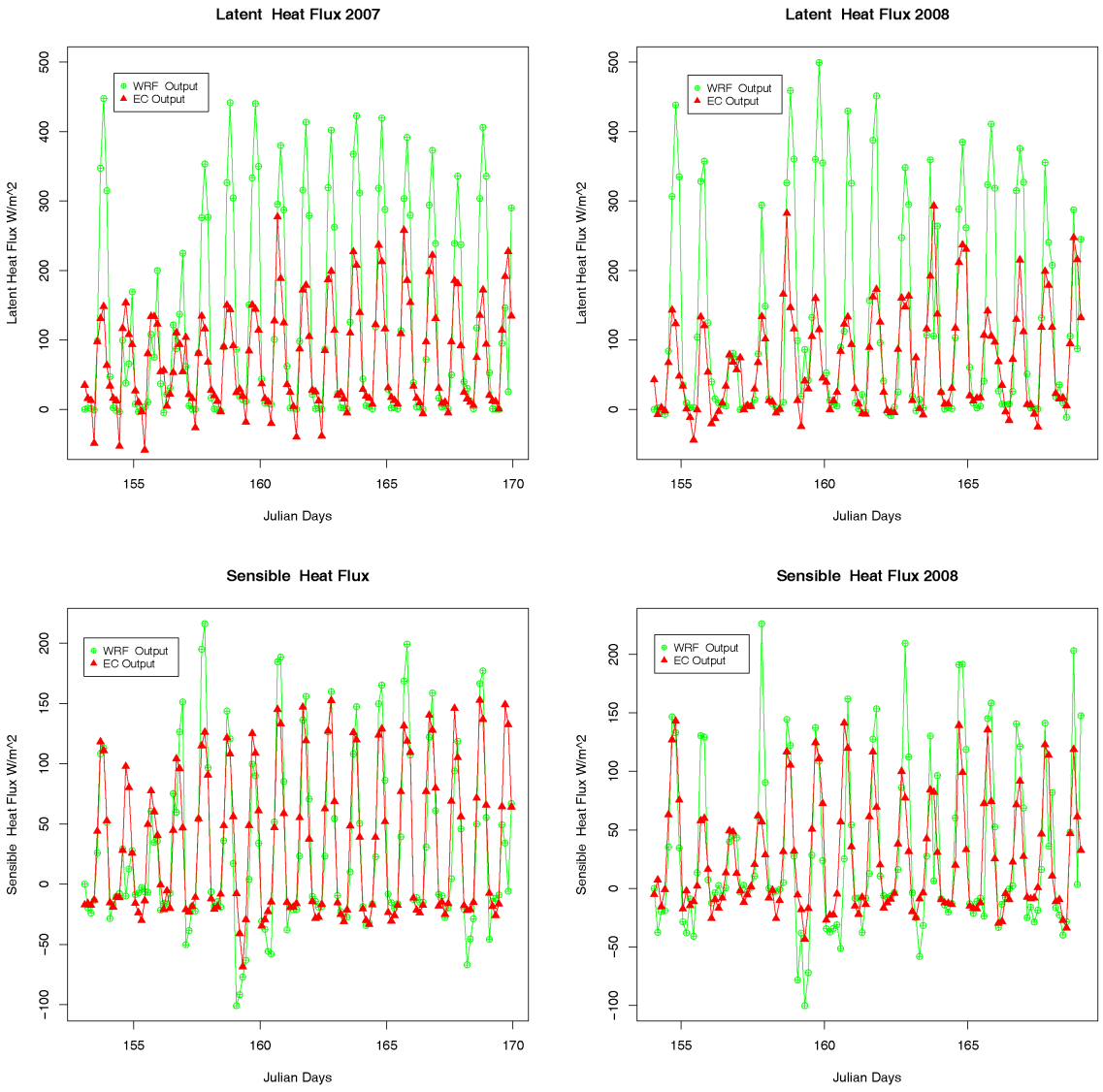

Figure 6.1: Comparison of latent (top row) and sensible (bottom) heat flux measured from eddy covariance tower with model-derived flux for the years a) 2007 (left panel) and b) 2008 (right panel). EC measurement (red triangle) and WRF simulations (green circle).

6.2.2 Surface Energy Flux Sensitivity to PBL Schemes

Figure 6.2 (a-l) illustrates the spatial distribution of the simulated mean LHF bias compared to the NLDAS-2 MOSAIC model output for January 2002. We find that the spatial patterns of simulated LHF in January are in good agreement with NLDAS-2 model output. A comparison of the four PBL schemes reveals that LHF is overestimated by the non-local YSU (Figure 6.2 a-c) and hybrid ACM2 (Figure 6.2 d-f) schemes and underestimated by the local schemes MYJ (Figure 6.2 g-i) and MYNN2 (Figure 6.2 j-l). Out of the four PBL schemes studied, the ACM2 PBL scheme shows the lowest overall bias in January, followed by the YSU. The overall LHF biases are between -25 and 25 Wm^{-2}. On the other hand, in July, no individual PBL scheme outperformed the others, as shown in Figure 6.3. The model overestimated fluxes in the interior part of the domain and underestimated them for other areas. The spatial distributions of monthly mean SHFs for January and July of 2002 are shown in Figure 6.4 (a-l) and 6.5 (a-l), respectively. The model shows an apparent overall underestimation in January. In July, simulated SHF showed similar behavior as shown in Figure 6.2 for LHF. Our results comply with those of LeMone *et al.* (2007) [52], who noticed similar energy flux patterns.

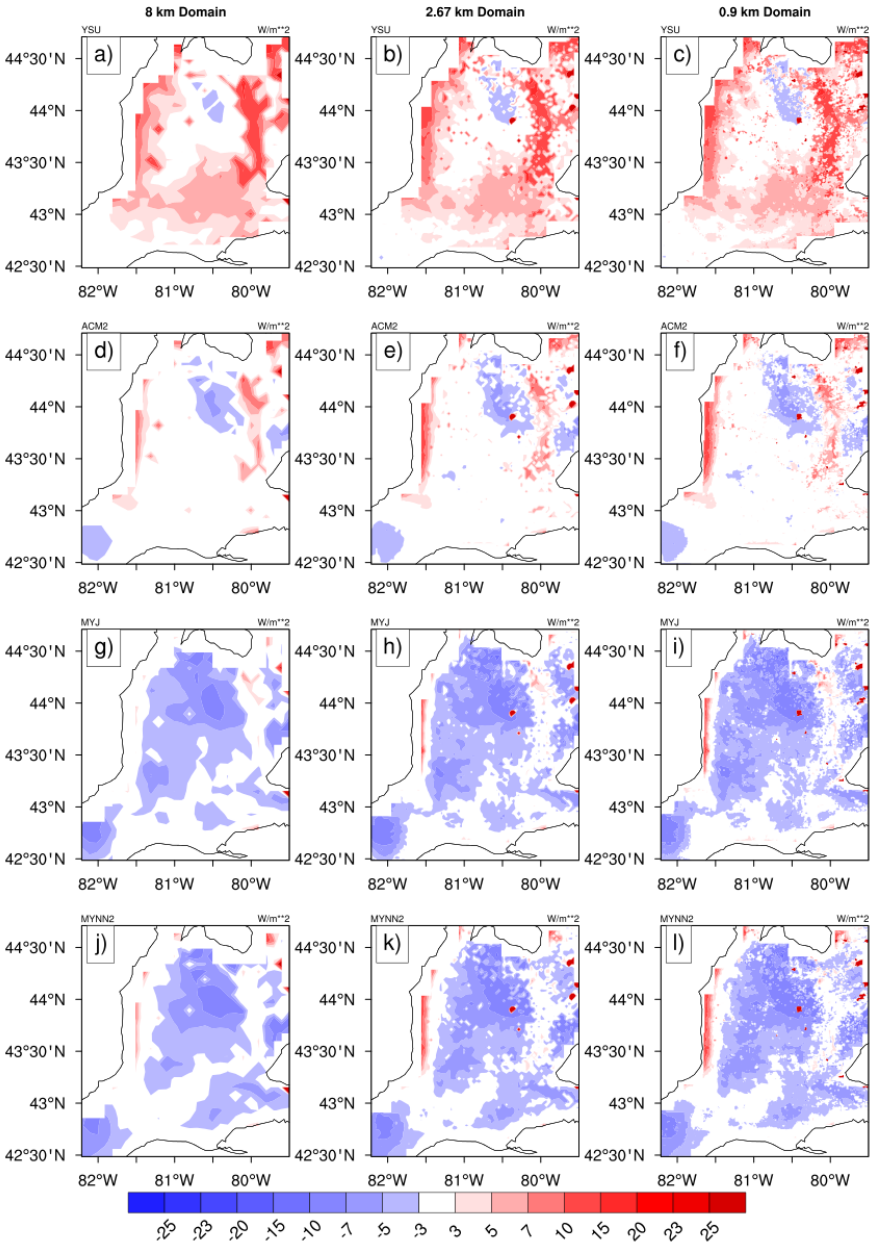

Figure 6.2: Mean latent heat flux bias in Wm^{-2} for January 2002. The four PBL schemes (i.e., YSU, ACM2, MYJ, and MYNN2) are arranged from top to bottom, whereas simulations with grid spacing of 8km, 2.67 km, and 0.888km are shown from left to right.

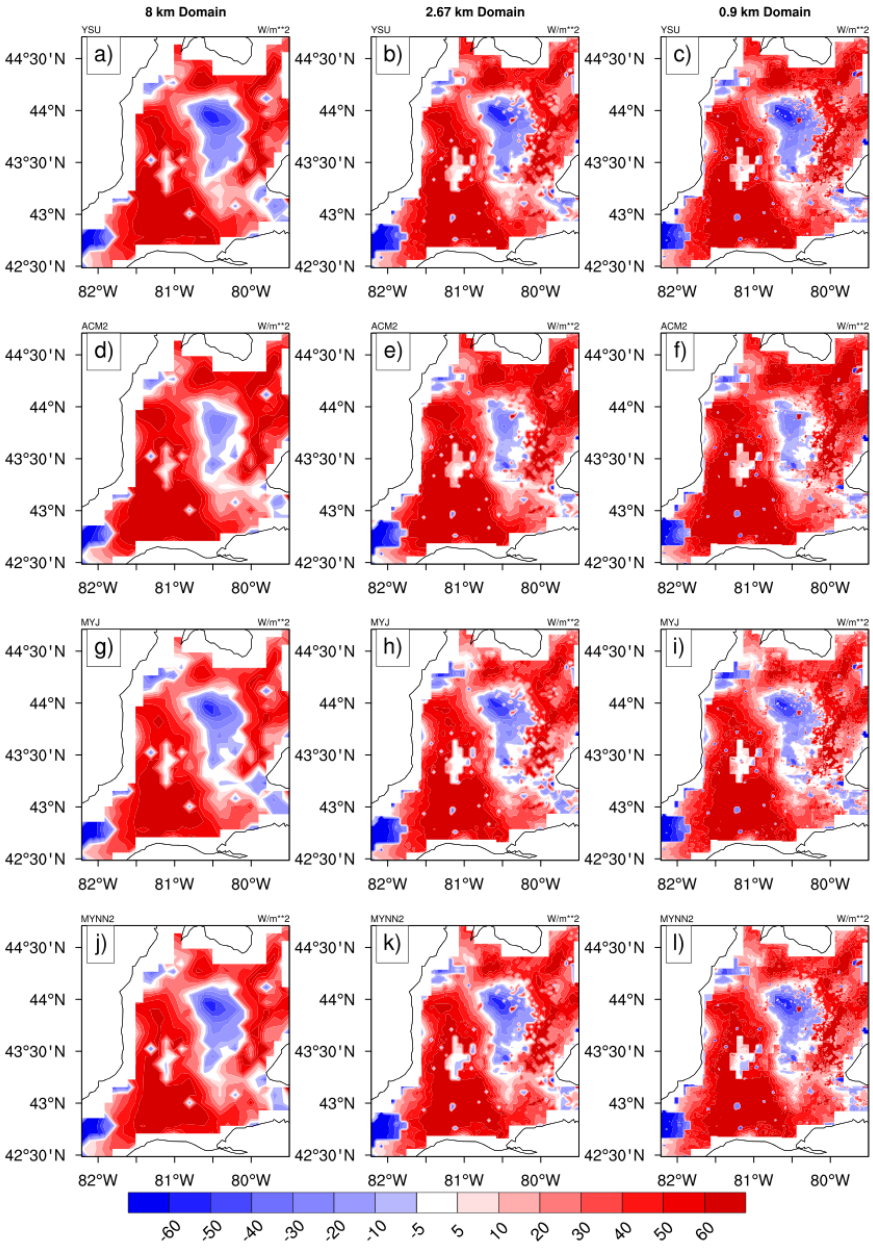

Figure 6.3: The same as Figure 6.2 but for July 2002.

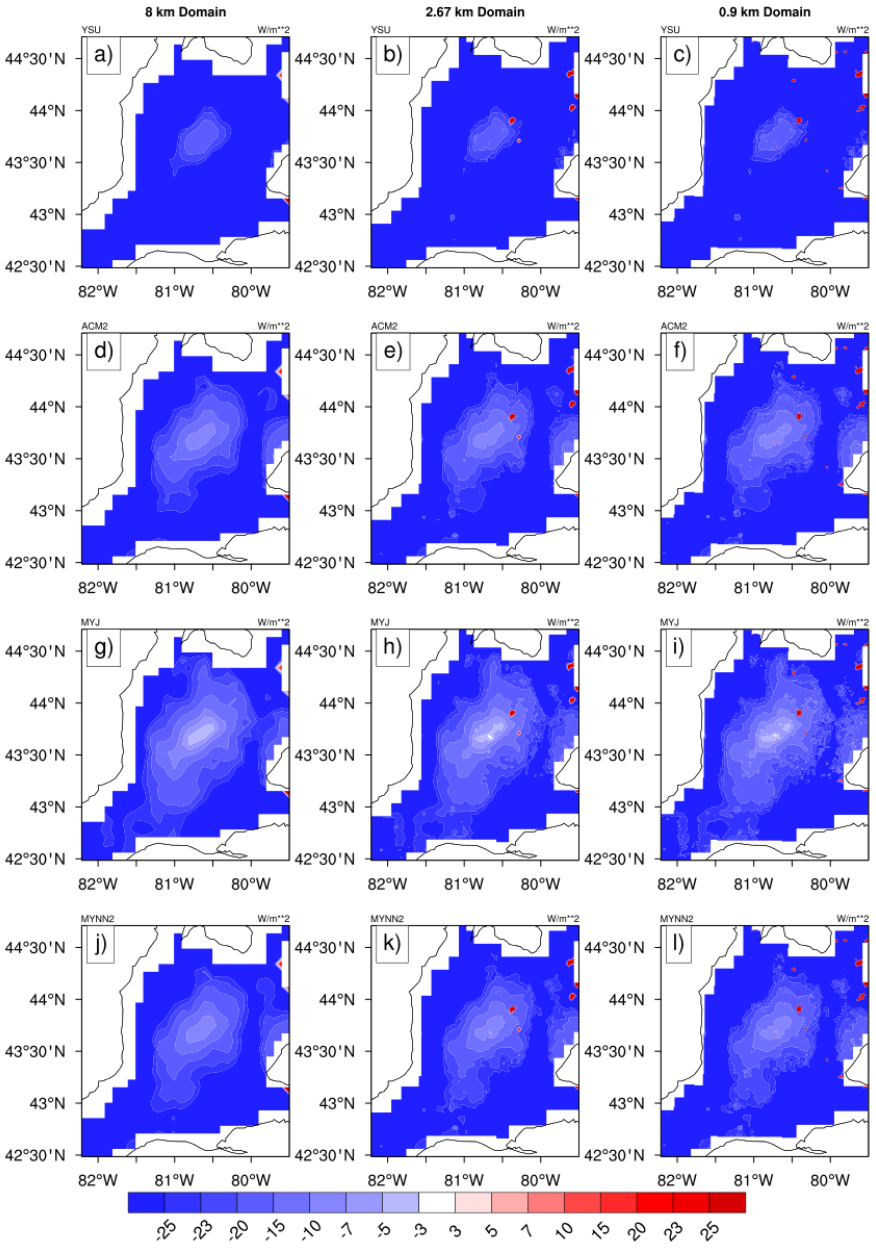

Figure 6.4: The same as Figure 6.2 but for SHF.

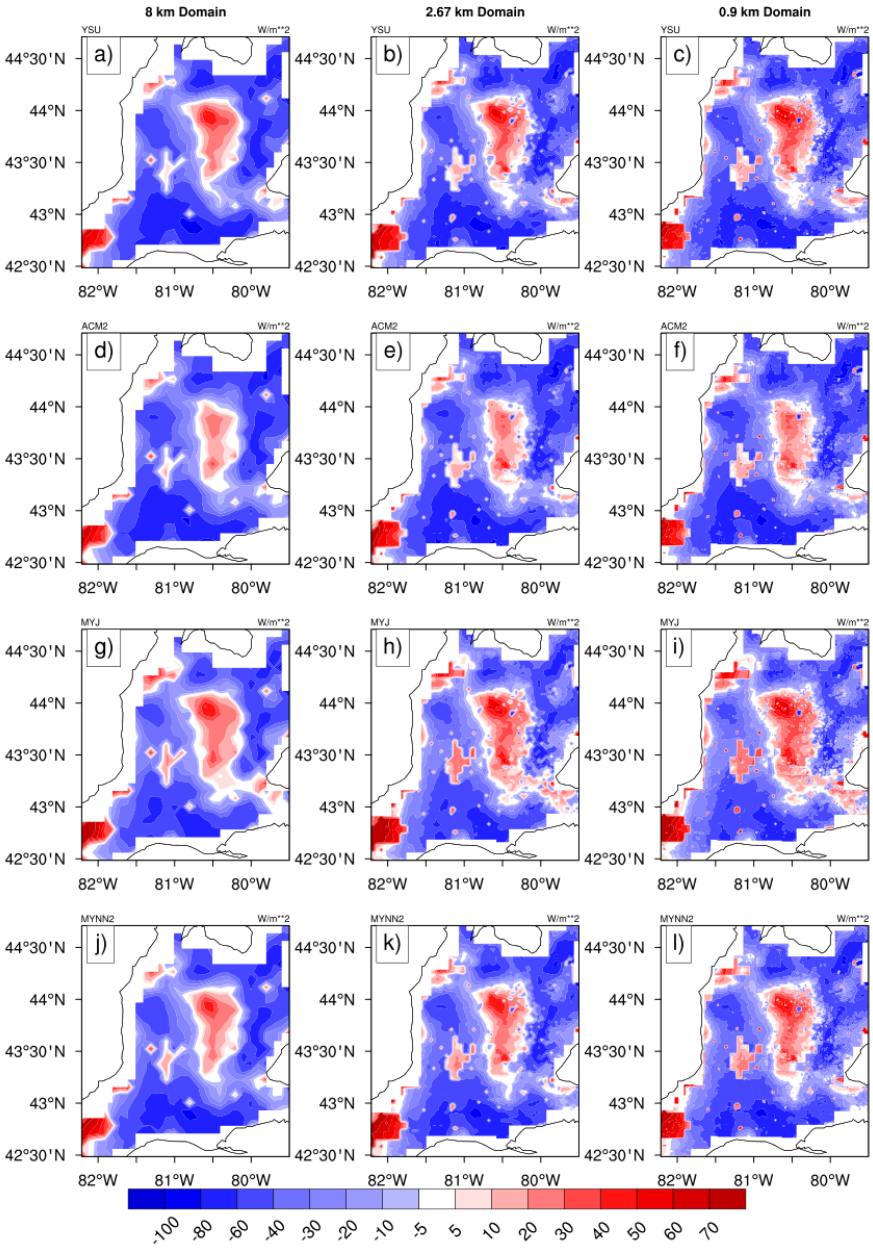

Figure 6.5: The same as Figure 6.3 but for SHF.

The GHF, the smallest but not negligible component of the energy budget equation (1.3), is measured at the top of the soil and directed into the ground. The WRF-simulated

GHF shows large overestimation compared to EC-observed data (figure not shown here). For the spatial distribution of GHF, the model shows overestimation in January and underestimation in July over the whole domain. Overall, WRF performed poorly while simulating GHF. It is to be noted that GHF contributes less to the net surface energy balances.

6.2.3 Surface Energy Flux Sensitivity to Annual Climatological Atmospheric Conditions

To test the sensitivity of different surface energy flux components to large-scale atmospheric conditions, two year-long simulations, for 2014 and 2015, were performed. We compared WRF simulations against three NLDAS-2 gridded analyses generated using the VIC, Noah, and MOSAIC LSMs in the absence of an entirely observed gridded energy flux data set. The LSMs were developed independently by three research groups; therefore, this study meets the model-evaluation criteria recommended by Pielke Sr. (2002) [80].

We observed a strong sensitivity to large-scale atmospheric conditions for simulated LHF. WRF shows widespread overestimation of LHF in January, 2002, as shown in Figure 6.6 (top row). In contrast, in January 2015, the model underestimated LHF over a large portion of southern Ontario, but showed very little to no bias elsewhere (Figure 6.6, bottom row). We noticed a change in values of LHF bias across the domain in January 2015 for the three LSMs. For example, when MOSAIC LSM is compared with Noah LSM, WRF underestimated not only over southern Ontario but also over the north-east corner of the domain (Figure 6.7, bottom row). WRF-simulated LHF showed large underestimation at the lee side of Lake Huron compared to the Noah and MOSAIC LSMs (Figure 6.6 and 6.7, bottom row). It can be seen in Figure 6.8 (bottom row) that WRF showed very low bias to the most sophisticated VIC LSM analysis, except for a small overestimation over the Appalachian mountains portion of the domain. It is also evident from all three figures that WRF underestimated LHF at the interface between the water on Lake Huron's southern Ontario side and the surrounding land areas, popularly known as snow belt regions. WRF showed a systematic underestimation of LHF for the entire winter season, as illustrated in Figure 6.9. Accordingly, the spatial distribution of WRF-simulated SHF bias (figures not shown here) in different winter months for years 2002, 2014, and 2015 for the three LSMs demonstrates a behavior that complements the LHF bias (i.e., in regions of underestimated LHF, it overestimated SHF). A positive SHF bias starts disappearing as the 2014 winter season progresses; eventually, WRF shows a negative SHF as spring begins.

Moreover, in January, WRF shows an unusually high energy flux bias both for SHF and

LHF over the smaller, shallower northern lakes (especially in the north-eastern corner of the domain) for all three LSMs (Figure 6.6-6.8), and the magnitude of LHF bias decreases in the later winter months.

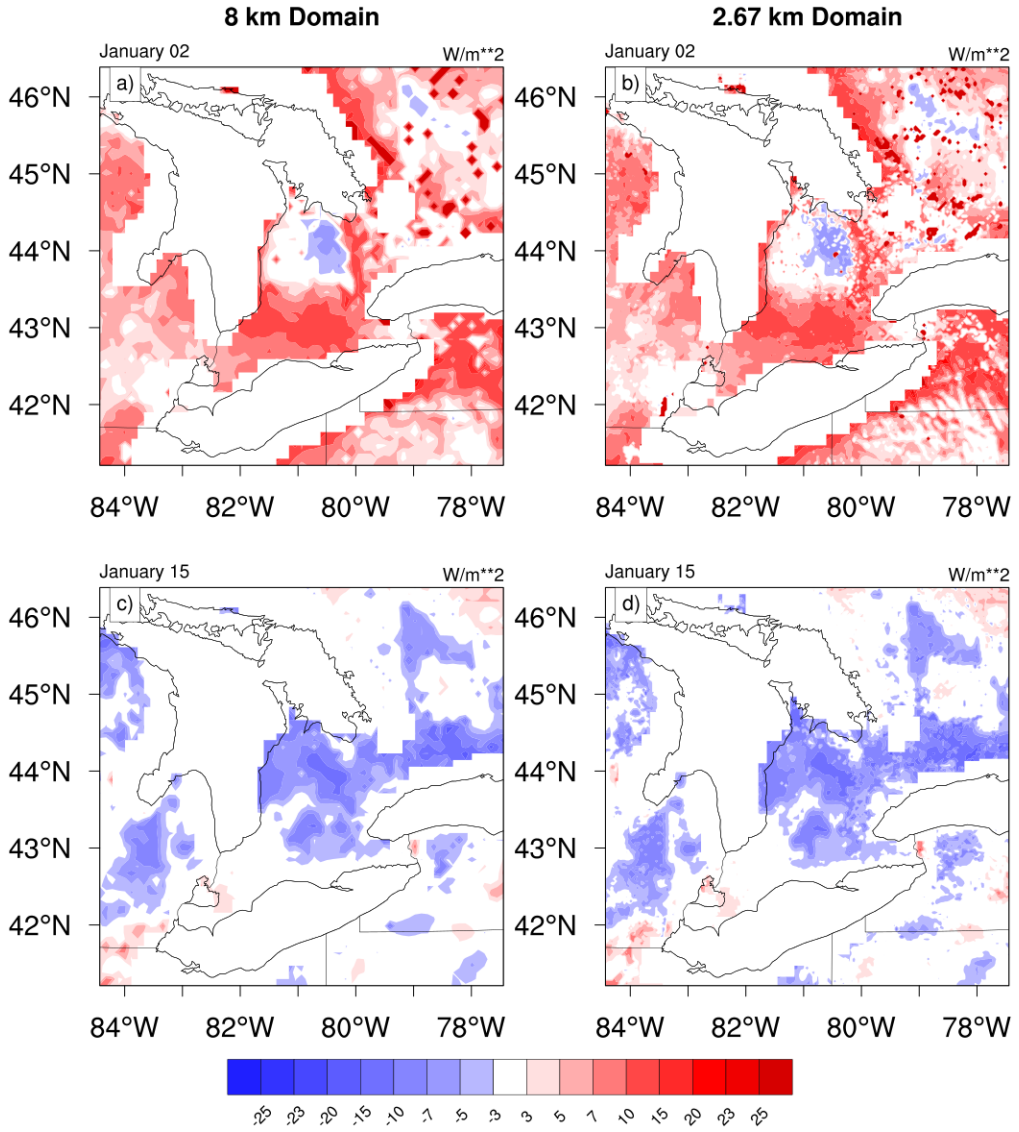

Figure 6.6: Bias in mean LHF bias relative to NLDAS-Noah LSM analysis in January of 2002 (top row) and 2015 (bottom row); for the outermost domain (left column), intermediate domain (right column). The NLDAS-2 data are in 1/8th-degree grid spacing and interpolated to match WRF model grid spacing.

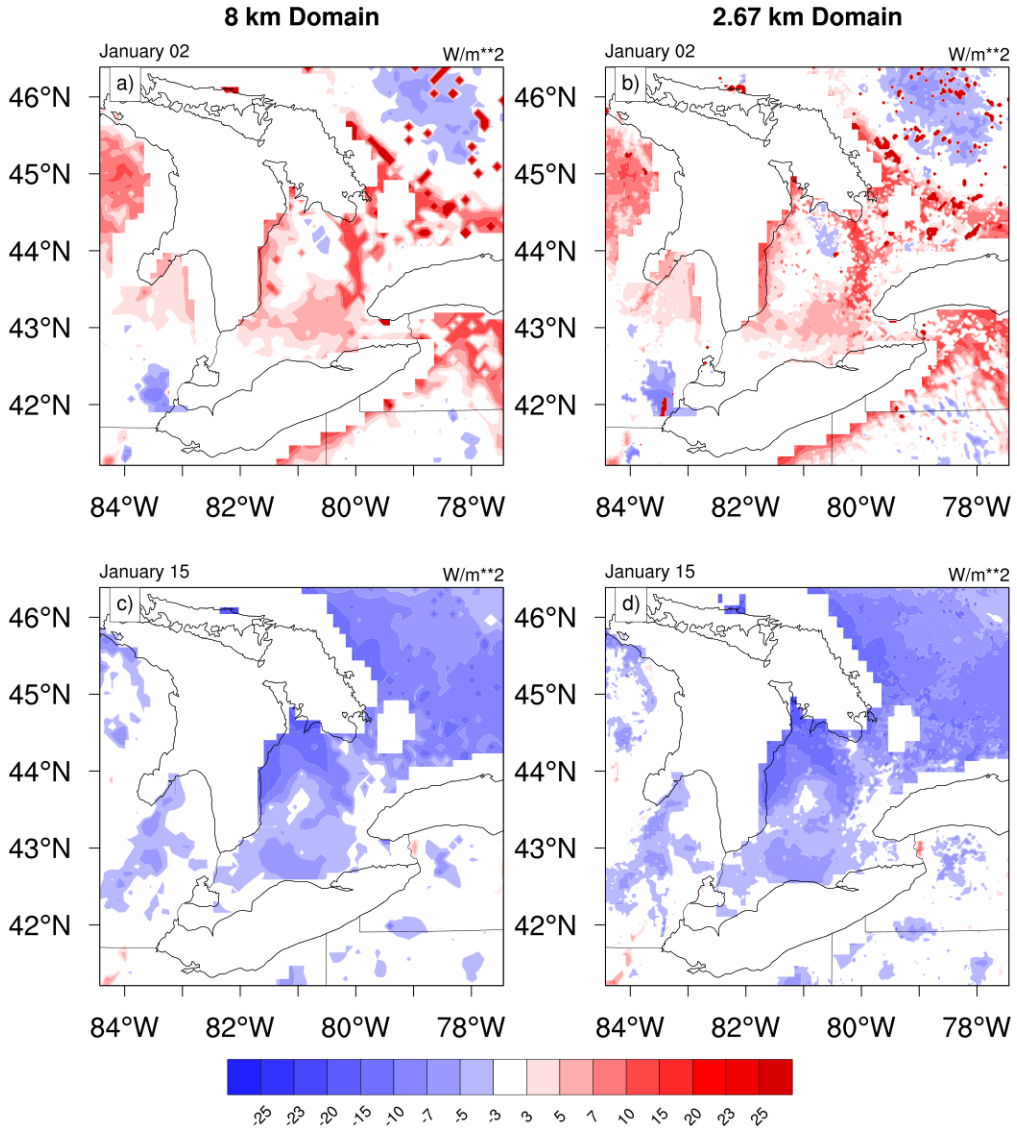

Figure 6.7: The same as Figure 6.6 but for the MOSAIC LSM.

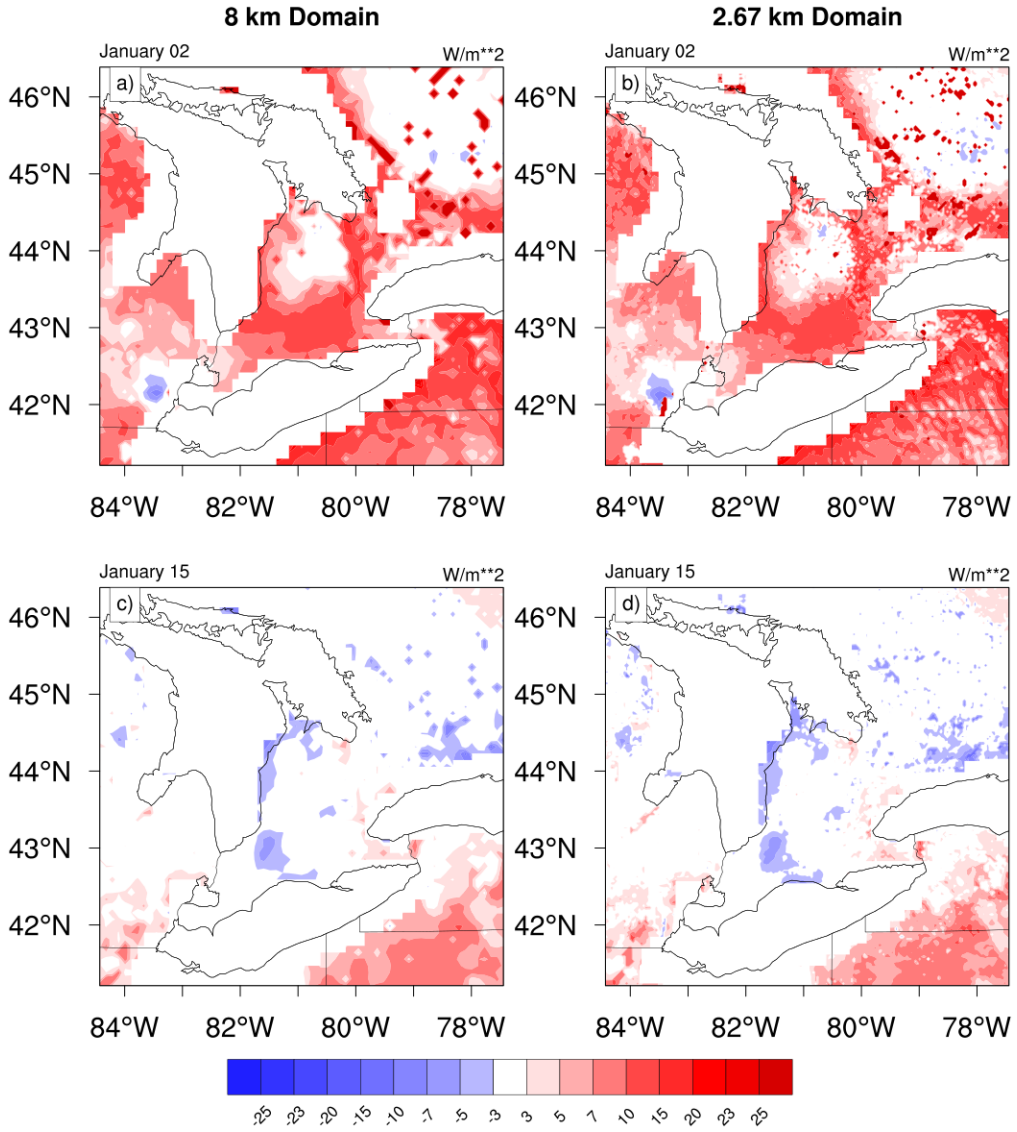

Figure 6.8: The same as Figure 6.6 but for the VIC LSM.

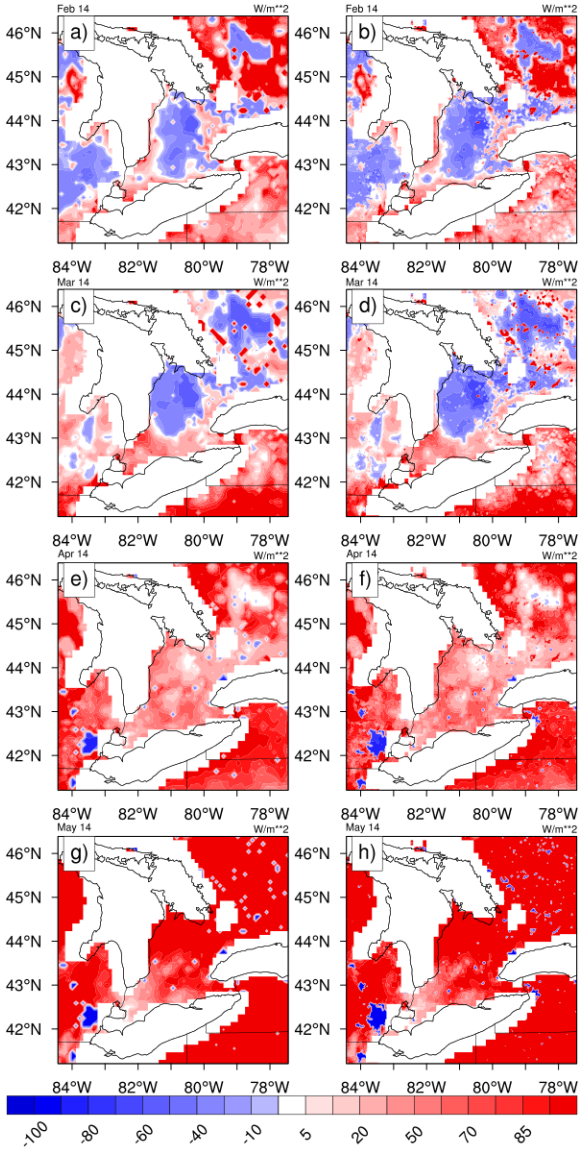

Figure 6.9: The same as Figure 6.6 but for February-May, 2014.

6.3 Discussion

This research has examined the sensitivity of WRF-simulated SHF, LHF, and GHF to different PBL parameterization schemes and annual climatic conditions of the input at-

mospheric initial and boundary conditions over the Great Lakes region. In contrary to Steeneveld *et al.* (2011) [91] study, who used Cabauw tower (Netherlands) observations, the current WRF simulations successfully reproduces the diurnal variability of the SHF, but showed a systematic overestimation of the diurnal variability of LHF compared to EC tower measurement. It should be noted that we used the U.S. Geological Survey (USGS) 24 classification categories of land use data derived from 1-km advanced very high resolution radiometer (AVHRR) 10-day normalized difference vegetation index (NDVI) composites measured over a 12-month period (April 1992-March 1993). Therefore, in our experiment (WRF simulations for 2007 and 2008), a large overestimation of LHF bias may result from inaccurate land-use and land-cover characteristics. It is worth noting that the Cabauw tower (Netherlands) is sorrunded by open pasture where as the Strawberry Creek EC tower was over a corn field. Overall, both of the study found that SHF and LHF modeled by WRF are larger than EC observations.

According to the surface energy balance equation (1.3), the sum of LHF and SHF should equal the net radiation minus the GHF. However, we obtained an energy balance closure of 0.7 at the Strawberry Creek EC measurement site for 2007 and 2008. It is to be noted that we ignored the contributions of biochemical energy and heat storage parameters in the surface energy balance equation (1.3) when calculating the energy balance closure at Strawberry Creek EC station, as they are typically small. Yates *et al.* (2001) [108] reported an energy flux bias uncertainty of $\sim 50\ Wm^2$ based on a cooperative atmosphere-surface exchange study field experiment (CASE-97) in the Walnut River watershed, Kansas, USA. The authors observed an almost double increase in the standard deviation of peak LHF when they included cloudy days in their analysis. In our study, the model-simulated diurnal biases were found to be 10 to 30 Wm^{-2} and 50 to 200 Wm^{-2} for SHF and LHF, respectively, and are within an acceptable range of Yates *et al.* (2001) [108]. Obviously, such a difference in energy flux bias is expected to influence the evolution of ABL structure.

It is obvious that all PBL schemes show a systematic bias persistently for all surface energy flux components downstream of the Blue Mountain area and surrounding high elevation regions. The bias was largest in the year and month when the temperature difference between the lake water surface and the atmosphere above the water surface was maximum. Our results indicate that all PBL schemes studied possess limitations in properly representing boundary layer processes in the immediate vicinity of large water bodies followed by steep topography. This finding suggests that further improvement of these PBL schemes is needed.

The spatial distributions of simulated LHF patterns are in good agreement with NLDAS-2 model analysis for January 2002, but they are systematically underestimated for July 2002. We observed a noticeable difference in LHF bias over the Niagara Escarpment belt,

an area of significant landscape heterogeneity, which causes energy flux gradients because of the differences in albedo and roughness length. Landscape heterogeneity greatly affects the evolution of eddies in the convective boundary layer, which ultimately influences the partitioning of energy flux components (Avissar and Schmidt, 1998 [4]; Pielke *et al.*, 1997 [79]). Several studies have also reported the importance of proper representation of land use and vegetation properties in simulating SHF and LHF (LeMone *et al.*, 2007 [52]; Weckwerth *et al.*, 2004 [106]; and LeMone *et al.*, 2006 [53]). Model-simulated energy flux biases decreased significantly when high-resolution remote-sensing LULCC data and near real-time land-surface properties were incorporated Miller *et al.* (2006) [64].

We found the maximum LHF and SHF biases over green vegetation and sparsely populated land surfaces, respectively. The horizontal variability of SHF and LHF biases demonstrates the role of land surface characteristics in the partitioning of incoming solar radiation at Earth's surface. Overall, the WRF model showed positive bias for SHF and negative bias for LHF in the interior of the innermost domain. We hypothesize that biases in the initial soil moisture data are a possible source of error. In addition, insufficient model spin-up time (in our case a maximum of one month) can be another source of error. To test our hypothesis, it is required to run WRF simulations for high temporal resolution, and high resolution soil moisture and soil texture data; however, doing so is beyond the scope of the present study.

We also identified large energy flux biases over the smaller northern lakes. There are several possible explanations for this result, the most likely being the incorrect representation of lake surface temperatures. Since northern geography is dominated by smaller lakes, proper representation of their water temperatures is required to reproduce observed atmospheric conditions. Excessive fluxes from these smaller lakes can significantly alter the stability of the overlying atmospheric boundary layer and other components of the model solver. We know that boundary layer structure plays an important role in the initiation of convection and successive model precipitation.

6.4 Conclusion

We demonstrate that it is very important for RCM users to assess a model's capability to reproduce major surface energy flux components along with temperature and precipitation, the two most commonly used meteorological variables in evaluating a model's performance. When compared with EC tower measurement, WRF reproduced the diurnal variability of the SHF very well, but systematically overestimated LHF for the months of June 2007 and 2008. Model-simulated energy fluxes showed a lower sensitivity to the choice of PBL

parameterization schemes. WRF model simulations were also found to be sensitive to the climatology of the driving boundary conditions. For example, if the WRF model is forced with distinctively different annual climatological boundary conditions, such as extremely cold in January 2014 and below average temperature in January 2015, simulated spatial distribution of energy flux bias clearly indicates different behavior than that found through NLDAS analysis. Thus, the WRF's credibility when evaluated on the basis of only one seasonal statistic may provide misleading information about the model's performance. We also found large energy flux biases over the smaller northern lakes. This can propagate into other model solvers and deteriorate model solutions due to the nonlinear nature of atmospheric systems. Our energy flux sensitivity study has demonstrated that southern Ontario is an ideal place to study complex intersections of land, atmosphere, and water bodies.

Chapter 7

Discussions

Numerical weather prediction (NWP) models are powerful mathematical systems that allow us to simulate and understand complex weather and climate processes. NWP models like WRF generate internal variability (IV) due to nonlinear interactions among various components of model physics and dynamics. IV is an intrinsic part of the climate system and can modulate or mask the impacts of external forcing from model solutions. The study carries out WRF simulations with four cumulus cloud (CU), five cloud microphysics (MP), and four planetary boundary layer (PBL) parameterization schemes; five different years with significantly different climatological atmospheric conditions; and two seasons: winter and summer. It explores multiple meteorological variables, including total precipitation (convective + non-convective); daily temperature; and major surface energy flux components (i.e., sensible heat flux and latent heat flux). Particular attention is paid to analyzing precipitation and temperature variables.

Precipitation is a highly uncertain meteorological variable, dependent on topographic distribution, proximity to sea and lakes, and the latitude and longitude of study areas. In the WRF model, explored in this thesis, precipitation originates as a by-product of grid-scale processes (from the MP scheme) and sub-grid scale processes (from the convective parameterization scheme). WRF-simulated grid-scale precipitation was an order of magnitude higher than the sub-grid-scale precipitation in January. In January most of the simulated-precipitation over southern Ontario falls as snow, which originates due to microphysical processes and does not show sensitivity to the choice of CP scheme. However, during July, when precipitation falls as rain, it shows substantial variability to the choice of convective scheme. During July when convective activity dominates local precipitation over this part of the globe, the precipitation shows a dry bias over the Grand River watershed and a wet bias over the south-western and north-western corners of the domain.

There are several possible explanations for this bias; the most-probable is erroneous initial conditions of soil moisture, temperature, and texture.

Convective precipitation both in January and July shows a strong sensitivity to the cumulus parameterization scheme used and is dominated by orographic distribution. Monthly convective precipitation rates differ greatly among the four cumulus schemes; indeed, one can divide the four parameterization schemes into two groups. The KF and GD schemes generated too much convective precipitation and fall into the first group. In contrast, the NSAS and BMJ schemes produced comparatively lower convective precipitation and belong to the second group. WRF-simulated precipitation differences result because all four cumulus schemes parameterize the orographic influences independently. The study results are in agreement with Mooney *et al.* (2013) [69], who carried out WRF-model sensitivity experiments over Europe. The sensitivities of WRF-model CP schemes were tested by Collier (2007) [18] and Lin *et al.* (2008) [55], who reported substantial precipitation biases over North America in summer. WRF gives increased precipitation variability due to dynamical downscaling. It is hypothesized that rainfall distribution in the innermost nest increased because of more-realistic representation of land use and land cover classes over the domain.

Different values of CC in January and July indicate the different roles of PBL schemes in winter and summer months. Precipitation shows low sensitivity to the choice of PBL scheme in January, when the boundary layer becomes more stable because of dry and cold air, than in July, when it is less so because of warm and moist air. In summer months, the PBL scheme plays an important role in stabilizing the atmosphere, by transporting various surface fluxes, including heat, moisture, and momentum, from the lowest couple of meters of the Earth's surface to the upper atmosphere. Further, the PBL scheme directly influences summer precipitation by transporting necessary energy up to the LCL to initiate convection. The PBL schemes differ in their vertical mixing capacities, resulting in different amounts of moisture being transported to higher model levels. Excessive moisture and latent heat in the lower to middle atmosphere ultimately produced too much low and mid-level cloud, and finally, grid-scale precipitation, with the MP scheme. Both observation and model simulation confirmed concentrated snowfall in organized bands, especially downwind of each lake. The differences in monthly accumulated precipitation totals clearly indicate the different roles of local and non-local PBL schemes in transporting surface fluxes in different seasons.

The performance of cloud microphysics schemes depend on various factors, including the type of hydrometeor species, annual climatological conditions, and Great Lakes ice-cover statistics. This research has also demonstrated that a strong relationship exists among microphysical processes, atmospheric dynamics, and thermodynamics. The results

are consistent with those of Liu *et al.* (2011) [57], who carried out WRF model cloud microphysics scheme sensitivity experiments simulating winter precipitation over the Colorado headwaters region.

Summing up the results from the physical parameterization sensitivity experiments, it is evident that simulated precipitation is influenced by all three physical parameterizations. Further, the current physical parameterization sensitivity experiments demonstrate that precipitation is more sensitive to cumulus cloud and microphysics schemes than the PBL scheme. More specifically, convective precipitation exhibits strong sensitivity to cumulus cloud parameterization schemes in July. On the other hand, grid-scale precipitation indicates more variability among microphysics schemes in January. Similarities among summer precipitation results exist between the present study and that by Jankov *et al.* (2007) [46], who examined the sensitivity of the WRF model's physical parameterization for warm season mesoscale convective system (MCS) rainfall over the south-central United States. Additionally, more-sophisticated microphysics parameterization schemes improved model performance only slightly, and certainly not to the degree that regional climate model users logically desire.

In summary, the greatest precipitation variability comes from changes in the choice of cumulus cloud parameterization scheme in July and the microphysics parameterization scheme in January. January precipitation shows slight sensitivity to PBL schemes as well. In July, all cumulus schemes show a warm bias in the interior of the domain where precipitation is underestimated. The explanation is that this warm bias may have originated from an underestimation of precipitation. A majority of the temperature bias is inherited from inadequate representation of soil moisture and soil texture data sets during model initialization. Another source of uncertainty could be the SW and LW radiation parameterization.

The order of interactions of the PBL physical processes among the various schemes also varies considerably, resulting in different structures for the boundary layer profile (Hu *et al.*, 2010 [40]). Along the shores of the Great Lakes, simulated temperatures showed an overall bias, clearly indicating that lake surface temperatures modulate the inland temperatures of southern Ontario through lake-breeze. Further, a relatively large temperature bias was found over large cities (i.e., Toronto, Mississauga and Hamilton) where the land-use and land-cover patterns are very complex. It is to be noted that this study used no urban canopy model (UCM) or building energy model (BEM) in its WRF simulations. A UCM takes into account surface effects for roofs, walls, and streets, whereas a BEM is a multi-layer UCM model that can better represent the properties of taller building, especially those that are higher than the lowest model levels. WRF experiments using UCM and BEM to identify these cities' roles in diurnal temperature cycles can add invaluable information.

Some of the biases in temperature could result from incorrect representation of SW and LW radiation processes. Surface-temperature forecasting is more dependent on proper parameterization of SW and LW radiation schemes than on convective parameterization.

Unlike the cumulus parameterization schemes, which show low sensitivity to temperature, PBL schemes show high sensitivity to atmospheric temperature.The temperature analysis results suggests that problems exist in all convective parameterization schemes tested. No single scheme outperforms the others while simulating all three temperatures. The findings of the PBL sensitivity study are in agreement with the findings of García-Díez *et al.* (2013) [29], who investigated the WRF model's PBL sensitivity over Europe.

Over the smaller northern lakes, the energy flux study noticed a large LHF bias, which may have resulted from incorrect representation of lake surface temperatures. Since northern geography is dominated by smaller lakes, proper representation of their water temperatures is required to reproduce observed atmospheric conditions. Excessive fluxes from these smaller lakes can significantly alter the stability of the overlying atmospheric boundary layer and other components of the model solver. The large LHF bias over the Niagara Escarpment belt can be attributed to landscape heterogeneity, which causes energy flux gradients because of the differences in albedo and roughness length. Insufficient model spin-up time (in our case a maximum of one month) can be another source of error in the case of SHF. The surface temperature is directly affected by LHF and SHF. In particular, the later significantly influences surface temperatures. It is well known that inaccurate initial soil moisture and texture data give SHF bias too.

The highest resolution simulation did not produced the best result compared to intermediate resolution grid, thus RCM users' are encouraged to validate the model climatology at those resolutions before running a climate simulation.

To the best of our knowledge, this is the first comprehensive sensitivity study that investigates the WRF model's credibility over the Great Lakes region, which is (1) surrounded by three of the largest lakes in the world, (2) has very large temperature differences between winter and summer months, (3) is underneath the Jet Stream path, and (4) is in a region over which frequent synoptic scale disturbances pass. In summer, Lake Breeze from Lakes Erie, Huron, and Ontario create a rare lower tropospheric environment over southern Ontario, which can be observed at very few other places on Earth.

In conclusion, surface energy flux sensitivity along with the WRF model's physical parameterizations (i.e., CU, PBL, and MP) offered a unique opportunity to test the WRF model's forecast credibility and a chance to verify the results published for other areas. This thesis has demonstrated that southern Ontario is a distinctive place in which to study complex intersections of land, atmosphere, and water bodies. The key findings of this thesis

are listed in the next chapter.

Chapter 8

Conclusions and Recommendations

8.1 Summary of Conclusions

The key findings of this thesis are grouped into two categories: generalized conclusions that are observed in all four studies and findings inherent to the individual studies.

8.1.1 General Conclusions

The following key findings were observed in all four studies

- Two-way feedback between the outermost domain and inner domain (nest) reduces WRF systematic bias (WRF-Observation);
- WRF shows a small increase in forecasting skill when the horizontal resolution is increased from 8 km to 2.67 km. Surprisingly, the model's forecast skill decreases when the horizontal resolution is increased from 2.67 km to 0.888km. Model simulations show hardly any sensitivity to dynamical downscaling, especially on the daily time scale;
- Simulated precipitation shows a systematic bias in July, on average, of -50 to +30 mm and in January, on average, of -10 to +30 mm;
- WRF-simulated temperatures showed good reproducing skill, as the biases are within the range of $\pm 1.0\,^{\circ}$ C in most parts of the domain;

- WRF-simulated precipitation and temperature agree well with DAYMET-gridded observations, with correlation coefficients of nearly 0.3 to 0.8 and >0.9, respectively.

8.1.2 Major Conclusions from Cumulus Cloud Parameterization Study

- Simulated precipitation shows lower variability in January, when the large-scale state provides strong forcing along the model boundaries, which later diffuses far inward of the model domain and prevents the model developing its own dynamics. On the other hand, simulated precipitation shows large variability in July because local forcing (e.g., deep convection) is strong and outperforms the external forcing present in the driving boundary conditions;

- WRF-simulated precipitation shows a significant dependence on CP, in particular KF and BMJ. The KF is found to be an overactive CP scheme, while BMJ is an under-active one;

- Precipitation shows more sensitivity to the selection of convective parameterization than temperature;

- The Model's forecasting skill exhibits strong seasonal dependence, low (high) temperature bias in summer (winter). No single scheme outperformed the others while simulating all three temperatures.

8.1.3 Major Conclusions from PBL Parameterization Sensitivity Study

- Surface temperature is more sensitive to PBL scheme;

- Accuracy of the model-simulated thermodynamic structures of the atmosphere depends on PBL scheme's ability to accurately simulate vertical wind components;

- PBL scheme's systematic errors depends on time of day and also on large-scale atmospheric conditions;

- The YSU scheme gives the most robust results.

8.1.4 Major Conclusions from Microphysics Parameterization Sensitivity Study

From the microphysics parameterization sensitivity study, the following key points can be highlighted:

- WRF-simulated precipitation shows more sensitivity to the choice of complex MP scheme in January when precipitation falls as snow. The most-sophisticated schemes, the THOM and M2M, took on average $15 \sim 25$ % more computing time, but did not produced the best forecast skill score;
- The WSM6 MP scheme shows the best overall performance while simulating surface precipitation totals both for January and July, with the best results for January;
- Extreme precipitation events are better captured by the WSM6 MP scheme;
- Model-simulated temperatures are not very sensitive to the choice of MP scheme;
- MP scheme performance depends on the type of hydrometeor species, annual climatological conditions, and Great Lakes ice cover statistics.

8.1.5 Major Conclusions from Energy Flux Sensitivity Study

- WRF-simulated LHF and SHF biases indicate sensitivity to climatological atmospheric initial conditions;
- Model-simulated surface energy flux sensitivity to PBL schemes depend on the Great Lakes ice cover statistics;
- WRF gives a large energy flux bias in January over the smaller shallow northern lakes;
- The Model shows a noticeable difference in LHF bias over the Niagara Escarpment belt, an area of significant landscape heterogeneity.

8.2 Recommendations for Future Research

From the beginning of the nineteenth century, Canadian agriculture has shifted to the prairies, and Ontario has witnessed agricultural land abandonment and commercial reforestation. The albedo of snow-covered cultivated land is higher than that for snow-covered forested landscape. Carbon sequestration through forestation/re-forestation is one of many popular techniques proposed to manage the current rate of global warming. However, Betts (2000) [9] simulated the impact of forestation in temperate and boreal forest areas and concluded that instead of mitigating the current rate of climate change, high-latitude forestation may amplify it due to snow-albedo feedback. Therefore, it is very important to investigate the impacts of historical land-use and land-cover conversion over Ontario, which has been undergoing periodic changes of its landscape from the beginning of European settlement.

In the future, the author plans to apply the WRF model's optimal physical parameterization combinations obtained in this current research and domain configurations to work on the following challenge:

- Modeling the impact of land-use/land-cover conversion on the regional climate of Southern Ontario, Canada;
- Surface temperature forecasts are more dependent on proper parameterization of SW and LW radiation schemes than on CU, PBL and MP. Therefore, sensitivity of SW and LW radiation are required for a robust understanding of the temperature bias;
- WRF simulations with high resolution soil moisture and soil texture data sets will be conducted to test our hypothesis about the persistent dry and warm bias over the Grand River watershed.

References

[1] RA Anthes. Estimating sensitivity and uncertainty in mesoscale numerical models. In *Proc. Int. Conf. Monsoon and Mesoscale Meteorology*, pages 1–8, 1986.

[2] Akio Arakawa and Wayne Howard Schubert. Interaction of a cumulus cloud ensemble with the large-scale environment, part i. *Journal of the Atmospheric Sciences*, 31(3):674–701, 1974.

[3] Salvi Asefi-Najafabady, Kevin Knupp, John R Mecikalski, and Ronald M Welch. Radar observations of mesoscale circulations induced by a small lake under varying synoptic-scale flows. *Journal of Geophysical Research: Atmospheres (1984–2012)*, 117(D1), 2012.

[4] Roni Avissar and Tatyana Schmidt. An evaluation of the scale at which ground-surface heat flux patchiness affects the convective boundary layer using large-eddy simulations. *Journal of the Atmospheric Sciences*, 55(16):2666–2689, 1998.

[5] Nauman K Awan, H Truhetz, and A Gobiet. Parameterization-induced error characteristics of mm5 and wrf operated in climate mode over the alpine region: An ensemble-based analysis. *Journal of Climate*, 24(12):3107–3123, 2011.

[6] P Bechtold, E Bazile, F Guichard, P Mascart, and E Richard. A mass-flux convection scheme for regional and global models. *Quarterly Journal of the Royal Meteorological Society*, 127(573):869–886, 2001.

[7] AK Betts and MJ Miller. A new convective adjustment scheme. part ii: Single column tests using gate wave, bomex, atex and arctic air-mass data sets. *Quarterly Journal of the Royal Meteorological Society*, 112(473):693–709, 1986.

[8] Alan K Betts. A new convective adjustment scheme. part i: Observational and theoretical basis. *Quarterly Journal of the Royal Meteorological Society*, 112(473):677–691, 1986.

[9] Richard A Betts. Offset of the potential carbon sink from boreal forestation by decreases in surface albedo. *Nature*, 408(6809):187–190, 2000.

[10] Rafael Borge, Vassil Alexandrov, Juan José Del Vas, Julio Lumbreras, and Encarnacion Rodriguez. A comprehensive sensitivity analysis of the wrf model for air quality applications over the iberian peninsula. *Atmospheric Environment*, 42(37):8560–8574, 2008.

[11] L Bounoua, R. DeFries, G James Collatz, P Sellers, and H Khan. Effects of land cover conversion on surface climate. *Climatic Change*, 52(1):29–64, 2002.

[12] David R Bright and Steven L Mullen. The sensitivity of the numerical simulation of the southwest monsoon boundary layer to the choice of pbl turbulence parameterization in mm5. *Weather and Forecasting*, 17(1):99–114, 2002.

[13] AR Brown. Evaluation of parametrization schemes for the convective boundary layer using large-eddy simulation results. *Boundary-Layer Meteorology*, 81(2):167–200, 1996.

[14] AR Brown. Large-eddy simulation and parametrization of the baroclinic boundary-layer. *Quarterly Journal of the Royal Meteorological Society*, 122(536):1779–1798, 1996.

[15] AR Brown, ACM Beljaars, and H Hersbach. Errors in parametrizations of convective boundary-layer turbulent momentum mixing. *Quarterly Journal of the Royal Meteorological Society*, 132(619):1859–1876, 2006.

[16] Melissa S Bukovsky and David J Karoly. Precipitation simulations using wrf as a nested regional climate model. *Journal of Applied Meteorology & Climatology*, 48(10), 2009.

[17] Daniel R Cayan. Latent and sensible heat flux anomalies over the northern oceans: Driving the sea surface temperature. *Journal of Physical Oceanography*, 22(8):859–881, 1992.

[18] J Craig Collier and Guang J Zhang. Effects of increased horizontal resolution on simulation of the north american monsoon in the ncar cam3: An evaluation based on surface, satellite, and reanalysis data. *Journal of Climate*, 20(9), 2007.

[19] Jason M Cordeira and Neil F Laird. The influence of ice cover on two lake-effect snow events over lake erie. *Monthly Weather Review*, 136(7):2747–2763, 2008.

[20] Jimy Dudhia. Numerical study of convection observed during the winter monsoon experiment using a mesoscale two-dimensional model. *Journal of the Atmospheric Sciences*, 46(20):3077–3107, 1989.

[21] Fabian Eder, Frederik De Roo, Katrin Kohnert, Raymond L Desjardins, Hans Peter Schmid, and Matthias Mauder. Evaluation of two energy balance closure parametrizations. *Boundary-layer meteorology*, 151(2):195–219, 2014.

[22] GA Efstathiou, NM Zoumakis, D Melas, CJ Lolis, and P Kassomenos. Sensitivity of wrf to boundary layer parameterizations in simulating a heavy rainfall event using different microphysical schemes. effect on large-scale processes. *Atmospheric Research*, 132:125–143, 2013.

[23] MB Ek, KE Mitchell, Y Lin, E Rogers, P Grunmann, V Koren, G Gayno, and JD Tarpley. Implementation of noah land surface model advances in the national centers for environmental prediction operational mesoscale eta model. *Journal of Geophysical Research: Atmospheres (1984–2012)*, 108(D22), 2003.

[24] Elfatih AB Eltahir. A soil moisture–rainfall feedback mechanism: 1. theory and observations. *Water Resources Research*, 34(4):765–776, 1998.

[25] Jason P Evans, Marie Ekström, and Fei Ji. Evaluating the performance of a wrf physics ensemble over south-east australia. *Climate Dynamics*, 39(6):1241–1258, 2012.

[26] Eva Falge, Dennis Baldocchi, Richard Olson, Peter Anthoni, Marc Aubinet, Christian Bernhofer, George Burba, Reinhart Ceulemans, Robert Clement, Han Dolman, et al. Gap filling strategies for defensible annual sums of net ecosystem exchange. *Agricultural and forest meteorology*, 107(1):43–69, 2001.

[27] JM Fritsch and CF Chappell. Numerical prediction of convectively driven mesoscale pressure systems. part i: Convective parameterization. *Journal of the Atmospheric Sciences*, 37(8):1722–1733, 1980.

[28] Yoshinori Furukawa and John S Wettlaufer. Snow and ice crystals. *Physics Today*, 60(12):70–71, 2007.

[29] M García-Díez, J Fernández, L Fita, and C Yagüe. Seasonal dependence of wrf model biases and sensitivity to pbl schemes over europe. *Quarterly Journal of the Royal Meteorological Society*, 139(671):501–514, 2013.

[30] James B Gilmore, Jason P Evans, Steven C Sherwood, Marie Ekström, and Fei Ji. Extreme precipitation in wrf during the newcastle east coast low of 2007. *Theoretical and Applied Climatology*, pages 1–19, 2015.

[31] Georg A Grell and Dezső Dévényi. A generalized approach to parameterizing convection combining ensemble and data assimilation techniques. *Geophysical Research Letters*, 29(14):38–1, 2002.

[32] Jonathan Gula and W Richard Peltier. Dynamical downscaling over the great lakes basin of north america using the wrf regional climate model: The impact of the great lakes system on regional greenhouse warming. *Journal of Climate*, 25(21):7723–7742, 2012.

[33] Madhuparna Halder, Anupam Hazra, P Mukhopadhyay, and Devendraa Siingh. Effect of the better representation of the cloud ice-nucleation in wrf microphysics schemes: A case study of a severe storm in india. *Atmospheric Research*, 154:155–174, 2015.

[34] Jongil Han and Hua-Lu Pan. Revision of convection and vertical diffusion schemes in the ncep global forecast system. *Weather & Forecasting*, 26(4), 2011.

[35] Teddy Holt and Sethu Raman. A review and comparative evaluation of multilevel boundary layer parameterizations for first-order and turbulent kinetic energy closure schemes. *Reviews of geophysics*, 26(4):761–780, 1988.

[36] AAM Holtslag and BA Boville. Local versus nonlocal boundary-layer diffusion in a global climate model. *Journal of Climate*, 6(10):1825–1842, 1993.

[37] Song-You Hong and Jeong-Ock Jade Lim. The wrf single-moment 6-class microphysics scheme (wsm6). *J. Korean Meteor. Soc*, 42(2):129–151, 2006.

[38] Song-You Hong, Yign Noh, and Jimy Dudhia. A new vertical diffusion package with an explicit treatment of entrainment processes. *Monthly Weather Review*, 134(9), 2006.

[39] Song-You Hong, Kyo-Sun Sunny Lim, Ju-Hye Kim, Jeong-Ock Jade Lim, and Jimy Dudhia. Sensitivity study of cloud-resolving convective simulations with wrf using two bulk microphysical parameterizations: ice-phase microphysics versus sedimentation effects. *Journal of Applied Meteorology and Climatology*, 48(1):61–76, 2009.

[40] Xiao-Ming Hu, John W Nielsen-Gammon, and Fuqing Zhang. Evaluation of three planetary boundary layer schemes in the wrf model. *Journal of Applied Meteorology and Climatology*, 49(9):1831–1844, 2010.

[41] Mark Z Jacobson. *Fundamentals of atmospheric modeling*. Cambridge university press, 2005.

[42] Zaviša I Janjic. The step-mountain eta coordinate model: Further developments of the convection, viscous sublayer, and turbulence closure schemes. *Monthly Weather Review*, 122(5):927–945, 1994.

[43] Zaviša I Janjic. Comments on development and evaluation of a convection scheme for use in climate models. *Journal of the Atmospheric Sciences*, 57(21):3686–3686, 2000.

[44] Zaviša I Janjić. Nonsingular implementation of the mellor–yamada level 2.5 scheme in the ncep meso model. *NCEP office note*, 437:61, 2002.

[45] ZI Janjic. The surface layer parameterization in the ncep eta model. *World Meteorological Organization-Publications-WMO TD*, pages 4–16, 1996.

[46] Isidora Jankov, Paul J Schultz, Christopher J Anderson, and Steven E Koch. The impact of different physical parameterizations and their interactions on cold season qpf in the american river basin. *Journal of Hydrometeorology*, 8(5):1141–1151, 2007.

[47] John S Kain. The kain–fritsch convective parameterization: an update. *Journal of Applied Meteorology*, 43(1), 2004.

[48] A Khain, M Ovtchinnikov, M Pinsky, A Pokrovsky, and H Krugliak. Notes on the state-of-the-art numerical modeling of cloud microphysics. *Atmospheric Research*, 55(3):159–224, 2000.

[49] Randal D Koster and Max J Suarez. Modeling the land surface boundary in climate models as a composite of independent vegetation stands. *Journal of Geophysical Research: Atmospheres (1984–2012)*, 97(D3):2697–2715, 1992.

[50] O Krogsæter and J Reuder. Validation of boundary layer parameterization schemes in the weather research and forecasting model under the aspect of offshore wind energy applicationspart i: Average wind speed and wind shear. *Wind Energy*, 18(5):769–782, 2015.

[51] RRDE Laprise, R De Elia, D Caya, S Biner, PH Lucas-Picher, E Diaconescu, M Leduc, A Alexandru, L Separovic, et al. Challenging some tenets of regional climate modelling. *Meteorology and Atmospheric Physics*, 100(1-4):3–22, 2008.

[52] Margaret A LeMone, Fei Chen, Joseph G Alfieri, Mukul Tewari, Bart Geerts, Qun Miao, Robert L Grossman, and Richard L Coulter. Influence of land cover and soil moisture on the horizontal distribution of sensible and latent heat fluxes in southeast kansas during ihop_2002 and cases-97. *Journal of Hydrometeorology*, 8(1):68–87, 2007.

[53] Margaret A LeMone, Robert L Grossman, Richard L Coulter, Marvin L Wesley, Gerard E Klazura, Gregory S Poulos, William Blumen, Julie K Lundquist, Richard H Cuenca, Shaun F Kelly, et al. Land-atmosphere interaction research, early results, and opportunities in the walnut river watershed in southeast kansas: Cases and able. *Bulletin of the American Meteorological Society*, 81(4):757–779, 2000.

[54] Xetal Liang, Dennis P Lettenmaier, Eric F Wood, and Stephen J Burges. A simple hydrologically based model of land surface water and energy fluxes for general circulation models. *JOURNAL OF GEOPHYSICAL RESEARCH-ALL SERIES-*, 99:14–415, 1994.

[55] Jia-Lin Lin, Brian E Mapes, Klaus M Weickmann, George N Kiladis, Siegfried D Schubert, Max J Suarez, Julio T Bacmeister, and Myong-In Lee. North american monsoon and convectively coupled equatorial waves simulated by ipcc ar4 coupled gcms. *Journal of Climate*, 21(12), 2008.

[56] Yuh-Lang Lin, Richard D Farley, and Harold D Orville. Bulk parameterization of the snow field in a cloud model. *Journal of Climate and Applied Meteorology*, 22(6):1065–1092, 1983.

[57] Changhai Liu, Kyoko Ikeda, Gregory Thompson, Roy Rasmussen, and Jimy Dudhia. High-resolution simulations of wintertime precipitation in the colorado headwaters region: Sensitivity to physics parameterizations. *Monthly Weather Review*, 139(11):3533–3553, 2011.

[58] Syukuro Manabe, Joseph Smagorinsky, and Robert F Strickler. Simulated climatology of a general circulation model with a hydrologic cycle. *Mon. Wea. Rev*, 93(12):769–798, 1965.

[59] Michale McCumber, Wei-Kuo Tao, Joanne Simpson, Richard Penc, and Su-Tzai Soong. Comparison of ice-phase microphysical parameterization schemes using numerical simulations of tropical convection. *Journal of Applied Meteorology*, 30(7):985–1004, 1991.

[60] George L Mellor and Tetsuji Yamada. Development of a turbulence closure model for geophysical fluid problems. *Reviews of Geophysics*, 20(4):851–875, 1982.

[61] Fedor Mesinger, Geoff DiMego, Eugenia Kalnay, Kenneth Mitchell, Perry C Shafran, Wesley Ebisuzaki, Dušan Jovic, Jack Woollen, Eric Rogers, Ernesto H Berbery, et al. North american regional reanalysis. *Bulletin of the American Meteorological Society*, 87(3):343–360, 2006.

[62] JA Milbrandt and MK Yau. A multimoment bulk microphysics parameterization. part i: Analysis of the role of the spectral shape parameter. *Journal of the atmospheric sciences*, 62(9):3051–3064, 2005.

[63] JA Milbrandt and MK Yau. A multimoment bulk microphysics parameterization. part ii: A proposed three-moment closure and scheme description. *Journal of the atmospheric sciences*, 62(9):3065–3081, 2005.

[64] Jesse Miller, Michael Barlage, Xubin Zeng, Helin Wei, Kenneth Mitchell, and Dan Tarpley. Sensitivity of the ncep/noah land surface model to the modis green vegetation fraction data set. *Geophysical research letters*, 33(13), 2006.

[65] Kenneth E Mitchell, Dag Lohmann, Paul R Houser, Eric F Wood, John C Schaake, Alan Robock, Brian A Cosgrove, Justin Sheffield, Qingyun Duan, Lifeng Luo, et al. The multi-institution north american land data assimilation system (nldas): Utilizing multiple gcip products and partners in a continental distributed hydrological modeling system. *Journal of Geophysical Research: Atmospheres (1984–2012)*, 109(D7), 2004.

[66] Eli J Mlawer, Steven J Taubman, Patrick D Brown, Michael J Iacono, and Shepard A Clough. Radiative transfer for inhomogeneous atmospheres: Rrtm, a validated correlated-k model for the longwave. *Journal of Geophysical Research: Atmospheres*, 102(D14):16663–16682, 1997.

[67] Andrew L Molthan and Brian A Colle. Comparisons of single-and double-moment microphysics schemes in the simulation of a synoptic-scale snowfall event. *Monthly Weather Review*, 140(9):2982–3002, 2012.

[68] AS Monin and AMF Obukhov. Basic laws of turbulent mixing in the surface layer of the atmosphere. *Contrib. Geophys. Inst. Acad. Sci. USSR*, 151(163):e187, 1954.

[69] PA Mooney, FJ Mulligan, and Rowan Fealy. Evaluation of the sensitivity of the weather research and forecasting model to parameterization schemes for regional climates of europe over the period 1990-95. *Journal of Climate*, 26(3), 2013.

[70] H Morrison, G Thompson, and V Tatarskii. Impact of cloud microphysics on the development of trailing stratiform precipitation in a simulated squall line: Comparison of one-and two-moment schemes. *Monthly Weather Review*, 137(3):991–1007, 2009.

[71] Mikio Nakanishi and Hiroshi Niino. An improved mellor–yamada level-3 model: Its numerical stability and application to a regional prediction of advection fog. *Boundary-Layer Meteorology*, 119(2):397–407, 2006.

[72] Grigory Nikulin, Colin Jones, Filippo Giorgi, Ghassem Asrar, Matthias Büchner, Ruth Cerezo-Mota, Ole Bøssing Christensen, Michel Déqué, Jesus Fernandez, Andreas Hänsler, et al. Precipitation climatology in an ensemble of cordex-africa regional climate simulations. *Journal of Climate*, 25(18):6057–6078, 2012.

[73] HD Orville and RD Farley. Numerical modeling of clouds. *Lecture notes IFAORS Short Course*, 450:1–5, 1980.

[74] Jason Otkin, Hung-Lung Huang, and Axel Seifert. A comparison of microphysical schemes in the wrf model during a severe weather event. In *Papers delivered at 7th WRF Users Workshop, Boulder, CO, USA*, pages 19–22, 2006.

[75] Jason A Otkin and Thomas J Greenwald. Comparison of wrf model-simulated and modis-derived cloud data. *Monthly Weather Review*, 136(6):1957–1970, 2008.

[76] HL Pan and Wan-Shu Wu. Implementing a mass flux convection parameterization package for the nmc medium-range forecast model. *NMC office note*, 409(40):20–233, 1995.

[77] SE Perkins, AJ Pitman, NJ Holbrook, and J McAneney. Evaluation of the ar4 climate models' simulated daily maximum temperature, minimum temperature, and precipitation over australia using probability density functions. *Journal of climate*, 20(17):4356–4376, 2007.

[78] RM Petrone, P Chahil, ML Macrae, and MC English. Spatial variability of co_2 exchange for riparian and open grasslands within a first-order agricultural basin in southern ontario. *Agriculture, Ecosystems & Environment*, 125(1):137–147, 2008.

[79] RA Pielke, TJ Lee, JH Copeland, JL Eastman, CL Ziegler, and CA Finley. Use of usgs-provided data to improve weatherand climate simulations. *Ecological Applications*, 7(1):3–21, 1997.

[80] Roger A Pielke. *Mesoscale meteorological modeling*. Academic press, 2002.

[81] Jonathan E Pleim. A combined local and nonlocal closure model for the atmospheric boundary layer. part i: Model description and testing. *Journal of Applied Meteorology & Climatology*, 46(9), 2007.

[82] Jonathan E Pleim. A combined local and nonlocal closure model for the atmospheric boundary layer. part ii: Application and evaluation in a mesoscale meteorological model. *Journal of Applied Meteorology & Climatology*, 46(9), 2007.

[83] Jonathan E Pleim and Julius S Chang. A non-local closure model for vertical mixing in the convective boundary layer. *Atmospheric Environment. Part A. General Topics*, 26(6):965–981, 1992.

[84] CHB Priestley and RJ Taylor. On the assessment of surface heat flux and evaporation using large-scale parameters. *Monthly weather review*, 100(2):81–92, 1972.

[85] M Rajeevan, A Kesarkar, SB Thampi, TN Rao, B Radhakrishna, and M Rajasekhar. Sensitivity of wrf cloud microphysics to simulations of a severe thunderstorm event over southeast india. In *Annales Geophysicae*, volume 28, pages 603–619. European Geosciences Union, 2010.

[86] Satyaban B Ratna, JV Ratnam, SK Behera, T Ndarana, K Takahashi, T Yamagata, et al. Performance assessment of three convective parameterization schemes in wrf for downscaling summer rainfall over south africa. *Climate Dynamics*, pages 1–23, 2013.

[87] Eric Rogers, Thomas Black, Brad Ferrier, Ying Lin, David Parrish, and Geoffrey DiMego. Changes to the ncep meso eta analysis and forecast system: Increase in resolution, new cloud microphysics, modified precipitation assimilation, modified 3dvar analysis. *NWS Technical Procedures Bulletin*, 488:15, 2001.

[88] Juan J Ruiz, Celeste Saulo, and Julia Nogués-Paegle. Wrf model sensitivity to choice of parameterization over south america: validation against surface variables. *Monthly Weather Review*, 138(8):3342–3355, 2010.

[89] Shaohua Shen and Monique Y Leclerc. How large must surface inhomogeneities be before they influence the convective boundary layer structure? a case study. *Quarterly Journal of the Royal Meteorological Society*, 121(526):1209–1228, 1995.

[90] WC Skamarock, JB Klemp, J Dudhia, DO Gill, and DM Barker. Coauthors, 2008: A description of the advanced research wrf version 3. *NCAR Tech. Note NCAR/TN-475+ STR*, 113, 2005.

[91] GJ Steeneveld, LF Tolk, AF Moene, OK Hartogensis, W Peters, and AAM Holtslag. Confronting the wrf and rams mesoscale models with innovative observations in the netherlands: evaluating the boundary layer heat budget. *Journal of Geophysical Research: Atmospheres*, 116(D23), 2011.

[92] Roland B. Stull. Transilient turbulence theory. part i: The concept of eddy-mixing across finite distances. *Journal of the Atmospheric Sciences*, 41(23):3351–3367, 1984.

[93] Roland B Stull. *An introduction to boundary layer meteorology*, volume 13. Springer Science & Business Media, 1988.

[94] Karl E Taylor. Summarizing multiple aspects of model performance in a single diagram. *Journal of Geophysical Research: Atmospheres (1984–2012)*, 106(D7):7183–7192, 2001.

[95] NE Theeuwes, GJ Steeneveld, F Krikken, and AAM Holtslag. Mesoscale modeling of lake effect snow over lake erie–sensitivity to convection, microphysics and the water temperature. *Advances in Science and Research*, 4(1):15–22, 2010.

[96] Jean Thiébaux, Eric Rogers, Wanqiu Wang, and Bert Katz. A new high-resolution blended real-time global sea surface temperature analysis. *Bulletin of the American Meteorological Society*, 84(5):645–656, 2003.

[97] Gregory Thompson, Paul R Field, Roy M Rasmussen, and William D Hall. Explicit forecasts of winter precipitation using an improved bulk microphysics scheme. part ii: Implementation of a new snow parameterization. *Monthly Weather Review*, 136(12):5095–5115, 2008.

[98] PE Thornton, MM Thornton, BW Mayer, N Wilhelmi, Y Wei, and RB Cook. Daymet: Daily surface weather on a 1 km grid for north america. 1980–2008. *Oak Ridge National Laboratory Distributed Active Archive Center, Oak Ridge, T, N. doi*, 10, 2012.

[99] Peter E Thornton, Steven W Running, and Michael A White. Generating surfaces of daily meteorological variables over large regions of complex terrain. *Journal of Hydrology*, 190(3-4):214–251, 1997.

[100] P Thunis and R Bornstein. Hierarchy of mesoscale flow assumptions and equations. *Journal of the atmospheric sciences*, 53(3):380–397, 1996.

[101] SB Trier, MA LeMone, F Chen, and KW Manning. Effects of surface heat and moisture exchange on arw-wrf warm-season precipitation forecasts over the central united states. *Weather and Forecasting*, 26(1):3–25, 2011.

[102] IB Troen and L Mahrt. A simple model of the atmospheric boundary layer; sensitivity to surface evaporation. *Boundary-Layer Meteorology*, 37(1-2):129–148, 1986.

[103] Taneil Uttal, Judith A Curry, Miles G Mcphee, Donald K Perovich, Richard E Moritz, James A Maslanik, Peter S Guest, Harry L Stern, James A Moore, Rene Turenne, et al. Surface heat budget of the arctic ocean. *Bulletin of the American Meteorological Society*, 83(2):255–275, 2002.

[104] Wei Wang and Nelson L Seaman. A comparison study of convective parameterization schemes in a mesoscale model. *Monthly Weather Review*, 125(2):252–278, 1997.

[105] Thomas T Warner, Ralph A Peterson, and Russell E Treadon. A tutorial on lateral boundary conditions as a basic and potentially serious limitation to regional numerical weather prediction. *Bulletin of the American Meteorological Society*, 78(11):2599, 1997.

[106] Tammy M Weckwerth, David B Parsons, Steven E Koch, James A Moore, et al. An overview of the international h2o project (ihop_2002) and some preliminary highlights. *Bulletin of the American Meteorological Society*, 85(2):253, 2004.

[107] Youlong Xia, Kenneth Mitchell, Michael Ek, Justin Sheffield, Brian Cosgrove, Eric Wood, Lifeng Luo, Charles Alonge, Helin Wei, Jesse Meng, et al. Continental-scale water and energy flux analysis and validation for the north american land data assimilation system project phase 2 (nldas-2): 1. intercomparison and application of model products. *Journal of Geophysical Research: Atmospheres (1984–2012)*, 117(D3), 2012.

[108] David N Yates, Fei Chen, Margaret A LeMone, Russell Qualls, Steven P Oncley, Robert L Grossman, and Edward A Brandes. A cooperative atmosphere-surface exchange study (cases) dataset for analyzing and parameterizing the effects of land

surface heterogeneity on area-averaged surface heat fluxes. *Journal of Applied Meteorology*, 40(5):921–937, 2001.

[109] Lin Zhao, Jiming Jin, Shih-Yu Wang, and Michael B Ek. Integration of remote-sensing data with wrf to improve lake-effect precipitation simulations over the great lakes region. *Journal of Geophysical Research: Atmospheres (1984–2012)*, 117(D9), 2012.

[110] S Zilitinkevich. Non-local turbulent transport: Pollution dispersion aspects of coherent structure of connective flows. *WIT Transactions on Ecology and the Environment*, 9, 1970.

[111] Michael A Zulauf and Steven K Krueger. Two-dimensional cloud-resolving modeling of the atmospheric effects of arctic leads based upon midwinter conditions at the surface heat budget of the arctic ocean ice camp. *Journal of Geophysical Research: Atmospheres (1984–2012)*, 108(D10), 2003.

APPENDIX

Appendix A

Convective Parameterization

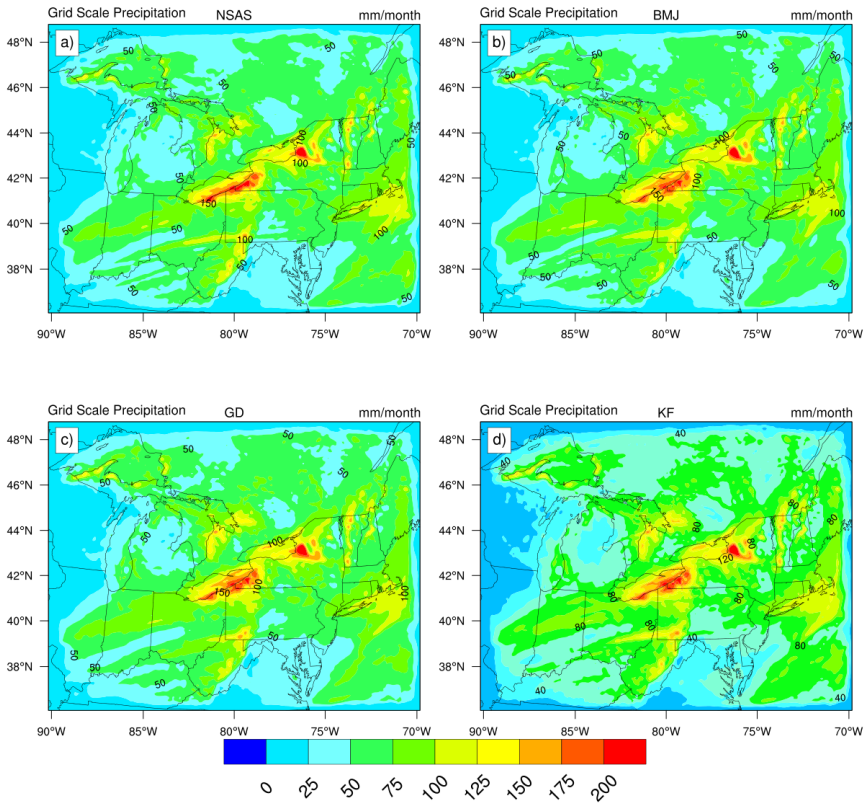

Figure A.0.1: The spatial distribution of monthly (January 2002) accumulated grid scale precipitation in mm generated by the WSM6 microphysics scheme.

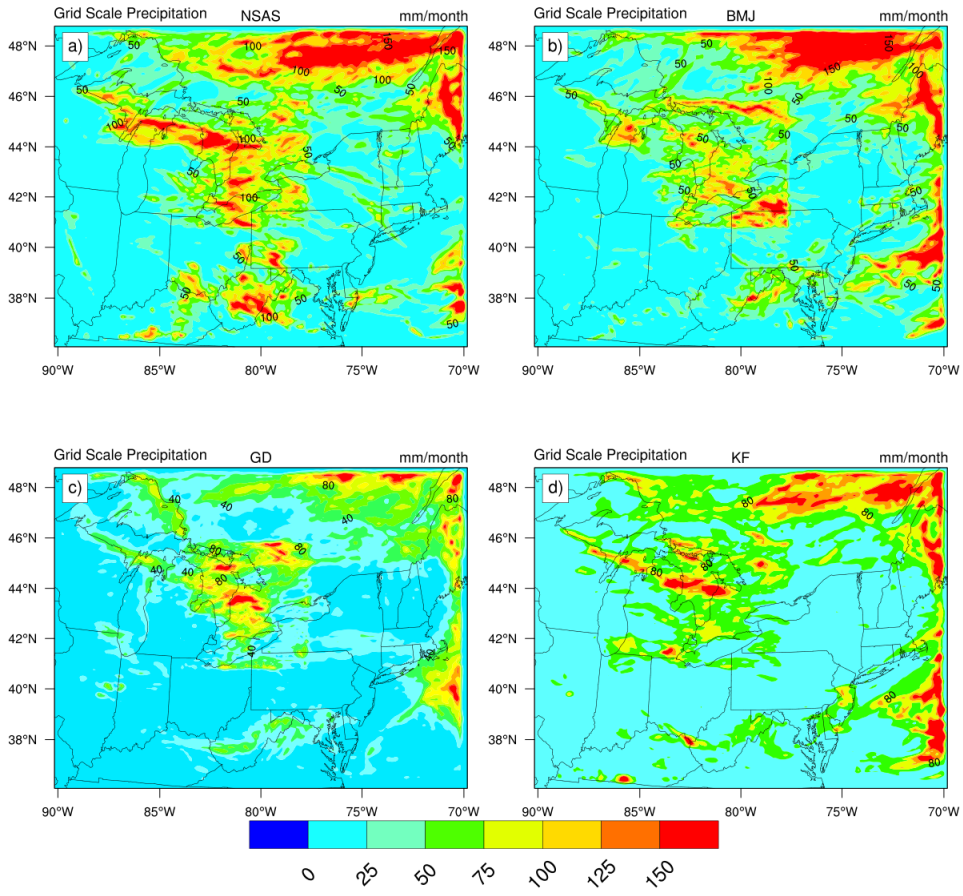

Figure A.0.2: As in Figure A.0.1 but for July

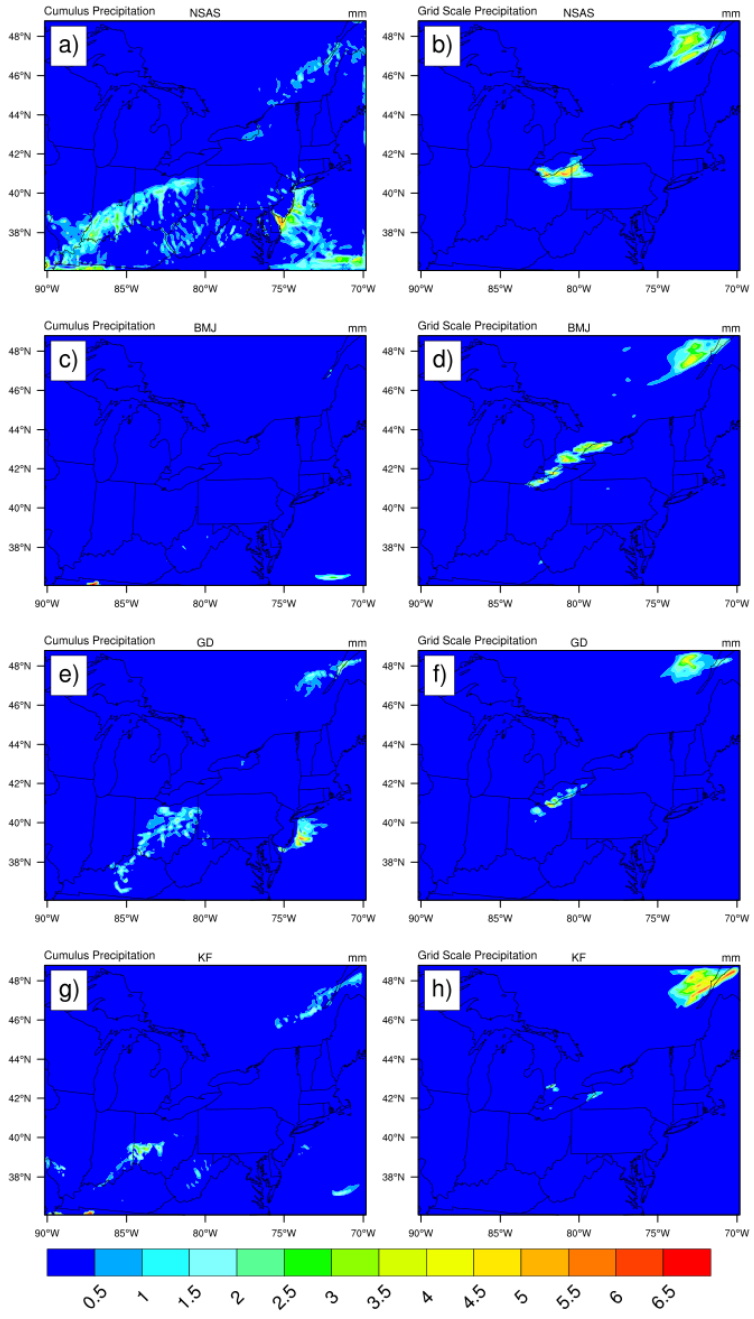

Figure A.0.3: Three hourly (from 0600 UTC to 0900 UTC) accumulated grid and sub-grid scale precipitation on July 23, 2002.

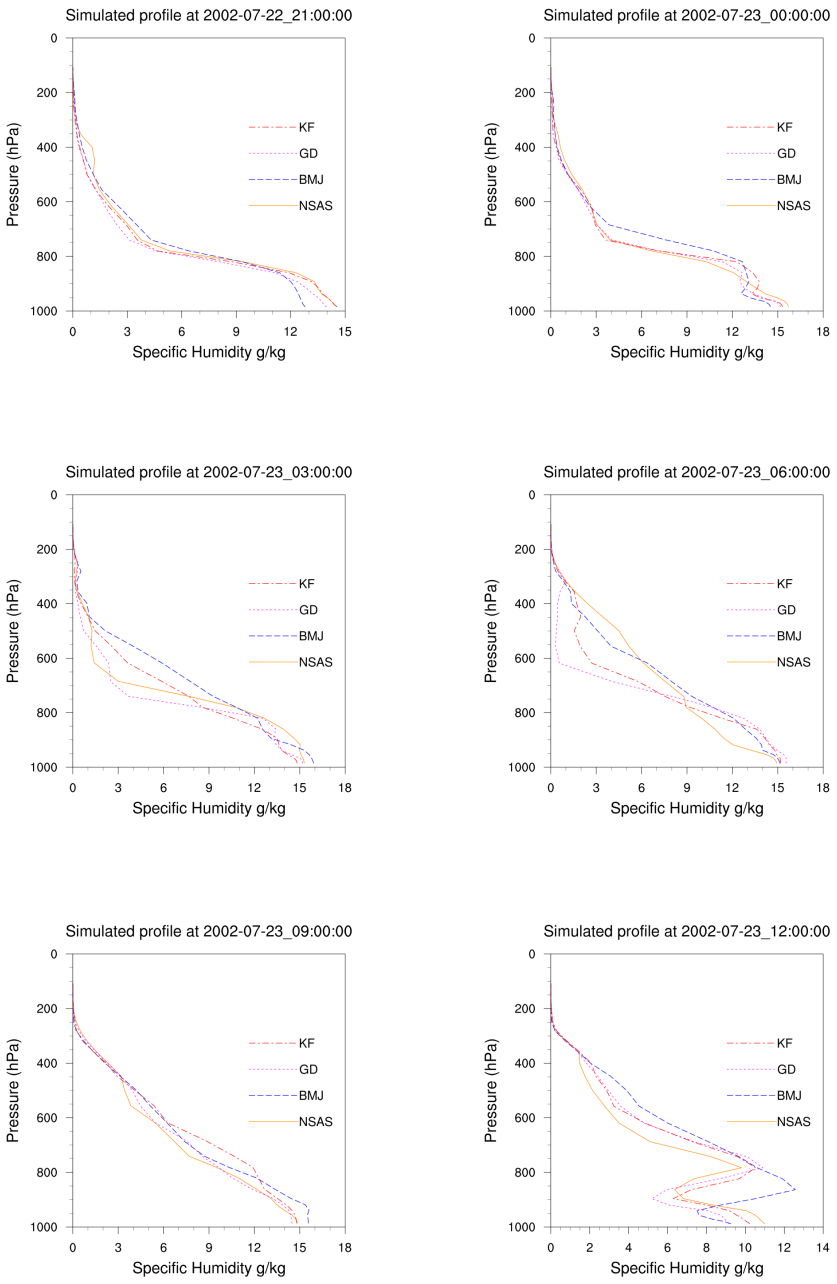

Figure A.0.4: Temporal evolution of simulated specific humidity (SH) profiles: valid from July 22, 2100 UTC to July 23, 1200 UTC of 2002.

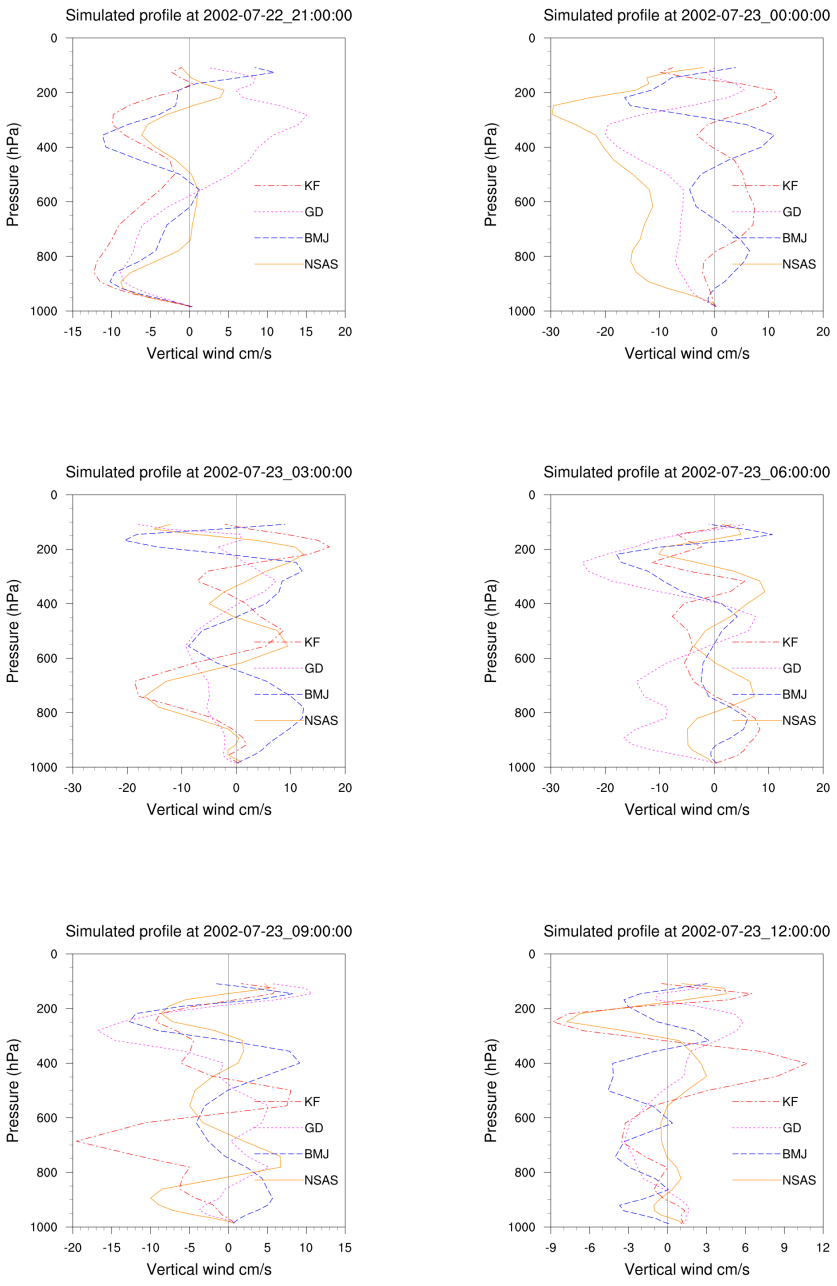

Figure A.0.5: Temporal evolution of simulated vertical wind (W) profiles: valid from July 22, 2100 UTC to July 23, 1200 UTC of 2002.

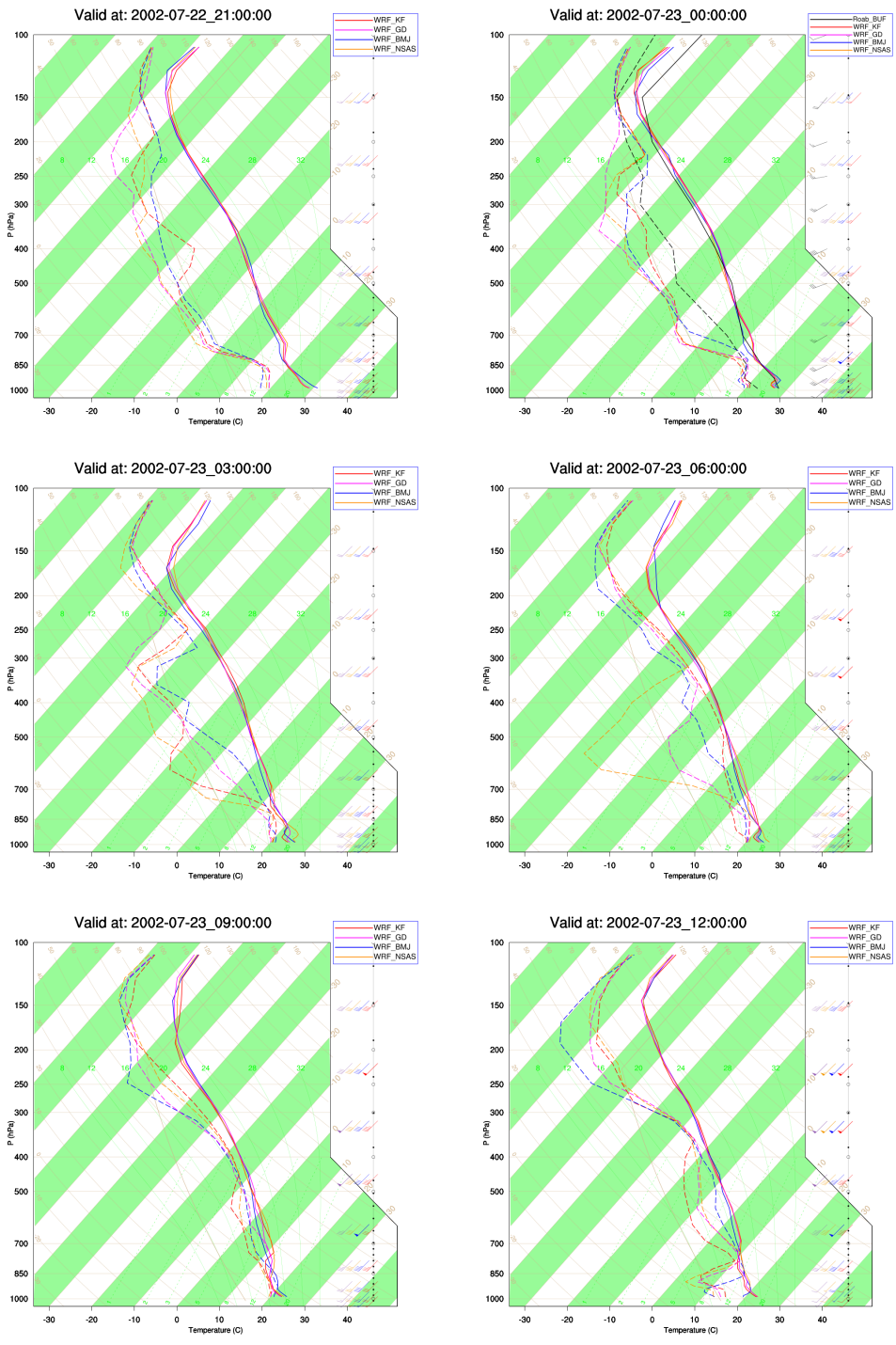

Figure A.0.6: Temporal evolution of Skew-T profiles: valid from July 22, 2100 UTC to July 23, 1200 UTC of 2002.

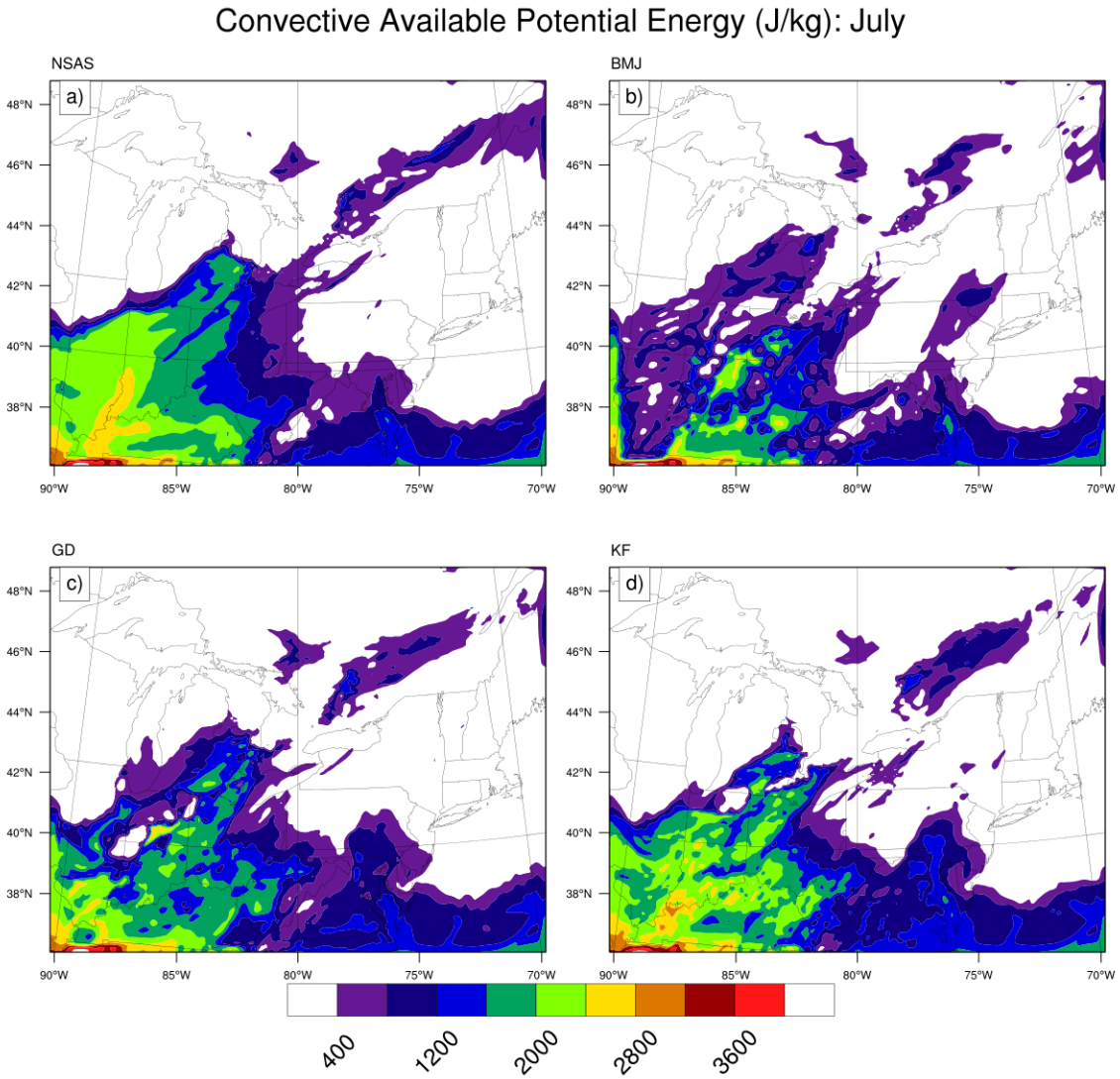

Figure A.0.7: Simulated Convective Available Potential Energy (CAPE) in Jule per Kilogram for a) NSAS, b) BMJ, c) GD, and d) KF, valid at July 23, 2002, 0000 UTC.

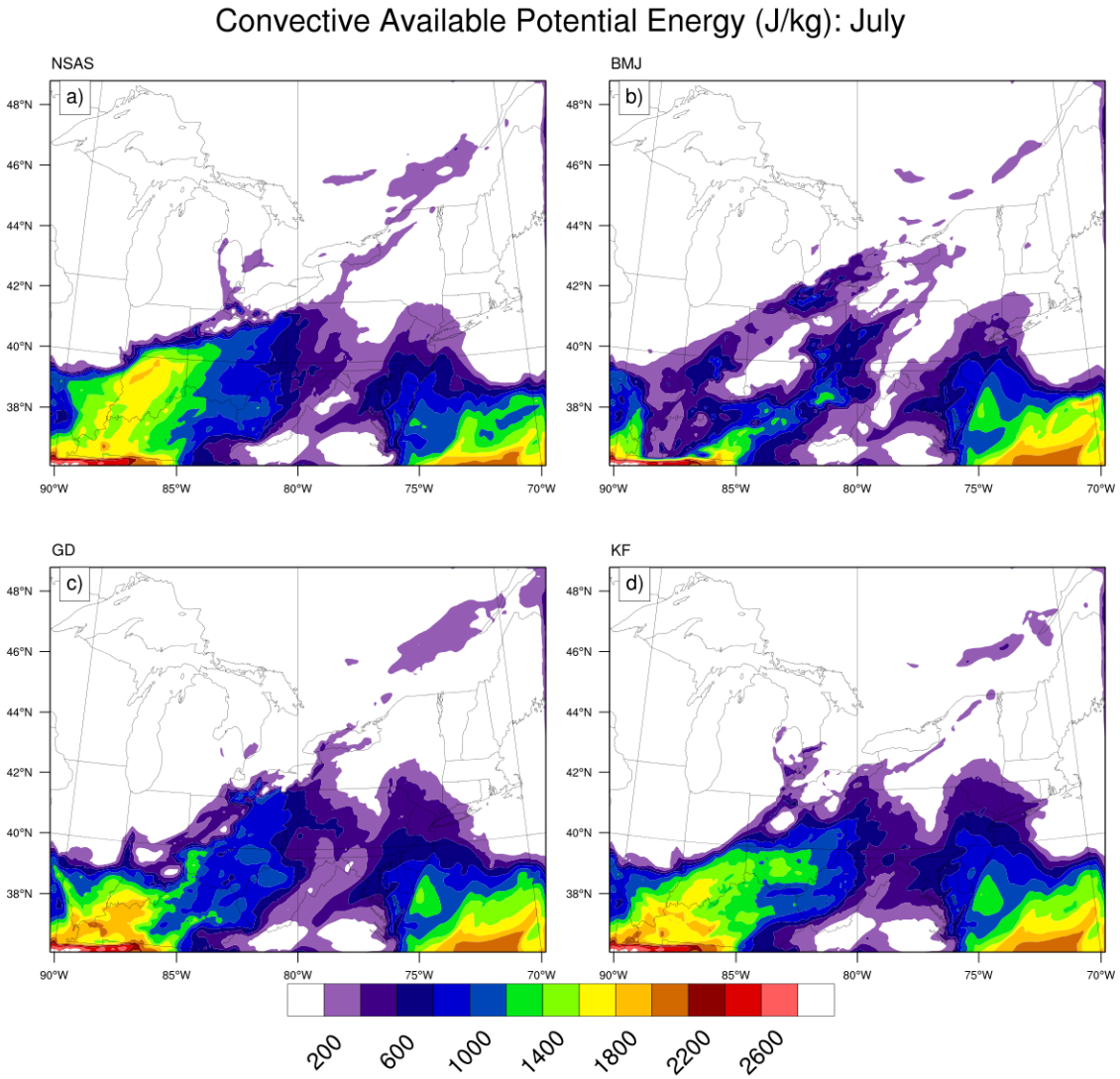

Figure A.0.8: The same as Figure A.0.7 but valid at July 23, 2002, 0600 UTC.

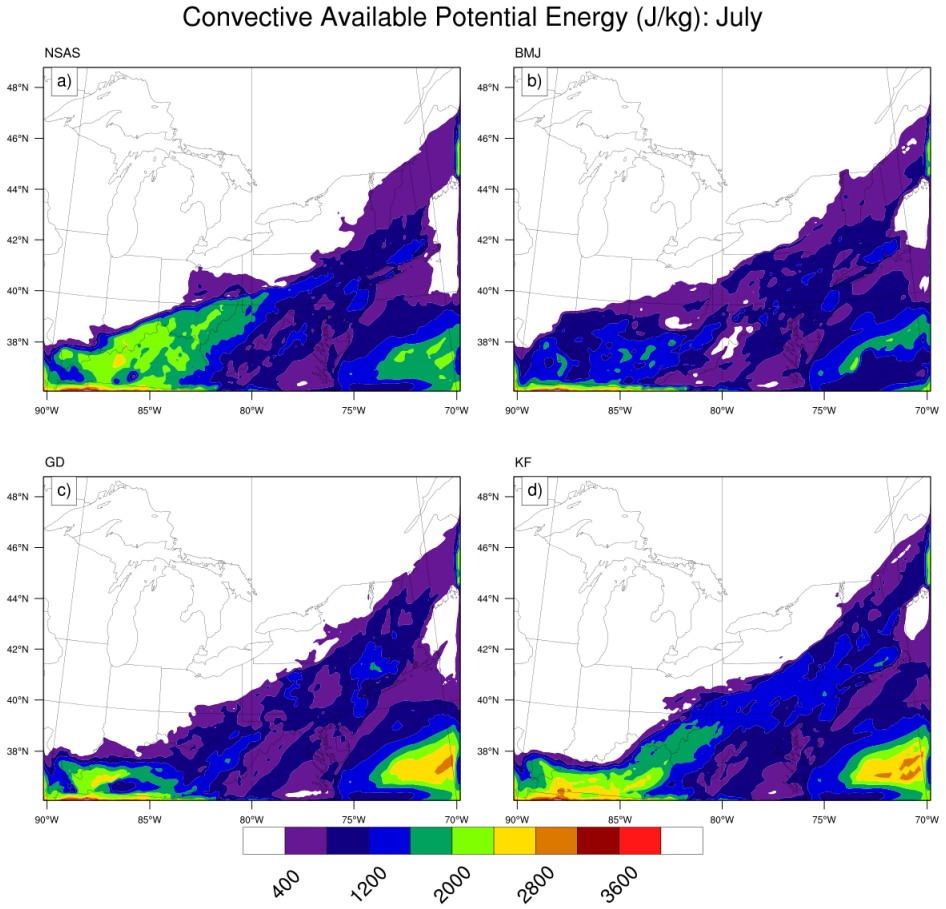

Figure A.0.9: The same as Figure A.0.7 but valid at July 23, 2002, 1500 UTC.

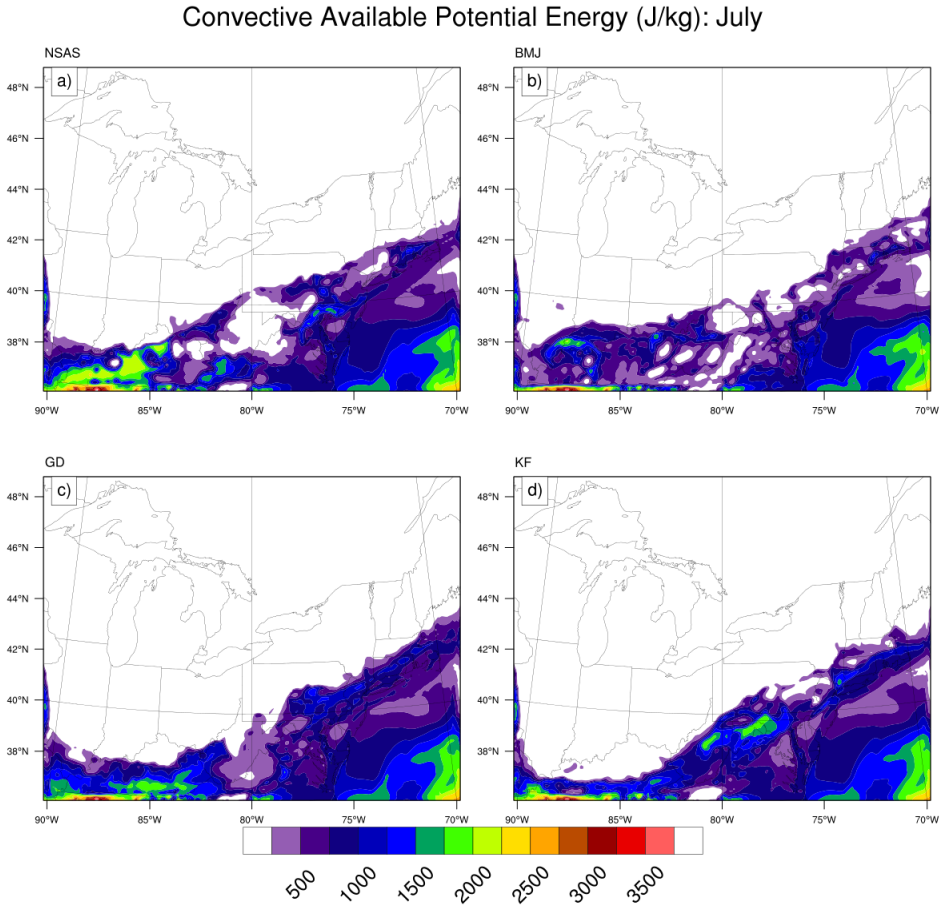

Figure A.0.10: The same as Figure A.0.7 but valid at July 24, 2002, 0000 UTC.

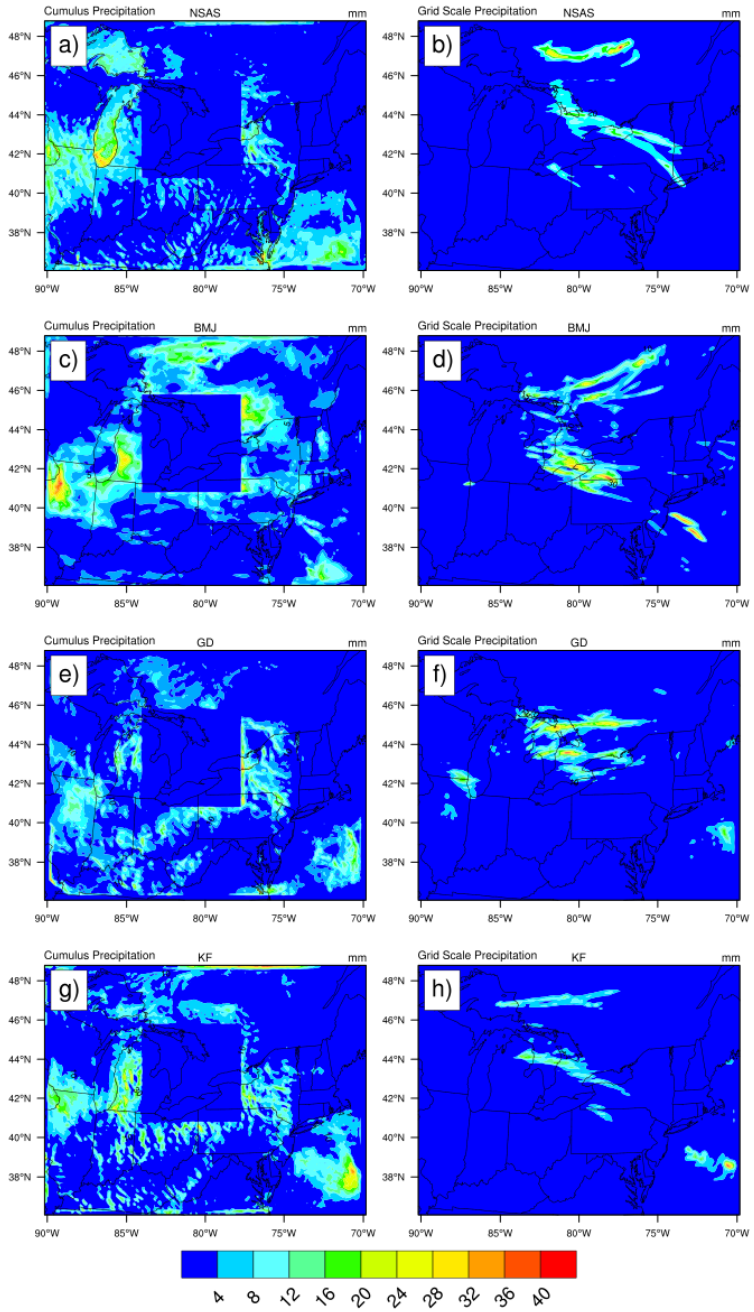

Figure A.0.11: 24 hour accumulated subgrid (left column) and grid (right column) scale precipitation in mm from 0000 UTC of July 28 to 0000 UTC of July 29, 2002.

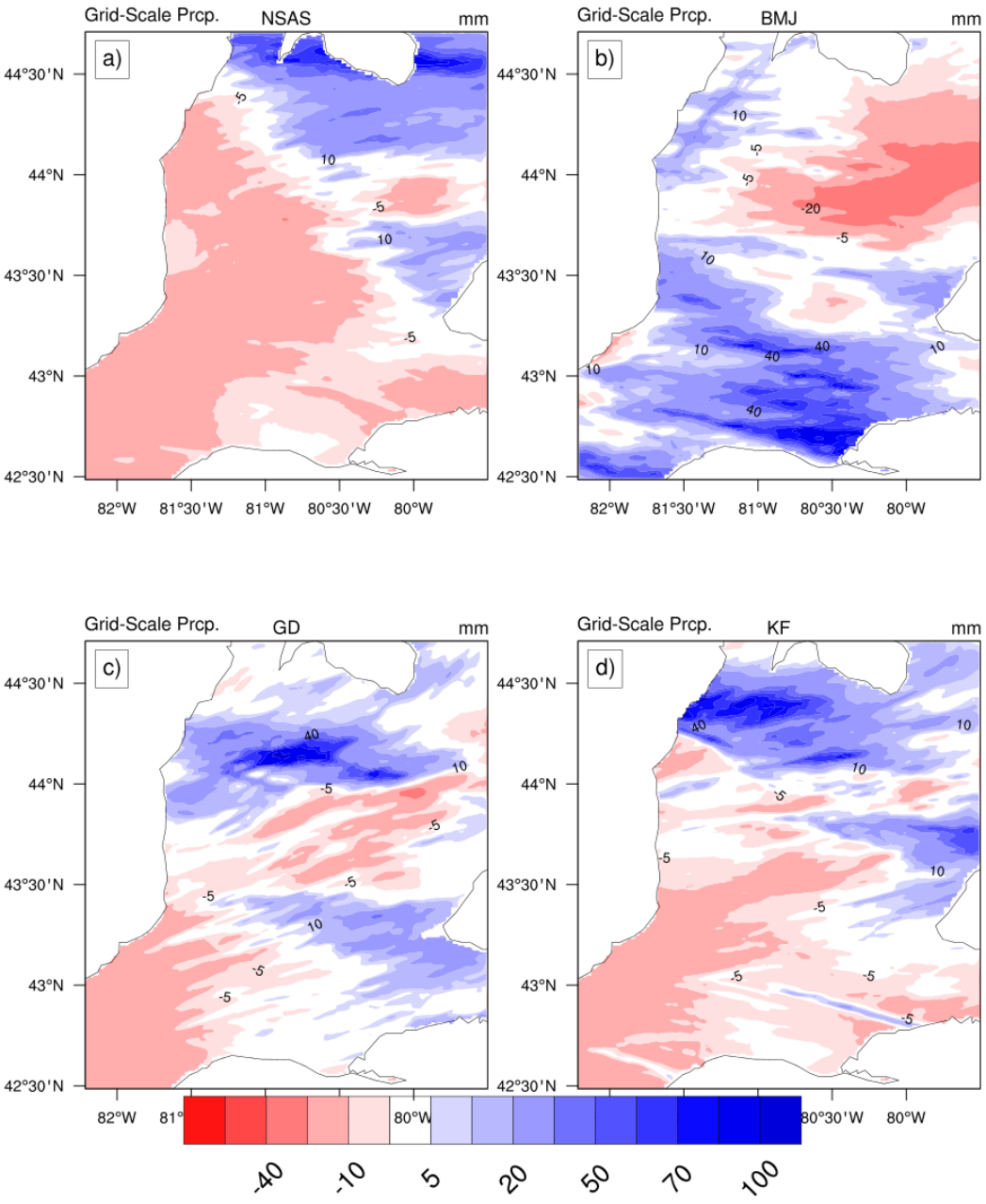

Figure A.0.12: 24 hour accumulated grid scale precipitation bias (WRF-DAYMET) in mm from 0000 UTC of July 28 to 0000 UTC of July 29, 2002 from the innermost domain.

Appendix B

Datasets used in this study

1) The North American Regional Reanalysis (NARR) of [61]

http://rda.ucar.edu/datasets/ds608.0/index.html#sfol-hr?g=3

2) Sea surface temperature (SST) devloped by NCEP's Marine Modeling and Analysis Branch (NCEP / MMAB) [96]

http://polar.ncep.noaa.gov/sst/oper/Welcome.html

3) DAYMET Gridded observations of Dr. Peter E Thornton [98]

http://daymet.ornl.gov/overview

4) The North America land data assimilation system (NLDAS-2) land surface model output of Mitchell *et al.* (2004) [65]

ftp://hydro1.sci.gsfc.nasa.gov/data/s4pa/NLDAS/

5) NCEP Automated Data Processing (ADP) global upper air and surface weather observations

http://rda.ucar.edu/datasets/ds337.0/

6) The Great Lakes Ice-cover Statistics

The Great Lakes surface and bottom water temperature, ice cover charts, and various statistics have been collected from the following agencies:

Observed Ice Charts from Canadian Ice Service

https://www.ec.gc.ca/glaces-ice/default.asp?lang=En&n=D32C361E-1

Canadian Ice Service Archive

http://iceweb1.cis.ec.gc.ca/Archive/

Ice analysis charts from NOAA's Great Lakes Environmental Research Laboratory (GLERL)

http://www.glerl.noaa.gov/data/ice/

National Snow and Ice Data Center

http://nsidc.org/

Various ice analysis product from the United States National Ice Center (NIC)

http://www.natice.noaa.gov/products/great_lakes.html

Realtime MODIS Sea Surface Temperatures (SSTs) from TERRA and AQUA from the University of Wisconsin-Madison

http://cimss.ssec.wisc.edu/db_products/SST/

The Great Lakes Statistics

http://coastwatch.glerl.noaa.gov/statistic/statistic.html

Appendix C

Atmospheric scales

TABLE 1. Atmospheric scale definitions, where L_H is horizontal scale length.

L_H	Lifetime	Stull (1988)	Pielke (1984)	Orlanski (1975)	Present	Atmospheric phenomena
10 000 km	1 month	Macro	Synoptic Regional	Macro-α	Macro-α	General circulation, long waves
2000 km	1 week			Macro-β	Macro-β	Synoptic cyclones
200 km	1 day	Meso	Meso	Meso-α	Macro-γ	Fronts, hurricanes
20 km	1 h			Meso-β	Meso-β	Low-level jets, thunderstorm groups, mountain winds and waves, sea breeze, urban circulations
2 km				Meso-γ	Meso-γ	Thunderstorm, clear-air turbulence
200 m	30 min	Micro	Micro	Micro-α	Meso-δ	Cumulus, tornadoes, katabatic jumps
20 m	1 min			Micro-β	Micro-β	Plumes, wakes, waterspouts, dust devils
2 m	1 s	Micro-δ		Micro-γ	Micro-γ	Turbulence, sound waves
					Micro-δ	

Figure C.0.1: Atmospheric Scales Definitions according to Thunis and Bornstein (1996), [100]